A MIXED EULERIAN-LAGRANGIAN APPROACH FOR THE SIMULATION OF INTERFACIAL PHENOMENA IN SOLIDIFICATION PROCESSING

By

H S UDAYKUMAR

A DISSERTATION PRESENTED TO THE GRADUATE SCHOOL
OF THE UNIVERSITY OF FLORIDA IN PARTIAL FULFILLMENT
OF THE REQUIREMENTS FOR THE DEGREE OF
DOCTOR OF PHILOSOPHY

UNIVERSITY OF FLORIDA

1994

ACKNOWLEDGEMENTS

I have learned much from Professor Wei Shyy during my studies at the University of Florida. It is seldom that one encounters individuals with the intellectual calibre, scientific temper and humanity that are embodied in him. His tolerance of the several quirks of personality and mood swings of his students and his patient guidance will remain in my memory as an example. It is difficult to imagine any research environment that can parallel the one he creates for his group in terms of the freedom of thought and the opportunity to develop one's individual traits. I shall remain deeply grateful to him for his benevolence.

My parents, H. N. S. Murthy and Shailaja Murthy, grandparents J. B. Balvant Rao and Pramila Rao, sister Nita N. Deshpande, and brother-in-law Naren Deshpande have always been a source of support and love, for which I am thankful beyond words. I hope this work in some measure justifies their pride in me. I am also thankful for the affection showered on me by my aunts, uncles and cousins, all of whom, though physically separated from me, literally by many seas, are inextricably woven into the fabric of my being.

In the later stages of my studies I had the fortune of meeting and gaining the affection of a truly remarkable person. I can only attempt to express my heartfelt thanks to Christine Bohannan for all the wonderful things that she has brought into my existence.

Over the past few years, I have been fortunate to develop close friendships with Jeff Wright and Siddharth Thakur and his wife Jyoti. Through good times and bad, we have managed to maintain a cheerful outlook and to share our gro-

tesque frequently juvenile sense of humor The near inseparability of the three of us has occasioned many a remark in the department and will have a deep and lasting impact on our lives I am grateful to that excellent fellow Ramesh Marrey for being a most understanding roommate for over 6 years, during which period he has courageously withstood my culinary experiments Other group members, the enigmatic philosopher at-large Rick Smith, the phlegmatic Madhukar Rao, an asset as far as computer resources go, James Liu with his bisyllabic humour and Rajat Mittal, have all been excellent company over the years

I wish to thank the members of my doctoral committee, Professors L E Malvern, U H Kurzweg, D W Mikolaitis and R. Narayanan for their guidance and support Thanks are also due to the Department of Aerospace Engineering, Mechanics and Engineering Science, University of Florida, for uninterrupted financial support during the entire period of my studies

TABLE OF CONTENTS

	page
ACKNOWLEDGEMENTS	ii
ABSTRACT	ix
CHAPTERS	
1 THE PHYSICS OF MORPHOLOGICAL INSTABILITIES DURING SOLIDIFICATION	1
1.1 Introduction	1
1.1.1 Motivation	1
1.1.2 Need for Numerical Techniques	5
1.2 Theory of Morphological Instabilities in Solidification	7
1.2.1 The Mullins-Sekerka Mechanism	7
1.2.2 The Solid-Liquid Interface	9
1.2.2.1 Kinetics of solidification, the Gibbs-Thomson condition	9
1.2.2.2 Facetted and rough growth	12
1.2.2.3 Macroscopic interfaces	14
1.2.3 The Evolution of Interfacial Morphology	15
1.3 Implications of Morphological Instabilities	27
1.4 Concluding Remarks	32

2 MODELLING AND SCALING OF SOLIDIFICATION PROCESSES 33

2 1 The Demands on the Numerical Method 33

2 2 Numerical Methods Applied to General Moving Boundary Problems 34

2.2 1 Interface definition 34

2.2.2 Interfacial boundary condition 36

2 2 3 Discretization of the domain 36

2 2 4 Topological changes of the interface 36

2 3 Choice of Method -- Lagrangian or Eulerian ? 37

2 4 Review of Available Methods for Moving Boundary Problems 37

2 5 Micro and Macroscopic Modelling of Solidification Phenomena for Pure Materials 45

2 6 A Typical Scaling Analysis 47

2 6.1 Level 1 The Outer Scales 50

2 6.2 Level 1 Flowfield in the Interface Region 52

2 6 2 1 Scales in the intermediate viscous layer 55

2 6.2 2 Scales in the intermediate thermal layer 56

2 6 3 Level II The Morphological Scales 59

2 7 Equations at the Morphological Scales for Pure Conduction 64

2 8 Morphological Scales and Non Dimensionalized Equations with Convection 65

2 8 1 Case 1 65

2 8 2 Case 2 67

2.9 The Non-dimensionalized Equations Applicable to the Problem 67

2 10 Setting Up a Micro-Model 69

2 11 Conclusions 71

3 A BOUNDARY-FITTED APPROACH TO SIMULATION OF INTERFACIAL INSTABILITIES 73

3 1 Introduction 73

3 2 Assessment of the Quasi-stationary Approximation 74

3 2 1 Formulation 74

3 2 2 Results and Discussion 78

3 3 A General Procedure for Interface Tracking 79

3 4 Results and Discussion 81

3 4.1 Case 1 Calculations with Temperature Field Active in One Phase Only 81

3 4.2 Case 2 Calculations with Temperature Field Active in Both Phases 82

3 5 Motion of Curved Fronts 85

3 5 1 Interfacial Conditions 85

3.5.2 Scales for the Morphological Instability Simulations 87

3 5 3 Features of the Computational Method 90

3 5 4 Results and Discussion 91

3 6 Preliminary Investigation of Convection Effects 97

3 7 Conclusions 103

4 AN INTERFACE TRACKING METHOD FOR ARBITRARILY SHAPED INTERFACES AND THEIR INTERACTIONS 106

4.1 Introduction 106

4 2 Interface Tracking Procedure 109

4 2 1 Basic Methodology 109

4 3 Mergers of Interfaces 115

4.3 1 Procedures for Merger 115

4 3 2 Summary of Merger Procedure 127

4 4 Results 127
4 4 1 Results for Non-Merging Interfaces 127
4 4 2 Results for Merging Interfaces 134
4 5 Conclusions 138

5 A METHOD FOR THE SIMULATION OF DIFFUSION CONTROLLED INTERFACIAL INSTABILITIES 142
5 1 Requirements of the Numerical Method 142
5 2 Outline of the Current Approach 143
5 3 Formulation 143
5 4 The Solution Methodology 148
5 4 1 Obtaining the Thermal Field 148
5 4 2 Computing the Velocities of the Interfacial Markers 156
5 5 Results and Discussion 157
5.5 I Grid Addition/Deletion 157
5.5.2 Planar Interface Propagation 158
5 5 3 Experiments with Non-planar Interfaces 159
5 5 3 1 Zero surface tension 161
5 5.3 2 Low surface tension 164
5 5 3 3 Imposition of symmetry 168
5 5 3 4 Stable fingers for significant surface tensions 170
5 6 Conclusions 179

6 A COMPUTATIONAL TECHNIQUE FOR FLUID FLOWS WITH MOVING BOUNDARIES 181
6 1 Introduction 181
6 2 The Control Volume Formulation for a Transport Variable ϕ 188

6.2.1 Discretization 188
6.2.2 The Staggered Grid 190
6.2.3 Computation of the Pressure Field 192
6.2.4 Computation of Convective and Diffusive Fluxes and Source Terms 192
6.2.5 Computation of Interfacial Fluxes 195
6.2.6 Evaluation of the Source Term 198
6.2.7 The Continuity Equation - Pressure Correction Equation 199
6.2.8 Dealing with Cut Cells 200
6.2.9 Conservation and Consistency at Cell Faces 201
6.2.10 Anomalous Cases 202
6.2.11 Distinction between Liquid and Solid Cells 203
6.2.12 Moving Boundary Problems – Treatment of Cells that Change Phase 203
6.3 Results and Discussion 205
6.4 Summary 212

7 SUMMARY AND SUGGESTIONS FOR FUTURE WORK 217

REFERENCES 223

BIOGRAPHICAL SKETCH 233

Abstract of Dissertation Presented to the Graduate School
of the University of Florida in Partial Fulfillment of the
Requirements for the Degree of Doctor of Philosophy

A MIXED EULERIAN-LAGRANGIAN APPROACH FOR THE SIMULATION OF INTERFACIAL PHENOMENA IN SOLIDIFICATION PROCESSING

By

H S Udaykumar
December 1994

Chairperson Wei Shyy
Major Department Aerospace Engineering, Mechanics and Engineering Science

Instabilities of the solid liquid interface determine grain structures and compositional and structural inhomogeneities of alloys, and are typical of a wider class of pattern forming processes in natural as well as engineered environments The present effort is directed toward developing a comprehensive computational method for the investigation of such interfacial instabilities One key aspect of the instabilities in solidification is the existence of multiple scales The length scales corresponding to capillarity, instability wavelength and the growth environment are widely separated. A scaling procedure is presented to characterize the effects of the macroscopic transport phenomena on the microscales

A computational technique using the conventional body fitted adaptive grid formulation is first developed but serious difficulties arise in the advanced stages of the instability due to the convoluted moving phase boundary Thus, a fresh approach is deemed necessary to handle the following features

1) complex interfaces and their interactions, 2) the phenomena at the interface, without resorting to averaging procedures, and 3) computation of flow variables in each phase subject to moving, irregularly-shaped boundaries

The first capability is developed in an interface tracking scheme that incorporates a fixed Cartesian grid and a Lagrangian interface representation. The tracking scheme is developed separately from the field solver A method to track the mergers and fragmentation of interfaces is devised, taking advantage of the mixed Eulerian-Lagrangian features Next, with pure conduction heat transport in the two phases, we develop the control volume formulation for irregularly shaped cells and techniques for dealing with the cut cells that arise when an interface of arbitrary shape passes through an underlying Cartesian grid The simulations result in finger-like forms and clearly demonstrate the effects of capillarity

Finally, the Navier-Stokes equations are solved Details regarding the computation of convective fluxes and interfacial boundary conditions are resolved A pressure-based implicit in time algorithm is used to solve the field equations The method is tested first for stationary deformed geometries and then for moving boundaries including phase change. The results obtained compare favorably with those from previously benchmarked solvers using curvilinear coordinates

The framework developed here can handle the presence of deformed and moving boundaries Application of the algorithm is envisaged for computation of flows in complex geometries, including internal phase boundaries that can undergo severe distortions.

CHAPTER 1

THE PHYSICS OF MORPHOLOGICAL INSTABILITIES DURING SOLIDIFICATION

1.1. Introduction

1.1.1. Motivation

Physical systems are often comprised of coexisting regions with distinct physical and chemical properties. For example, it is not uncommon to find natural or engineered environments containing a variety of compositions, phases, material properties and flow features. When such distinct regions are present, they are obviously accompanied by interfaces. Depending on the physical properties of the various components of the system or the conditions imposed thereupon, the interfaces may represent discontinuities i.e., they may be of infinitesimal thickness. Under certain conditions, usually characterized by one or more control parameters, the interfaces experience instabilities. Typically, a cascade of interfacial instabilities on an initially smooth interface results in intricate, often densely branched structures. The observed mature patterns and morphological structures reflect the interaction of the micro- and macroscopic properties of the system. In this dissertation we shall be concerned mainly with the instabilities occurring on the phase boundary separating solid and liquid phases (Brenner et al., 1991, Kessler et al., 1988, Langer, 1981, Pelce, 1988, Sekerka, 1993, Woodruff, 1973). This system has attracted the attention of researchers from a wide variety of fields due to its aesthetic as well as technological appeal.

Morphological instabilities at the solid-liquid or solid-vapor phase boundary determine the shapes and properties of grown crystals. An inspiring and per

hops the most familiar example of the consequences of such instabilities is the snowflake, which assumes a highly branched, six-fold symmetric shape under certain growth conditions (Nakaya, 1954) As early as the seventeenth century Kepler (Emerton, 1984) observed that

> The cause of the six-sided shape of a snowflake is none other than that of the ordered shapes of plants and of numerical constants. . . I do not believe that even in a snowflake this ordered pattern exists at random . . . There is then a formative faculty in the body of the earth . . . the faculty of earth is in itself one and the same, but it imparts itself to different bodies and cooperates with them It engrafts itself on them and builds now one design, now another, as the inner disposition of each matter or outer conditions allow (p. 41, Emerton, 1984)

Although Kepler's insights into the mechanisms of formation of the snowflake were constrained by the inadequate knowledge in his time of the states and fundamental structure of matter, he correctly anticipated some of the key features of pattern forming processes. In particular his intuition regarding the interplay of microscopic (*inner disposition*) and macroscopic (*outer conditions*) features has been borne out by research in the past few decades (Kessler et al., 1988)

For some time now, quite successful efforts have been directed at unravelling the physics underlying such repeatable patterns as the snowflake. The motivation is to unearth a paradigm for organized phenomena far from equilibrium. On the most fundamental level, one is interested in revealing the causes and effects of the plethora of patterns observed in nature. Biological systems for example, abound in forms driven by function. In a recent review of the current state of knowledge in the area of pattern formation, Cross and Hohenberg (1993) write, in connection with biological patterns

> . . . at the earliest stages of development there arises the question of how spatial differentiation arises in a featureless medium. A mathematical form of this question concerns the breaking of a symmetry : one end of a symmetric egg will become the head and the other the tail. As with any broken symmetry, chance i.e. fluctuations, can determine which is which, but this choice is only binary -- the head will not appear in the middle of the embryo. As the organism grows different parts will develop quite different functions, despite the fact that the material of the embryo is rather homo-

> geneous at least at the level of the molecular chemistry controlling development. It is true that on its full scale, the embryo is not spatially uniform due to its finite size, and ultimately this limitation will play a vital role. The question remains of how this macroscopic nonuniformity is communicated to the smaller scales. (p. 1050)

It is obvious that the issues pertaining to formation of structures in biological systems are considerably more complex than in other physical systems. The fundamental physical processes and principles underlying biological patterns are not well understood. The causes may be biochemical in origin and may involve environmental effects. In contrast, the solidification process represents one of the simpler systems displaying pattern formation, and has been widely researched for that reason. Nevertheless, even in this system several unanswered questions remain. It is the objective of this work to establish a framework directed toward answering some of these questions.

The interest in pattern-forming phenomena during solidification does not stem solely from aesthetic or theoretical standpoints. Strong technological motivations exist for the study of such patterns (Brown, 1988, Flemings, 1974). For example, the demands on purity and crystal quality of semiconductors and high-temperature alloys are becoming ever more stringent. Under commonly encountered solidification environments employed in the preparation of such materials, instabilities can occur causing the solid–liquid interface to break up into cells and dendrites as shown in Fig. 1.1. When such morphologies result, the solutes or dopants are trapped in the interdendritic or intercellular regions (*microsegregation*) leading to compositional inhomogeneities. The non-uniformities can be discerned from the characteristic patterns observed in metallographic sections. They determine the grain sizes, defects and other crystal properties. To mitigate the impact of instabilities materials are often processed at rates, solute concentrations and temperature levels at which they can be avoided or reduced. In producing alloys, for example, instabilities at the interface can be avoided at low

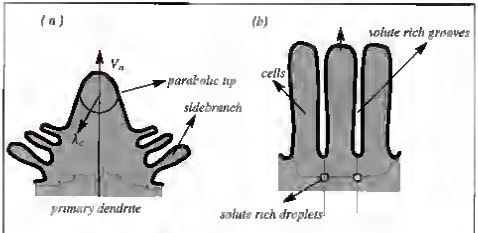

Fig. 1.1 Illustration of two types of interfacial morphologies upon instability at the solid–liquid interface (a) Dendritic and (b) Cellular morphologies arising during solidification.

growth rates, while maintaining large temperature gradients in the melt Thus the process variables and economics of solidification processes are influenced by considerations involved in dealing with morphological instability While maintaining low growth rates may conflict with the economics of production, large temperatures may lead to thermal stresses that may impact on the structural properties of the crystals produced. Therefore, much attention has recently been directed by the materials science community to fully understand the instability phenomena and develop the capability to predict and control them The complexity of the physics involved in these highly nonequilibrium, nonlinear phenomena is further compounded by the mieroscopic scale of the events, the high temperatures at which metallic systems operate and by the opacity of metallic melts These problems hinder experimental as well as analytical investigations Furthermore, as will become clear in subsequent chapters a plethora of physical issues enter into the overall solidification process, each with characteristic length and time scales and physical mechanisms predominant at these scales Thus, in order to understand fully the solidification process and the pattern-forming phenomena in-

volved therein numerical simulation is perhaps the most viable investigative technique

1.1.2 Need for Numerical Techniques

To date, several instability phenomena involving interfaces have been studied by researchers from a wide range of specializations While the snowflake is an example of a solid vapor system that has experienced a *morphological instability* , the growth of ice crystals (Tirmizi and Gill, 1987), i.e , in a solid-liquid system, also gives rise to complex morphologies. Other well investigated examples of interfacial instabilities include the Saffman-Taylor fingering phenomenon (Saffman and Taylor, 1958 Bensimon, 1986) between two fluids of different viscosities Such fingers have been studied in connection with *water coning* in oil recovery (Glimm et al , 1988), flow through porous media (Homsy, 1987), and in two−dimensional form in Hele-Shaw cells in the laboratory (Tabeling et al , 1987) The Saffman Taylor instability is in fact an analogue of the solidification morphology problem and several of the conclusions drawn from analyses of the former phenomenon have been found to apply to the latter (Kessler et al , 1988). Fluid-fluid systems such as liquid crystals and organic materials and the process of electro-deposition are also subject to interfacial instability in a similar fashion to the solid-liquid systems (Flesselles et al , 1991) Other interesting examples of interfacial instabilities in hydrodynamics include the Kelvin Helmholtz instability in its various forms (Huerre,1987), the Rayleigh Taylor overturning instability (Sharp, 1984) and the breakup of liquid jets (Drazin and Reid 1981)

Conventionally, the onset and linear growth stages of disturbances in the above mentioned phenomena have been investigated along the same lines as Lord Rayleigh's approach to the jet instability problem (Rayleigh, 1899), applying linear stability theory Weakly nonlinear analyses in extension of the onset behavior have also been performed (Langer 1980) However, far from onset, the interfaces

undergo successive instabilities of various types and in some systems the final observed pattern may deviate significantly from that predicted by linear stability analyses. In other cases the instability may be triggered by large amplitude disturbances and such subcritical phenomena are obviously not accessible to linear stability considerations. The mechanisms by which the nonlinear phenomena induce reorganizations and coherent patterns in unstable systems are not therefore clarified by analyses restricted to small perturbations. Thus, sufficient motivation exists for developing general investigative capabilities in order to study the above mentioned phenomena in their highly nonlinear stages. This regime is obviously most accessible to laboratory and computational experiments.

The effort presented herein is devoted to developing a tool for computational study of the instability of interfaces far into the nonlinear growth stages. We choose to investigate the phenomenon of morphological instabilities during solidification due to its significance both as a typical pattern forming system and in materials processing technologies. In addition the instabilities in this system result in interfacial patterns, i.e., crystal morphologies which pose a challenge to any simulation procedure. The interaction of the solidification front with itself, or with other fronts, and with the growth environments are typical of pattern–forming phenomena. Numerical simulation of the various events leading to complete solidification is a complex task. In order to understand the demands on the numerical techniques to be developed in later chapters, it is first necessary to familiarize oneself with the physics. This is the objective of the following sections.

1.2. Theory of Morphological Instabilities in Solidification

1.2.1. The Mullins-Sekerka Mechanism

Two simple configurations in which to obtain solidification are shown in Fig. 1.2. As shown in Fig. 1.2(a), let the walls of the chamber containing a single component (i.e. pure) liquid be held at a temperature below the fusion temperature, T_m. The melt in such a state is said to be *undercooled*. If one were to place a spherical seed crystal at the center of this chamber, solidification will proceed outward, accompanied by the release of the heat of fusion at the crystallizing front. The need for undercooling and the seed crystal will be clarified later. The distinguishing feature of the set-up in Fig. 1.2(a) would be that the spherical seed crystal would not result in a spherical solidification morphology, i.e. the front will not maintain a smooth spherical shape during growth. The situation in this case is unstable. In contrast, in the set-up in Fig. 1.2(b) the growth front will remain smooth, deviating from a sphere due to the influence of geometry of the growth chamber on heat transfer rates. The growth in this case is stable. The explanation of this instability phenomenon was first provided by Mullins and Sekerka (1964) in the context of multi-component materials. In the case of pure materials the instability can be explained with the aid of Fig. 1.2(c). Here the liquid boundary is maintained at a temperature slightly below the fusion temperature, i.e. $T_l = T_m - \Delta$. Let a perturbation arise on the initially flat solidification front. For the present let the solid-liquid interface represent the isotherm corresponding to $T = T_m$. As shown in the figure, when the bump forms, the isotherms in the liquid phase ahead of the bump are compressed. In other words, the bump finds itself in a cooler region. This causes accelerated solidification or growth of the bump. One would expect therefore that the bump would find itself in progressively cooler regions causing the instability to run away. While the imposed heat transfer condition at the macroscopic dimensions of the growth chamber induces the instability, the

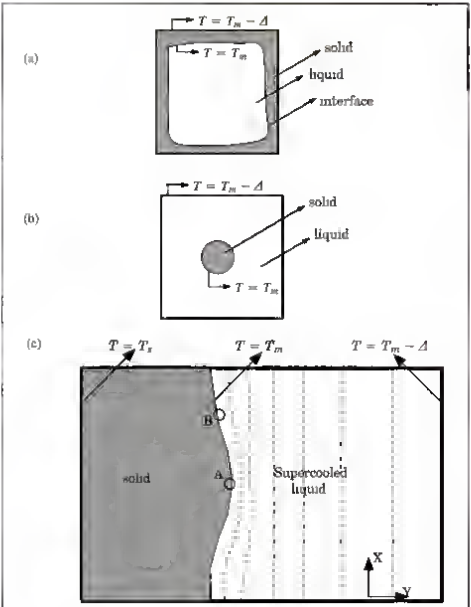

Fig. 1.2 Illustration of solidification arrangements (a) Stable case (b) Unstable case (c) Illustration of the Mullins–Sekerka instability mechanism Dotted lines represent isotherms

morphological features develop at the scale of microns In fact recent work has shown that capillary forces play a key role in pattern selection. A typical capillary length is of the order of angstroms reflecting the origin of capillary forces due to the difference in atomic arrangements across the interface While this basic mechanism of instability is simple enough to be predicted by linear stability analysis, the events subsequent to it are considerably more intricate and analytically intractable In order to understand the nonlinear behavior, it is necessary to familiarize oneself with the interfacial phenomena at each level of concern When the actual pattern-forming process is described in section 1 2 3, it will become clear that the interaction of mechanisms at the different scales is crucial to the emergence of patterns.

1.2.2 The Solid-Liquid Interface

1.2.2.1 Kinetics of solidification, the Gibbs-Thomson condition

The kinetics of solidification (Weeks and Gilmer,1979, Woodruff, 1973), i e , the actual atomic/molecular rearrangement that accompanies a change of phase from liquid to solid plays an important role in the solidification process and its instabilities In order for phase change to ensue, the disordered molecular arrangements from the liquid must assume the lattice structure of the solid phase In the (equilibrium) thermodynamic view, the driving force for this process is the minimization of free energy Considering the system in Fig 1 3, where two phases of volumes V_1 and V_2 and Gibbs free energies G_1 and G_2 are in contact at the surface Ω_{12} of area A, the total Gibbs free energy is given by

$$G = G_1 V_1 + G_2 V_2 + \gamma A \qquad (1\ 1)$$

Here γ is the surface energy or tension. The system will thus evolve in such a direction as to minimize the above total free energy

The first step in the phase transition is the formation of suitable nucleates or substrates in the melt (*homogeneous nucleation*) by the stable agglomeration

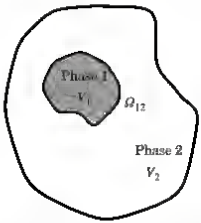

Fig 1 3 Two phases in coexistence Equilibrium is obtained when the total free energy as given in Eq (1 1) is minimized

and reorientation of the clusters of molecules in the liquid state to assume the lattice structure of the solid state. For a planar interface, solid-liquid phase transition occurs when one phase has a lower free energy than the other, at temperatures around the melting point A schematic of the variation of Gibbs free energies with temperature is shown in Fig 1 4

At the melting point, the slopes of the $G-T$ curve are related by

$$(\frac{\partial G_s}{\partial T})_P - (\frac{\partial G_l}{\partial T})_P = \frac{L}{T_m} \tag{1 2}$$

Subscripts s and l indicate solid and liquid phases and P implies that the pressure is held constant. Thus the change in slope of the G-T curve gives the entropy of fusion at the melting point. For a planar phase front , below the melting point, the solid phase has a lower free energy while above it the liquid phase is energetically preferred However, at nucleation the cluster of molecules formed is small enough that the free energy of the interface comes into play. In other words at the small dimensions in question the interatomic bond energies of the neighbors on the surface assume as much importance as those of the neighbors in the bulk. One has

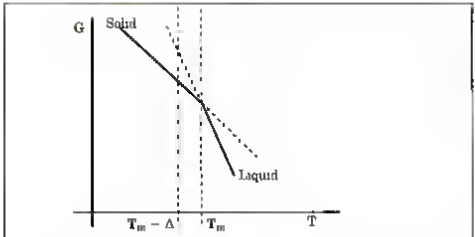

Fig 1 4 Illustration of variation of Gibbs free energy with temperature

to take into account the interfacial energy changes associated with the change in surface area of the nucleus with accretion of atoms from the liquid The minimization of free energy is thus influenced heavily by the surface term in Eq (1 1) In order for solidification to proceed an impetus must be provided to the process by, say, decreasing the temperature below T_m by an amount Δ, called the *undercooling* This operating point is shown in Fig 1 4 To estimate the undercooling necessary, consider a small spherical nucleus. The Gibbs free energy of such a particle in contact with the melt is

$$G = G_s V_s + G_l V_l + \gamma_{sl} A_{sl} \tag{1 3}$$

where γ_{sl} is now the energy of the solid liquid interface of area A_{sl} The total excess free energy of a spherical nucleus of radius r is

$$\delta G = -\frac{4}{3}\pi r^3 \frac{L\Delta}{T_m} + 4\pi r^2 \gamma_{sl} \tag{1 4}$$

where the first term is the contribution due to the change of phase, L being the latent heat of fusion, while the second is that due to the creation of the surface of area $4\pi r^2$ The critical nucleation radius is reached when

$$\frac{\partial \delta G}{\partial r} = 0 \tag{1 5}$$

Thus the critical nucleation radius is

$$r = \frac{2\gamma_{sl}T_m}{L\Delta} \tag{1.6}$$

This relation may also be recast as

$$\Delta = \frac{2\gamma_{sl}T_m}{Lr} \tag{1.7}$$

Thus, for a crystal of radius r, this is the minimum undercooling necessary to induce further solidification. For some metals, the value of the undercooling required can be quite substantial, up to a few hundred degrees. However, in reality such large undercoolings are seldom encountered since *heterogeneous nucleation*, i.e. nucleation on foreign substrates, is possible at much lower undercoolings. Generalizing the content of Eq. (1.7), the interfacial temperature is obtained as

$$T_{i_{eq}} = T_m(1 - \frac{\gamma\kappa}{L}) \tag{1.8}$$

where κ is the curvature of the front and the subscript eq implies that the interface is in thermodynamic equilibrium, i.e. the attachment kinetics are rapid. Eq. (1.8) is the frequently encountered form of the Gibbs-Thomson condition, which can be obtained from thermodynamic considerations (Shyy, 1994). According to Eq. (1.8) regions of positive curvature have lower interfacial temperatures, i.e. melting points, than those with negative curvatures. As explained later this interfacial property has important consequences for pattern selection. The ratio

$$\frac{\gamma}{L} = d_o \tag{1.9}$$

in Eq. (1.8) is the capillary length and is of the order of angstroms. The validity of the assumption of equilibrium at the interface, made in Eq. (1.8), depends on the type of growth considered. The two types of interfacial growth based on attachment kinetics are outlined below.

1.2.2.2 Facetted and rough growth

Atomistically speaking, the interface advance can proceed in smooth (facetted) or rough modes depending on the growth conditions and material considered. In the first type the propagation of ledges or steps provides 2-dimensional nucleation sites for the adatoms from the liquid phase. The growth proceeds with

the propagation of a few monolayers on the interface and is therefore slow and kinetically controlled However, rapid growth is possible in the presence of defects which lead to screw and edge dislocations which provide a continuous source of nucleation sites (Woodruff, 1973, Flemings, 1974) Such smooth or facetted growth occurs at low temperatures when the driving force for solidification is not large Above a certain temperature called the surface roughening transition temperature T_R rough growth occurs. In the case of most metals and many organic compounds, $T_R < T_m$. Thus rough growth is observed in these cases. The atomistic view of the rough interface assumes the form of many layers of random clusters of surface atoms providing a multitude of attachment sites for arriving adatoms Thus, growth is rapid Since in rough growth, random orientations and clustering of adatoms are possible, the final solid profile follows the heat flow characteristics and the interface obtained is isotropic and smooth on a macroscopic scale In contrast, In facetted growth, singularities arise due to the preferred growth directions offered by the low-index planes

For small undercoolings, the kinetics of rough growth, with which we are primarily concerned, can be approximated by the linear rate law

$$V_n = \chi(T_{leq} - T_i) \tag{1.10}$$

where V_n is the interfacial normal velocity and T_i is the temperature at the interface including non-equilibrium effects Often it is necessary to ascribe an orientation dependence so that

$$V_n = \chi(\phi)(T_{leq} - T_i) \tag{1.11}$$

where ϕ is the angle made by the normal with the horizontal and reflects the anisotropy of the underlying crystal lattice Another consequence of such anisotropy is that the surface energy depends on the orientation so that Eq (1.8) becomes

$$T_{leq} = T_m(1 - \frac{\gamma(\phi)\varkappa}{L}) \tag{1.12}$$

In fact, the inclusion of the Herring(1951) torque terms to distinguish between surface tension and surface energy leads to the form

$$T_{f_{eq}} = T_m(1 - (\gamma(\phi) + \frac{\partial^2\gamma(\phi)}{\partial\phi^2})\frac{2\zeta}{L}) \tag{1.13}$$

It is to be noted that although the effects detailed in this section originate due to atomic/molecular structures of liquids and solids they manifest themselves on the macroscopic level. As will be shown below Eq. (1.13) has a significant bearing on the instability phenomena at the chosen micron range wavelengths and beyond.

1.2.2.3. Macroscopic interfaces

The interfacial conditions in the previous section result from the application of equilibrium thermodynamics to describe the physics at the atomic scale. In addition to the conditions that apply on the interface, two additional relations hold across the discontinuity (Carey, 1992). Considering the infinitesimally thin interface in Fig. 1.5(a) and a control volume as shown in Fig. 1.5(b), the statement of mass conservation is obtained for coordinates fixed at the interface as

$$\varrho_g(-V_n)dA = \varrho_f(u_{f_n} - V_n)dA \tag{1.14}$$

where V_n is the normal front velocity, u_{f_n} is the normal component of the fluid velocity with respect to a stationary observer and ϱ is the density. Simplifying, one obtains

$$u_{f_n} = \frac{V_n(\varrho_f - \varrho_g)}{\varrho_f} \tag{1.15}$$

which gives a boundary condition for fluid flow. Similarly, the conservation of energy with the aid of Fig. 1.5(c) is obtained from

$$(q_g - q_f)dA = \varrho_f(u_{f_n} - V_n)h_f dA - \varrho_g(-V_n)h_g dA \tag{1.16}$$

where q is the heat flux through the control volume sides and h represents enthalpy. Applying Eq. (1.15), Fourier's law for the heat flux and noting that the difference in enthalpies at the interface $h_f - h_g = L$, the latent heat of fusion, Eq. (1.16) simplifies to

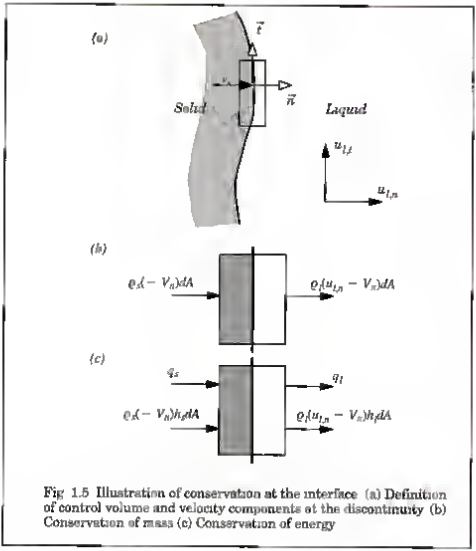

Fig 1.5 Illustration of conservation at the interface (a) Definition of control volume and velocity components at the discontinuity (b) Conservation of mass (c) Conservation of energy

$$\varrho_s V_n L = k_s(\frac{\partial T}{\partial n})_s - k_l(\frac{\partial T}{\partial n})_l \tag{1.17}$$

This expression is called the Stefan condition

1.2.3. The Evolution of Interfacial Morphology

We are now prepared to follow the evolution of the interface subject to the Mullins-Sekerka instability After transients have disappeared, it is observed that

the perturbation on the interface grows to assume a shape with characteristic properties. In the dendritic growth of crystals, for instance, one finally observes a highly branched structure with a nearly paraboloidal tip The radius and velocity of the tip are uniquely determined by the imposed undercooling – which is the only control parameter in free dendritic growth in pure melts – and by the material properties Much work has been directed at understanding this selection mechanism and a plausible theory has evolved over the years(Kessler et al., 1988) The more widely accepted hypotheses regarding selection are outlined below

The analysis of the instability phenomena has been mainly restricted to the pure diffusion transport of heat Thus, the governing equations are

$$\frac{\partial T}{\partial t} = \alpha_i \nabla^2 T \qquad i = l, s \tag{1 18}$$

where l and s represent liquid and solid phases respectively The Stefan condition is applicable at the interface where the brackets on the right indicate a jump condition

$$V_n L = -C_p \alpha_l [\vec{n} \cdot \nabla T]_{l-s} \tag{1 19}$$

The boundary condition in the liquid far from the interface is imposed as

$$T_{(l \to \infty)} = T_\infty - \Delta \tag{1 20}$$

and the interfacial temperature is given by

$$T_i = T_m(1 - d_0 \kappa) \tag{1.21}$$

where d_0 is a capillary length given by γ/L

In understanding the instability phenomenon, it is useful to begin with the simplest case, involving a planar interface as shown in Fig 1 2(c) Let the planar interface propagate in the y-direction with velocity V_n In coordinates translating with the interface, one seeks the temperature field $T(\xi)$, where $\xi = y - V_n t$ In these coordinates, assuming heat transport in the liquid only, the Eq (1 18) takes the form

$$\alpha_l \frac{\partial^2 T}{\partial \xi^2} = -V_n \frac{\partial T}{\partial \xi} \tag{1 22}$$

and the boundary conditions are

$$T(0) = T_m \tag{1.23}$$

$$LV_n = -\alpha_l \frac{\partial T(0)}{\partial \xi} \tag{1.24}$$

Solving, one obtains for the temperature in the liquid

$$T(\xi) = T_m + \frac{L}{C_p}(1 - \exp(-\frac{V_n \xi}{\alpha_l})) \tag{1.25}$$

The planar interface solution displays some curious features. First, the solution holds for arbitrary V_n. Thus, no information regarding the front velocity is available at this stage, a problem that recurs in other steady state solutions as well. Next, the unique undercooling at $\xi \to \infty$ is $\Delta = L / C_p$, consistent with heat conservation. For any other undercooling, a steady-state planar solution is not possible. This is to be expected since for other undercoolings there is a continuous accumulation of latent heat ahead of the interface. Not only does a steady-state planar solution not exist under most circumstances (an undercooling of $\Delta = L/C_p$ is very large compared to that imposed in most growth systems), the planar interface is also completely unstable. This can be shown by performing a linear stability analysis. Considering small perturbations of the form

$$\xi(x,t) = \zeta_k \exp(i\vec{k} \cdot \vec{x} + \omega_k t) \tag{1.26}$$

around the planar state and the solution in Eq. (1.25), one obtains a dispersion relation of the form

$$\omega_k = kV_n(1 - \frac{(1+\beta)}{2} d_0 \delta_T k^2) \tag{1.27}$$

where $\beta = \alpha_l / \alpha_s$ and δ_T is a thermal diffusion length $= \alpha_l / V_n$. Two features are evident from this relation. First, in the absence of surface tension, i.e. $d_0 = 0$, $\omega_k = kV_n$ and is always positive, implying an absolute instability of the front for perturbations of all wavelengths. Thus, in the absence of surface tension, there exists no stabilization mechanism on the interface and singularities such as cusps can develop. This is justifiable in that in the absence of capillarity the only length scale available in the system under consideration is the diffusion length α_l / V_n. There is no competing mechanism to set a length scale for the pattern. Upon introduc-

tion of surface tension into the analysis via the Gibbs-Thomson condition, perturbations sharper than

$$\lambda_c = 2\pi \sqrt{\frac{(1+f)d_0\delta_T}{2}} \tag{1.28}$$

will be suppressed. This can be seen by considering points A and B on the bulge shown in Fig. 1.2(c). When the curvature is large enough, $T_A < T_B$ so that heat flows from point B to A causing the bulge to flatten out. In other words the undercooling at point A is lower when compared to point B slowing point A down and causing a suppression of the instability. The wavelength given by Eq. (1.28) above sets the neutral stability point, i.e. $\omega_k = 0$ for this wavelength, which is the length scale first observed in the instability. This characteristic length scale is seen to be the geometric mean of the capillary length scale d_0 (typically of $O(\AA)$) and the diffusion length scale (approximately of O(mm)). Thus the instabilities are first observed at the length scale of a few microns.

In addition to the planar interface, the stability of other shapes such as spheres have also been studied (Mullins and Sekerka, 1963). In these geometries no steady-state shapes are obtained. The growth rate of a sphere is dependent on the radius, which is itself increasing with time. Furthermore, the spherical shape is also completely unstable. In fact, the only known steady-state interface shape solutions are paraboloids of circular and elliptic cross section. The existence of the former, first obtained by Ivantsov (1974), has greatly benefitted the study of dendritic growth. Much of the theory developed on the subject has relied on this model. These solutions are, however, approximations inasmuch as that due to the neglect of capillarity the paraboloids are isothermal. Briefly the Ivantsov paraboloids are obtained by solving the governing equations in parabolic coordinates translating with the tip velocity V_n, as shown in Fig. 1.6.

Defining the parabolic coordinates (ξ, η, θ) such that

$$\xi = \frac{(r - z)}{\lambda_c}, \quad \eta = \frac{(r + z)}{\lambda_c} \tag{1.28}$$

where r is the radial distance and λ_c is the tip radius of the paraboloid, the solution of the equations under the isothermal interface restriction yields the relation

$$\Delta = p \exp(p) \int_{p}^{\infty} E_1(p) \tag{1.30}$$

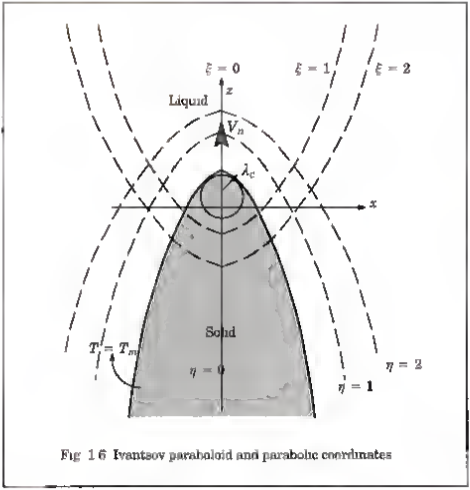

Fig 1 6 Ivantsov paraboloid and parabolic coordinates

where

$$E_1(p) = \int_y^\infty \frac{e^{-y'}}{y'} dy' \tag{1.31}$$

In Eq. (1.30)

$$p = \frac{\lambda_c V_n}{2\alpha_l} \tag{1.32}$$

is called the Peclet number. In the Ivantsov solution, Eq. (1.30), the imposed undercooling is expressed as a function of this Peclet number. An immediate consequence of Eq. (1.30) is that the undercooling determines uniquely the parameter p associated with a paraboloid. In other words, one can write the inverse relation

$$\frac{\lambda_c V_n}{2\alpha_l} = f(\Delta) \tag{1.33}$$

This brings to light the fundamental limitation of the Ivantsov model. Eq. (1.30) merely yields values for the product $\lambda_c V_n$, i.e. it determines a family of solutions corresponding to a Peclet number. Thus needle crystals of all possible tip radii are indicated as solutions. This problem was also encountered in the case of a planar front in the absence of surface tension. Much of the subsequent work on the dendritic growth phenomenon has been occupied with determining which of the needle crystals is actually selected in a particular growth environment.

Despite the missing crucial ingredient of capillarity, the faith reposed in the Ivantsov model has been vindicated by experiments (Huang and Glicksman, 1981; Trivedi and Somboonsuk, 1984). These efforts have shown that dendrite tips are indeed paraboloidal in shape. On this basis, various attempts were made to incorporate a correction to the Ivantsov model in order to include capillarity so as to select the tip radii and velocities (Kessler et al., 1988). Of these, the most successful attempt, by Langer and Muller-Krumbhaar (1978) – hereinafter referred to as LMK – invoked the issue of stability of the needle crystals to effect selection. A linear stability analysis around the needle crystal solution, in the justifiable limit

$p \to 0$, leads to a relationship of the form

$$\sigma^* = \frac{2d_0\Omega_1}{\lambda_c^2 V_n} \tag{1.34}$$

Thus, Eq (1 34), when combined with the Ivantsov relation, Eq (1.30), makes it possible to separate the quantities λ_c and V_n. The parameter σ^* is dependent on the material used and is associated with the anisotropy of the material. However, obtaining Eq (1 34) in itself does not fully solve the selection problem. Indeed, it is found that the capillary forces stabilize the tip for a range of σ^* above some critical value. Thus, one is still left with a continuous family of possible solutions. At this point LMK resort to a marginal stability hypothesis, whereby the operating point of the dendrite is argued to be such that the tip is marginally stable. For the popular organic material Succinonitrile, a value of $\sigma^* = 0\ 025$ was calculated, which is in close agreement with experiment (Huang and Glicksman, 1981, Muschol et al., 1992). Despite these close agreements, marginal stability remains a hypothesis, supported only by heuristic arguments rather than any sound theoretical basis. The model on which it is founded involves many simplifying assumptions. The mechanism by which marginal stability determines selection is not clear. The operating point of the dendrite involves highly complex, nonlinear behavior, especially in regard to the unsteady side-branching events away from the tip. The theory ignores side-branching and thus is of limited use in a realistic situation.

The fundamental shortcoming associated with most attempts at obtaining selection is the inclusion of surface tension as a perturbation to the Ivantsov needle crystals. A more recent view (Kessler et al , 1988) on the issue of pattern selection in dendritic growth is called the Microscopic Solvability Criterion (MSC). Here the effects of surface tension and anisotropy are incorporated in full from the outset. The initial ideas leading to the MSC arose in connection with simplified local models of dendritic growth, where much of the difficulties associated

with the nonlinearities and nonlocal behavior are circumvented (Brower et al , 1983) The insights obtained from these models were that in the absence of anisotropy dendrite tips become unstable to tip-splitting modes, while with sufficient anisotropy, stably propagating tips could be obtained. Thus, it became apparent that selection of the propagating dendritic primary branch calls for the inclusion of crystalline anisotropy

In order to understand how MSC operates, it is useful to cast the governing equations in integrodifferential form. According to Eq (1 19), an element of interface at (x', t') is a heat source of strength $L/C_p\ V_n(x',t')$ where $V_n(x',t')$ is the velocity of the element. Thus, the temperature field is obtained as the sum of the background temperature $T\infty$ and the superposition of all such heat sources at all previous locations of the interfacial points, propagated by the diffusion Greens function Thus

$$T(\vec{x}, t) = T_\infty + \int dS \int_{-\infty}^{t} dt\ G(\vec{x} - \vec{x}', t - t') \frac{L}{C_p} V_n(\vec{x}', t') \tag{1.35}$$

where dS' is a surface element and the diffusion Greens function is given by

$$G(\vec{x}\ t) = (4\pi\alpha_l t)^{-d/2} \exp(-\frac{\vec{x}\ \vec{x}}{4\alpha_l t}) \tag{1 36}$$

where d is the dimension of the surface element. The nonlocality in space and time is evident in Eq (1.35) Specializing to a two-dimensional interface and assuming a velocity V_n of the interface in the y−direction, one can write

$$\vec{x}' = (x\ y(x') + V_n t') \tag{1 37}$$

Evaluating Eq (1 35) on the interface and from the interfacial temperature given in Eq (1 21), one obtains after some manupulation

$$\Delta^* - \bar{d}_0\kappa = \frac{V_n}{2\pi\alpha_l} \int_{-\infty}^{\infty} dx' \exp[\frac{V_n}{2\alpha_l}(y(x') - y(x)] \\ K_0(\frac{V_n}{2\alpha_l}\sqrt{(x - x')^2 + (y(x) - y(x'))^2}) \tag{1 38}$$

where K_0 is a Bessel function, and the dimensionless quantities Δ^* and $\overline{d}_0$ are defined as

$$\Delta^* = \frac{(T_m - T_\infty)}{(L/C_p)} \tag{1.39}$$

and

$$\overline{d}_0 = \frac{d_0 T_m}{(L/C_p)} \tag{1.40}$$

In the limit of zero surface tension, i.e. $\overline{d}_0 \to 0$, and introducing parabolic coordinates one retrieves the Ivantsov solutions, Eq. (1.30). To select the appropriate needle crystal, it is necessary to retain surface tension and anisotropy. For example, assuming four-fold symmetry as in the case of Succinonitrile, which has a simple cubic structure, one can write

$$\gamma(\theta) = \overline{\gamma}(1 - \varepsilon \cos 4\theta) \tag{1.41}$$

After rescaling lengths by the diffusion scale ($2a_1/V_n$), one writes Eq. (1.35) as

$$\Delta^* - \gamma(\theta)\kappa = \frac{1}{\pi} \int_{-\infty}^{\infty} dx' \exp(y(x') - y(x)) \, K_0(\sqrt{(x - x')^2 + (y(x) - y(x'))^2}) \tag{1.42}$$

Eq. (1.42) can be used to obtain the interface shape $y(x)$ for a given undercooling Δ^* and material properties $\overline{\gamma}$ and ε. To do this, one can begin with the form

$$y(x) = -\frac{x^2}{2\rho} + z(x) \tag{1.43}$$

where the first term corresponds to the Ivantsov solution, wherefrom ρ can be obtained and $z(x)$ is a small correction. By substituting Eq. (1.43) in Eq. (1.42), $z(x)$ can be obtained as a function of (ρ, $\overline{\gamma}$ and ε). To do this, one integrates from the root of the dendrite (arclength $s = -\infty$ in Fig. 1.7) towards the tip ($s = 0$). Now, in general, when this is done for a given ρ, there will be a finite cusp at the origin. In order to select the allowed solutions, $\overline{\gamma}$ is to be varied so that the cusp at $s = 0$ vanishes. In the limit of small ρ which is physically reasonable, one can write Eq. (1.42) as

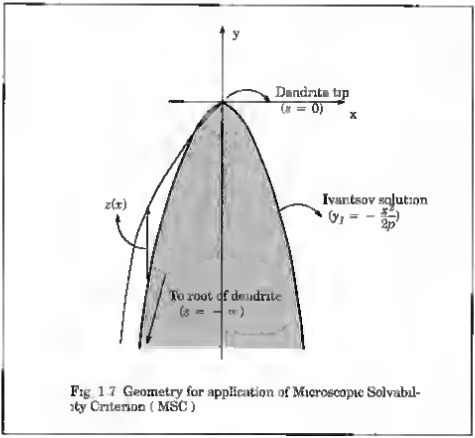

Fig. 1.7 Geometry for application of Microscopic Solvability Criterion (MSC)

$$\sigma(1-\varepsilon\cos 4\theta)\kappa = \frac{2}{\pi}\int d\kappa' \log\frac{(x-x')^2+(y-y')^2}{(x-x')^2+(x^2-x'^2)^2} \tag{1.44}$$

Solution of this equation for $\sigma(\varepsilon)$ gives the result, for small undercoolings,

$$\overline{\rho}(\rho\ \varepsilon) = \rho^2\sigma^*(\varepsilon) \tag{1.45}$$

where σ^* is the selected value. Written in dimensional terms, this implies that

$$V_n\lambda_c^2 = \frac{\overline{d}_0}{2a_1\rho^*(\varepsilon)} \tag{1.46}$$

This is the same form as that obtained by the marginal stability hypothesis. The individual quantities λ_c and V_n can therefore be obtained from Eq. (1.30) and (1.45) for given material properties $\overline{d}_0$, ε and imposed undercooling Δ. Thus, at this stage, upon inclusion of surface tension and anisotropy, it is possible to select

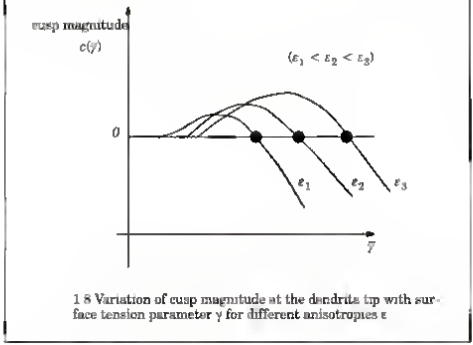

1 8 Variation of cusp magnitude at the dendrite tip with surface tension parameter γ for different anisotropies ε

a few discrete solutions from the Ivantsov continuum However, in reality, a unique tip radius and tip velocity are selected and this has to be achieved for the MSC to be any superior to the other *ad hoc* selection theories In particular the function $\sigma^*(\varepsilon)$ has to be quantitatively determined

It is clear that while surface tension is essential to set a length scale to the finally observed pattern, anisotropy is essential to the selection of a single pattern from the available continuum Hence, the macroscopic phenomena of capillarity and anisotropy set the observed patterns In fact the selection criterion gets its name from the fact that it is based on the solvability condition for zero cusp magnitude at $\varepsilon=0$ For example, if Eq (1.44) is solved for zero anisotropy, i.e. $\varepsilon = 0$, the cusp magnitude obtained at the tip does not vanish at any $\bar{\gamma}$, indicating that no steady-state tip solution is possible The behavior of cusp magnitude at $\varepsilon=0$ versus $\bar{\gamma}(p, \varepsilon)$, is illustrated in Fig 1 8 for non-zero values of ε There is a discrete set of

possible allowed $\bar{\gamma}$ or σ values, culminating in a maximum value These maximum values are indicated by the dots in Fig 1 8 The next step is to examine the available discrete solutions for stability When the linear stability is investigated, it turns out that for given (p,ε), the solution corresponding to the maximum value of $\bar{\gamma}(p, \varepsilon)$ is linearly stable, while for the lower allowed values in the discrete set, instabilities exist Thus linear stability dictates the unique observed patterns in dendritic growth The quantitative estimate of the parameter σ^* corresponding to the selected dendrite turns out for a crystal with four-fold symmetry to be approximately 0 02, a value in agreement with experiments with Succinonitrile (Huang and Glicksman, 1981, Muschol et al , 1992)

The MSC is still to be established as a complete theory for the selection of dendritic patterns in solidification It ignores effects such as interfacial kinetics and convection and relies on the restriction of small Peclet number or undercoolings. Furthermore, for highly anisotropic materials, its validity is questionable An example is Pivalic Acid (Rubinstein and Glicksman, 1990, Muschol et al., 1992), where the experiments seem to violate the condition $\lambda_c V_n^2$= constant, and it appears that the behavior is closer to $\lambda_c V_n$ = constant Xu (1988) has also questioned the boundary conditions applied at the root of the dendrite in obtaining the MSC. Thus the question of selection of dendritic solidification patterns is not fully resolved What is certain is that phenomena at the interface, such as surface tension and the lattice structure of the crystal formed, are crucial to any theory that attempts to explain such patterns

At this point, accepting that a criterion such as MSC appears to be necessary to effect selection, a further issue to be explained is the sidebranching phenomenon In nature, one does not encounter smooth needle crystals but a highly branched structure (Huang and Glicksman, 1981) As mentioned above, the tip

of the selected needle crystal is linearly stable The response of this selected tip to externally imposed or self-generated noise is believed to result in the observed sidebranches (Pieters and Langer 1986) At low anisotropies, i e low ϵ_4 the tip responds to external noise via tip-splitting, while at higher anisotropies, a steadily propagating tip persists, shedding sidebranches that are stationary in the lab frame, but receding away from the tip in the tip frame Analysis of the response of the tip to broadband noise indicates that the noise amplifies along the sides of the primary stem, and there is a most amplified frequency Ω^*, and an associated characteristic wavelength, this wavelength dictates the initial sidebranch spacing observed close to the tip This amplification of the noise is similar to that found in physical systems subject to convective instabilities (Huerre,1987, Diessler, 1985) Thus, while the noise is amplified down the sides of the primary dendrites resulting in sidebranches, the tip itself remains stable That crystalline anisotropy plays a significant role in this phenomenon can be demonstrated by imposing an artificial anisotropy, such as a grid on the Saffman-Taylor fingers (Ben–Jacob et al , 1985), whereupon sidebranches emerge on an otherwise unbranched finger The hypothesis of noise-induced sidebranch formation is supported by experiments of Dougherty et al (1987) where it has been shown that the sidebranches on either side of the dendrites are uncorrelated, indicating the noisy beginnings at the tip of the dendrite In contrast, in experiments of Bouissou et al (1990), an externally imposed oscillation causes expected resonant effects for a chosen frequency of oscillation and the resulting sidebranches are well correlated The sensitive nature of the tip of the dendrite, as well as the delicate effects of capillarity and lattice structure are crucial features in the theory of solidification patterns

1.3 Implications of Morphological Instabilities

Thus far we have summarized the current state of knowledge of dendritic growth in pure materials where the diffusion of heat controls the instability phe-

nomena. In alloys and semi-conductors which are grown by a variety of processes, the diffusion of solute is the limiting process and cellular and dendritic forms are observed on the growth front. The physics involved here is analogous to that described above. In the event of other control parameters entering the process by which solidification is obtained, such as in directional solidification, the instability phenomenon may become more complex (de Cheveigne et al., 1990) The origin of cellular forms in directional solidification is subcritical in origin, but results for the same reason as that in the pure material case, namely the propagation of the solidification front into a metastable supercooled melt For commonly employed alloys, the phase diagram is such that the solid rejects solute into the liquid phase In particular, there is an accumulation of such excess solute in the intercellular grooves and ahead of the growth front, leading upon complete solidification to an inhomogeneous solute distribution In addition, instabilities at the root of the cells may lead to the periodic shedding of droplets (Brattkus, 1989, Kurowski et al 1989) as shown in Fig 1 1, resulting again in non-uniform solute distribution At higher growth rates the cellular forms may transition into dendritic structures The mechanism for this transition is not well understood.

Even in the case of pure materials, the effects of convection on dendritic growth have not been well established and most models rely on purely diffusive field equations, although it has been demonstrated that both natural and forced convection in the melt can impact on the microstructure (Ananth and Gill, 1989, 1991, Boussou et al , 1990, Fang et al 1990, Ostrach, 1983, Tirmizi and Gill, 1987). The entire theory of pattern formation in solidification assumes that the interface is in local equilibrium, i e., it ignores kinetic effects The parameters associated with the kinetics of interfacial growth, such as rate constants interfacial energies, anisotropies and so on are difficult to measure or model, and these mechanisms have been largely ignored under the assumption of slow-moving in-

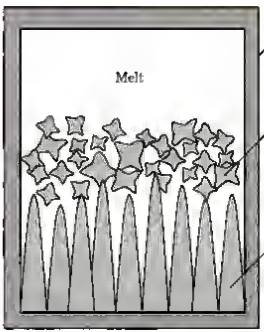

Fig. 1-9 Types of dendritic crystals in solidification from the melt The envelopes of the crystals are shown in both equiaxed as well as columnar cases

terfaces Other effects that may have significant impact on pattern selection in solidification include effects of confinement (Trivedi and Somboonsuk, 1984, Cladis et al , 1990), geometry of the growth domain (Fabietti et al 1990) and competition between orientations of heat transfer and crystalline anisotropy (Borisov et al., 1991)

Fig. 1 9 shows that dendrites can assume columnar or equiaxed forms, depending on their origin, i e depending on whether nucleation takes place on a substrate, such as a wall, or in the bulk of the melt A metallographic section can display distinct regions of grains resulting from columnar and equiaxed growth

and a transition between the two types It has been hypothesized that dendrite branch detachment from the columnar region and subsequent convection and growth in the melt can promote equiaxed growth (Beckermann et al , 1994) Beyond the formation of mature cells and dendrites several changes take place culminating in complete solidification In particular, in the late stages of dendritic growth, a phenomenon of *coarsening* or *ripening* occurs whereby the length scales of the solid structure increase (Huang and Glicksman, 1981) For example there is a progressive increase in sidebranch spacing Sidebranches in the vicinity of the tip of the primary dendrite are closely spaced, while the sidebranch spacing is greater away from the tip This coarsening of the sidebranch structure can occur via branch competition, whereby a sidebranch that is fortuitously longer than its neighbor suppresses the growth of the latter Alternatively, two neighboring sidebranches can merge with the same result All these phenomena are of utmost importance in determining the microstructures. The length and time scales involved are important to determine In particular, one needs to be able to predict the final primary dendrite spacing, length and velocity scales, the sidebranch spacing and its correlation if any to the primary dendrite characteristics These determine the dimensions of the envelope of the entire intricate branched structure corresponding to each dendrite This envelope forms a coherent, correlated structure and defines the all-important grain shapes and sizes of the solidified material Microsegregation, i e accumulation of impurities/solutes in the interdendritic regions leads, upon formation of the final grain structure, to a pattern of solute inhomogeneity The grain structure and resulting solute distribution govern the properties and performance of the metallic alloys or semiconductors

The above considerations impact significantly on the processes employed to produce crystals and have prompted single crystal growth techniques (Brown, 1988) and efforts aimed at mitigating the instabilities at the solid-melt interface

A desire to avoid instabilities may influence processing parameters which may conflict with the economy of the solidification processes. There have thus been extensive efforts to determine the effects of the macroscopic processing environments on the microstructure and *vice versa* (Beckermann and Viskanta, 1993, Ni and Beckermann, 1993, Rappaz, 1989, Thevoz et al., 1989, Tseng et al., 1991). With the computational facilities now available, the governing equations at the two levels are easily solved. The difficulty lies in modelling and computing the interactions of the different scales. It is a distinguishing feature of the solidification morphology problem that a plethora of scales are present from the atomic scales (O(Å)) to that of the growth environment (O(cm)). In the solution of the macroscopic equations, it is necessary to model the properties and behavior of the two phase zone, often called the *mushy zone* (Voller and Prakash, 1987). This region is comprised mainly of the morphological structures and adjoining liquid phase, and there appears to be no alternative but to perform averaging operations to model it. Even so, it is necessary that the scales, segregation patterns and solid fractions associated with each dendrite/cellular structure are quantified. The coupling between micro and macroscopic phenomena affect all these quantities. Investigation of the effects of macro phenomena such as convection, heat flow and boundary conditions, on the microstructure, whether experimental or analytical have been of a preliminary nature. Among efforts aimed at unifying the phenomena at different scales, the volume-averaged models of Beckermann and coworkers (Ni and Beckermann, 1993, Wang and Beckermann, 1993) and the solute diffusion models (Rappaz and Thevoz, 1987, Thevoz et al., 1989) are notable. These models incorporate solidification phenomena from the stochastic nucleation process to the macroscopic features of the solidified product. However, the details at each scale are either modelled or adopted from empirical correlations. The difficulties involved with the multiscale nature of the phenomena and the plethora of

nondimensional numbers which influence the physical phenomena at the different scales have thwarted attempts at arriving at an accurate representation of the physics. What is needed is the treatment of each scale separately and then to investigate their interactions. In this dissertation we attempt such a treatment of the overall solidification phenomena, with a systematic approach of constructing computational tools capable of solving the governing equations at all scales, by incorporating physics appropriate at each scale.

1.4. Concluding Remarks

The widely accepted results of morphological stability theory have been summarized in this chapter. Much of the theory is based on the Ivantsov needle crystal approximations, where the dendrite stem assumes the shape of a uniformly translating paraboloid. A selection principle is therefore necessary to establish the unique pattern observed in nature. The inclusion of surface tension and anisotropy are crucial to the emergence of selection from the governing equations. The theory of dendritic instabilities is by no means complete and several questions remain unanswered.

Interfacial instabilities at the solidifying front influence grain structure and distribution of dopants or impurities and hence the performance of solidified materials. In order to fully understand and control the effects of instabilities, investigations of the solidification processes at widely separated length scales are necessary. The complexities involved with the nonlinearities, moving boundaries and the microscopic nature of the instabilities has so far hampered both computational and experimental investigation. An effort is made in subsequent chapters to clarify the treatment of the various length scales and devise a computational method to simulate the solidification processes.

CHAPTER 2

MODELLING AND SCALING OF SOLIDIFICATION PROCESSES

2.1. The Demands on the Numerical Method

The phenomenon of morphological instability, as described in Chapter 1, places the following demands on a numerical procedure attempting to capture all the events leading to solidification from the melt:

1 The phase interface is a discontinuity in the flow field, temperature gradient and composition. Within the restrictions of finite grid resolution, the discontinuity needs to be tracked in time and space.

2 The interface is in motion under the influence of the gradients in the temperature and solute fields. Thus, accurate, efficient and robust field solvers are necessary in order to compute the interface location accurately.

3 The interface undergoes a succession of deformations leading to highly convoluted forms. Morphological instabilities can lead to cells and dendrites. Topological changes in the interface may result and the subsequent motion and growth of the disconnected or multiply-connected shapes may need to be followed. In the events leading to complete solidification several closed or open interfaces merge resulting in the eventual grain structure observed in metallographic sections.

4 The interface position is determined as part of the solution of the transport equations. They also form moving, internal boundaries for the field solver, with Dirichlet as well as Neumann conditions applied thereupon. The interface shape is then obtained from the interaction of transport processes in the bulk and capil

lary effects on the interface. In particular the interfacial temperature according to the Gibbs-Thomson condition is a function of the local curvature. Thus, it is imperative that such interfacial features as slopes and curvatures be obtained with sufficient accuracy.

In subsequent chapters, we will design a computational framework that can satisfy the above requirements. In order to motivate this fresh approach to simulation of interfacial instabilities, it is useful to review the available techniques and to draw from their shortcomings and strengths. This is done in the following section.

2.2. Numerical Methods Applied to General Moving Boundary Problems

Several techniques exist for tracking arbitrarily shaped interfaces, each with its own strengths and weaknesses(Crank, 1984, Floryan and Rasmussen, 1989). These techniques may be classified under two main categories: (a) Surface tracking or predominantly Lagrangian methods and (b) Volume tracking or Eulerian methods. The main features of the two types are presented in Fig. 2.1. In the Lagrangian methods, the grid is configured to conform to the shape of the interface and thus adapts continually to it. The Eulerian methods usually employ a fixed grid formulation and the interface between two phases is not explicitly tracked but is reconstructed from the properties of appropriate field variables, such as fluid fractions. Based on these basic differences in approach of the two classes of methods the following comparisons can be made.

2.2.1. Interface Definition

The Lagrangian methods maintain the interface as a discontinuity and track its evolution explicitly. If detailed information regarding the interface location is desired, Eulerian methods may need elaborate procedures to deduce the interface location based on the volume fraction information, and uncertainty cor-

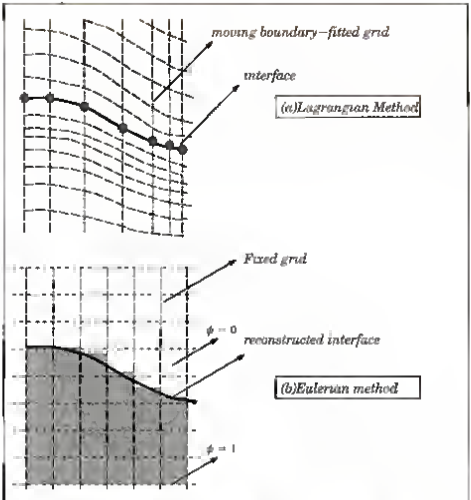

Fig. 2.1. Comparison of Lagrangian and Eulerian methods for interface tracking. (a) Purely Lagrangian method with a moving, boundary conforming grid. (b) Fixed grid Eulerian method with a phase fraction definition of the interface.

responding to one grid cell is unavoidable (Ashgriz and Poo, 1991, Liang, 1991, Hirt and Nichols 1981) In the Lagrangian case the interface can be tracked as an $(n-1)$-dimensional entity for an n-dimensional space (Glimm et al , 1988, 1986, Degregoria and Schwartz, 1985, Miyata, 1986) No modelling is necessary to define the interface or its effect on the flow field. In the case of Eulerian

schemes, modelling or the solution of additional equations is required to obtain information regarding fluid fractions or other functions yielding information in the two-phase regions

2.2.2. Interfacial Boundary Conditions

In the Lagrangian methods boundary conditions can be applied at the exact location of the interface since the interface position is explicitly known at each instant In the Eulerian methods, the boundary conditions are manipulated to appear in the governing transport equations (Brackbill et al., 1992). This leads to smearing of boundary information

2.2.3. Discretization of the Domain

In the Lagrangian methods, the grid adapts to the interface and hence grid rearrangement and motion terms have to be incorporated When the interface begins to distort the grid needs to be regenerated each time, which may require the solution of another equation(Thompson et al , 1985) The resulting grid on which the field variables are computed may be skewed and unevenly distributed, thus impacting on the accuracy of the field solver. The Eulerian methods are at an advantage in this regard since the computations are performed on a fixed grid, hence obviating the need for grid rearrangement However, when the interface is arbitrarily shaped, improved resolution in desired regions is difficult to obtain, unless complicated local refinements are adopted

2.2.4. Topological Changes of the Interface

Lagrangian methods have so far experienced difficulty in handling topological changes, mainly due to the breakdown of the structured grid arrangement and the need for redistribution of field information in the vicinity of the interface for unstructured grid methods On the other hand, in Eulerian methods mergers and fragmentations are taken care of automatically, merely by the updated values of the fluid fraction field However, the detailed physical features involved during

such events may not be fully resolved due to the smearing of information mentioned above

2.3. Choice of Method – Lagrangian or Eulerian ?

The choice of method, i e , Lagrangian or Eulerian, is dependent on the physical problem under investigation If details of the interface are secondary, or are unlikely to significantly impact on the global flow features, the Eulerian methods are more attractive. If the discontinuity across the interface is to be maintained with fidelity, and interfacial behavior is in focus, Lagrangian methods hold an advantage Hitherto, Lagrangian methods have faced the barrier of topological changes of the interface If it were possible to combine the strengths of the fixed grid and explicit interface tracking ideas and devise a scheme to circumvent the logical hurdles in the events of merger or breakup of interfaces, a method of broader applicability would result

2.4. Review of Available Methods for Moving Boundary Problems

Under the broad categories of Lagrangian and Eulerian methods the following numerical techniques have thus far been developed by researchers in the area of moving boundary problems

1. Transformation Methods. In such methods the irregular physical boundary is mapped into a regular computational domain where the solution of the equations is performed In Chapter 3, for the simulation of morphological instabilities in crystal growth, we will devise a body fitted moving grid solver with generalized curvilinear coordinates to follow the motion of the phase boundary However, as with most mapping methods, the calculations experience difficulties when the interface becomes multiple-valued (Brush and Sekerka, 1989, Ungar and Brown, 1984) It is of course possible to generate boundary-conforming grids beyond this stage, say by solving partial differential equations in each phase (Thompson et

al , 1985) The added expense of solving these equations is undesirable. The boundary fitted grid will also experience difficulties in the form of grid skewness under severe interface convolution and will need to be reconfigured under topological changes of the interface Such events will therefore need to be identified and dealt with, a process that will involve much logical and algorithmic complexity Furthermore, the grid points and values of the field variables will have to be redistributed in the vicinity of the interface, which may lead to numerical diffusion Finite element methods with domain decomposition have also been applied to capture the deep cell regime by Ungar and Brown (1984) The restrictions mentioned above regarding the need for remeshing apply to these simulations

2. Boundary Element Methods (BEM) Due to the facility offered by the BEM in terms of the reduction of the dimensions of the problem, it has been extensively employed in front tracking. Dendritic structures (Sato et al , 1988, Strain, 1989) and Saffman-Taylor fingers (DeGregoria and Schwartz, 1985, 1986) have been simulated with considerable success While the BEM is unquestionably well suited for problems with linear field equations, the application to nonlinear problems with convection and for physical situations involving time-dependent boundary conditions (Beunssen et al , 1990, Fabietti et al , 1990) and topological changes is not straightforward.

3. Volume–tracking methods The volume–tracking (Eulerian) methods differ fundamentally from the surface-tracking (Eulerian Lagrangian) methods discussed above in that the interface is not explicitly defined or tracked but is reconstructed at every step (Hirt and Nichols, 1981, Smith, 1981 Youngs, 1984) The Volume of Fluid (VOF) method has been popular where a fluid fraction variable F, assigned values of 1 and 0 in the two phases, is calculated as a field variable over the domain The interfacial cells are then identified as those with fractional values of F The volume fraction is then advected with the local flow velocity. Over the

years accurate fluxing schemes for advecting the volume fractions have been developed extensively for dealing with passive liquid-gas interfaces (Ashgriz and Poo, 1991, Liang, 1991, Kothe and Mjolsness, 1992, Brackbill et al., 1992) The most striking disadvantage of the volume tracking schemes is that while mergers and breakups of the interface can be detected, they can not be treated with precision The complications pertain to the reconstruction of the interface which involves considerable logical operations Only recently, a technique to impose surface tension effects in an efficient manner has been developed (Brackbill et al 1992) in which the boundary conditions on the interface are assigned in a weighted fashion to the computational nodes in the vicinity of the interface, instead of being applied on the boundary Volume tracking methods have been applied to complex interfacial phenomena, including droplet dynamics and breakup, morphological instabilities in crystals (Smith, 1961) and spray dynamics (Liang, 1991) In applications where the broad features of interfacial behavior are required to be extracted the VOF methods have been widely used. The capability of this approach in resolving the shape and irregularity of the interface with required accuracy needs to be improved

4. The level set method . Notable among new approaches to interface evolution problems, in particular reference to morphological instability is the level set Hamilton-Jacobi formulation (Osher and Sethian 1985, Sethian, 1990, Sethian and Strain, 1992). We now describe the basic features of such an algorithm.

As shown in Fig 2 2 , a variable called the distance function ϕ is defined on the domain, where initially $\phi(x,t)$ = distance from x to $\Gamma(t=0)$, the initial interface location. On this level set, the interface at any instant corresponds to the contour $\phi = 0$ A particle on the level set is advected according to the equation

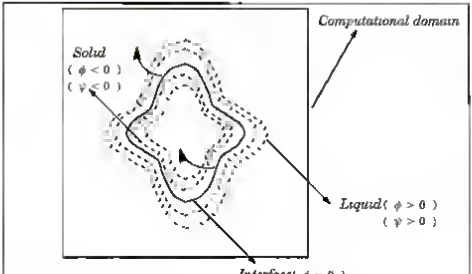

Fig 2.2 Illustration of computational domain and definition of distance function ϕ for the level−set formulation and phase variable ψ for the phase field method

$$\phi_t + \frac{\partial \vec{x}}{\partial t} \nabla\phi = 0 \qquad (2\,1)$$

and

$$\frac{\partial \vec{x}}{\partial t} \vec{n} = F \qquad (2\,2)$$

where F is a speed function evaluated at each point on the Cartesian grid. Thus, the equation governing contour evolution is

$$\phi_t + F|\nabla\phi| = 0 \qquad (2\,3)$$

and the initial interface shape as defined by the contour $\phi(x,t=0) = 0$ is specified. In the work of Sethian and Strain (1992) F, the speed function, is a globally defined variable, which reduces to V_n, the normal speed of the phase front contour for $x \in \Gamma(t)$. $\mathbf{F}$ is obtained by extending smoothly the expression for $V_n(x,t)$,

$$\varepsilon_c(n)C + \varepsilon_\gamma(n)V_n + T + H\int_I \int_{\Gamma(\tau)} K(x,x',t-t')V_n(x',t')dx'dt' = 0 \qquad (2\,4)$$

which applies for $x \in \Gamma(t)$. In Eq. (2.4) the integral is the travelling source term lo-

cated on the interface T is the local temperature, κ is the local curvature of the front, evaluated from the gradients of the level set, and ε_c and ε_v are factors controlling capillarity effects and kinetics respectively. This integral depends on the history of the interface motion, apart from its geometry. The level set equation is solved with an hyperbolic conservation law approach to obtain entropy-satisfying discretizations. By using the level set method, highly distorted, even three-dimensional interfaces have been obtained for the solidification problem. As with other purely Eulerian methods topology changes are incorporated automatically. However, the method as it stands is predicated on the existence of a kernel for the diffusion field. For highly nonequilibrium phenomena with arbitrary boundary conditions and inhomogeneous materials and convection in the melt, the applicability of the method needs further assessment.

5. Moving unstructured boundary–conforming grid methods: In a recent effort Unverdi and Tryggvason (1992) have employed a moving unstructured boundary-conforming grid in combination with a stationary Cartesian grid to track the motion of bubbles undergoing severe deformation. The method is similar in spirit to the front tracking schemes applied by Glimm et al. (1986) to the Rayleigh-Taylor instability. In each case, the boundary-conforming requirement of the grid leads to grid readjustment procedures close to the interface. In addition, in Unverdi and Tryggvason (1992), following Fauci and Peskin (1988), the surface tension effects on the interface are transmitted in the form of a force f_s to the underlying Cartesian grid, based on a weighting procedure. Thus, although the boundary–conforming grid avoids numerical dissipation at the interface, with respect to the field solver, the interface location is still not exactly specified.

6. Phase field methods. Phase field models (Kobayashi, 1993, Wheeler et al., 1993) have recently gained much attention and have succeeded in generating realistic solidification microstructures. In this method, as shown in Fig. 2.2, a phase field

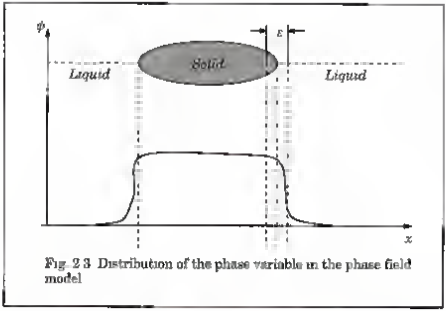

Fig. 2.3 Distribution of the phase variable in the phase field model

variable ψ is defined on a fixed grid. ψ assumes discrete values of 1 in the solid and 0 in the liquid. The distribution of the variable is as shown in Fig. 2.3.

The basis of the method lies in expressing the free energy of the system as a Cahn-Hilliard functional (Cahn and Hilliard, 1958, Penrose and Fife, 1990). For a general non-uniform system it is expected that the local free energy f per molecule will depend both on local composition and the composition of the surrounding environment. Thus, f can be expressed as the sum of the local composition c and the local composition derivatives, respectively. If f is a continuous function with respect to c and the gradients of c, then a Taylor series expansion around f_m, the free energy of a solution of uniform composition, yields

$$f(c, \nabla c, \nabla^2 c, \ldots) = f_o(c) + \sum_i \frac{\partial f}{\partial(\frac{\partial c}{\partial x_i})_o}(\frac{\partial c}{\partial x_i}) + \sum_{ij} (\frac{\partial f}{\partial(\frac{\partial^2 c}{\partial x_i \partial x_j})_o})(\frac{\partial^2 c}{\partial x_i \partial x_j}) \quad (2.5)$$

Under certain simplifying assumptions, Eq. (2.5) reduces to

$$f(c, \nabla c, \nabla^2 c) = f_o(c) + k_1 \nabla^2 c + k_2(\nabla c)^2 + \ldots \quad (2.6)$$

Thus, the free energy in a non-uniform system is a sum of local and a *gradient energy* contribution. The local Helmholtz free energy density f, is postulated on

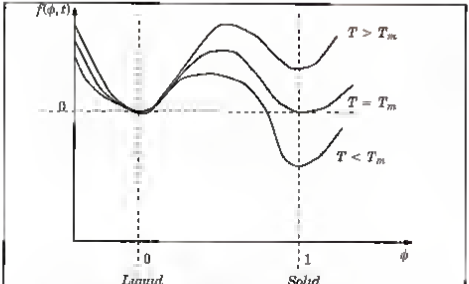

Fig 2 4 Free energy density f (Kobayashi, 1993) as a function of the phase fraction for different temperatures

a double-well function with two distinct minima each corresponding to a phase, as in Fig. 2 4. Integrating over a volume V, we obtain the total free energy of the system from

$$F = N_v \int_V f dV \tag{2 7}$$

where N_v is the number of molecules per unit volume. At equilibrium one expects the functional F defined in Eq. (2 7) to be a minimum with respect to variations in ϕ, and ϕ then satisfies the Euler-Lagrange equation

$$\frac{\delta F(\phi(\vec{x}))}{\delta \phi(\vec{x})} = 0 \tag{2 8}$$

This simplifies to

$$\frac{\delta F(\phi(\vec{x}))}{\delta \phi(\vec{x})} = f'(\phi(\vec{x})) - b\nabla^2 \phi(\vec{x}) \tag{2 9}$$

where b is a constant. The kinetics of the function $\phi(x, t)$ is usually assumed to follow

$$\frac{\partial\phi(\vec{x},t)}{\partial t} = -B\frac{\delta F(\phi_i(\vec{x}))}{\delta\phi_i(\vec{x})} = B(b\nabla^2\phi_i(\vec{x}) - f'(\phi_i(\vec{x}))] \qquad (2\ 10)$$

where B is positive always and may depend on ϕ and the temperature Eq (2 10) implies that the free energy decreases along solution paths, i.e., the free energy is a Lyapunov functional The equations solved then are the heat conduction equation with a source term accounting for latent heat evolution

$$\frac{\partial T}{\partial t} - L\frac{\partial\phi}{\partial t} = \nabla^2 T \qquad (2\ 11)$$

where L is the latent heat, and the equation for the evolution of the phase field

$$a\xi^2\dot{\phi}_i = -\frac{\delta F}{\delta\phi} = \xi^2\nabla^2\phi + \frac{1}{2a}\phi(1-\phi^2) + 2T \qquad (2\ 12)$$

where $T=0$ is the phase transition temperature, a and ξ are constants Here the Helmholtz energy functional used is

$$f(\phi\ t) = \frac{1}{8a}(\phi^2-1)^2 - 2T\phi \qquad (2\ 13)$$

which displays the double-well functional behavior

The solution of these equations leads to the development of realistic solidification patterns The phase field model thus yields excellent qualitative results However, in a most general situation, the basis of the model is questionable In a nonequilibrium situation the free energy may no longer be a Lyapunov functional In fact, a minimization principle may not even hold (Langer, 1981). Furthermore, it is difficult to correlate the several constants and parameters involved in the model to real physical systems One has to balance the need for an extremely fine grid resolution to capture sharp interfaces with stability considerations for time-stepping Thus, the phase field approach cannot be regarded as a simulation technique for a general solidification process.

As far as the microstructural evolution is concerned, computations thus far have been restricted to diffusion-controlled growth Under this restriction, several of the numerical techniques mentioned above are applicable in solving the full governing equations or simplified models In the early 1980s deep insights into

the physics of the instabilities were obtained using local models for the interface evolution (Brower et al., 1987) These models essentially amounted to computing the dynamics of strings under curvature dependent motion, and no account was taken of the long range behavior of the thermal field Fixed-grid techniques have been applied to the solidification problem, with considerable success at the macroscopic scale. These techniques usually employ variants of the entropy-porosity formulation (Shyy and Rao, 1993,Voller and Prakash, 1987) At the microscopic scales two useful methods are the aforementioned level set Hamilton-Jacobi formulation and the phase field models.

2.5. Micro and Macroscopic Modelling of Solidification Phenomena for Pure Materials

The multi-scale nature of the solidification process has been described in Chapter 1 As explained above, the enthalpy-porosity based Eulerian methods are well suited and have been extensively used for the simulation of the macroscopic flowfield and phase front. In this method the two-phase region is treated as a mushy zone whose thickness depends on an adjustable parameter ε Smearing of the two phase zone is necessary from stability considerations, so as to enable handling of the discontinuity However, in many cases, this smearing issue can be largely circumvented by appropriately formulating the algorithm so that very small values of ε are acceptable from a stability point of view. In this process the information regarding the intricate nature of the microstructure is simply averaged into the information contained by f_s , the solid fraction in the two-phase region In recent years, considerable effort has been expended in constructing a more accurate model for the microstructure in order to obtain a more realistic estimate for f_s (Beckermann and Viskanta, 1993, Rappaz, 1989, Tseng et al., 1992) Such attempts have been called micro-macroscopic modelling In the absence of direct simulations and adequate experiments performed at the microstructural

level, details regarding the behavior of the phase interface have been treated in a *lumped* or *volume-averaged* fashion and fed into the macroscopic models. Solute diffusion models (Rappaz and Thevoz, 1987, Thevoz et al., 1989) and volume-averaged models (Wang and Beckermann, 1993) of the microsegregation patterns depend on the information from the global flow field, which also determines local nucleant density based on cooling rates. Thus, employing currently available theoretical and analytical results the microstructure behavior, including columnar, equiaxed and globulitic structures have been modelled, in the spirit of modelling for turbulent flow computations. It is questionable whether and if the details of microstructure impact in any significant fashion on the macroscopic computational aspects at all, if the only information extracted from the microstructure is related to effective viscosities, conductivities, phase fractions and the like. This is particularly so in view of the need to assess the relative importance of the numerical and physical viscosities present in most studies. Furthermore, many of the models currently employed at the microscopic level are based on diffusion-controlled growth, an idealization inapplicable under many practical processing arrangements where convection is important.

A few of the key features of the microstructure that are to be predicted by a satisfactory model are

a) primary dendrite arm spacing, tip radius and velocity

b) dendrite secondary arm spacing, tip radius and velocity

c) dendrite/cell orientation with respect to convective and diffusive heat flow

d) interdendritic flow / microsegregation

e) grain sizes, both in the columnar and equiaxed cases

f) conditions for the transition between columnar and equiaxed growth (CET)

g) dendritic settling velocities for equiaxed shapes and the two-phase flow behavior

Such information is extremely difficult to obtain via experimentation due to the length scales in question What is required is a numerical simulation technique that can provide information regarding such features In section 2 4, we described several available techniques that could be applied to address the issues presented above. In view of the limitations of the methods developed thus far, there is a need for a numerical technique that can compute phase change phenomena at all scales The information obtained from the micro-scales, which may be regarded as a sub-grid model may then be supplied to the macroscopic flowfield calculations In this dissertation, the foundation is laid down toward developing such a comprehensive micro-macro model In this model, a crucial feature is to devise the communication between the micro and macroscopic models Thus, in investigating the effects of a macroscopic flowfield on the microstructural features and *vice versa*, it is necessary to obtain appropriately scaled formulations at each level and to match the evolution of each domain in time, space and structure (Bejan, 1992, Favier, 1990, Garandet et al., 1990) This situation is illustrated in Fig 2.5

2.6. A Typical Scaling Analysis

We now present an example of a scaling procedure that enables information transfer from the macroscopic to microscopic scales It may be noted that the scaling performed here is restricted to the particular configuration chosen below and is applicable to a pure material In the case of impure materials/alloys the scaling is considerably more complicated due to the addition of other competing effects and control parameters However, the nature of procedures required is along the lines of the model employed in the following

Let us assume the growth configuration shown in Fig 2 5 for the solidification/melting of a pure material. Let the domain size be defined by the length H Let, as in the experiments of Glicksman et al (1976), a global undercooling of A

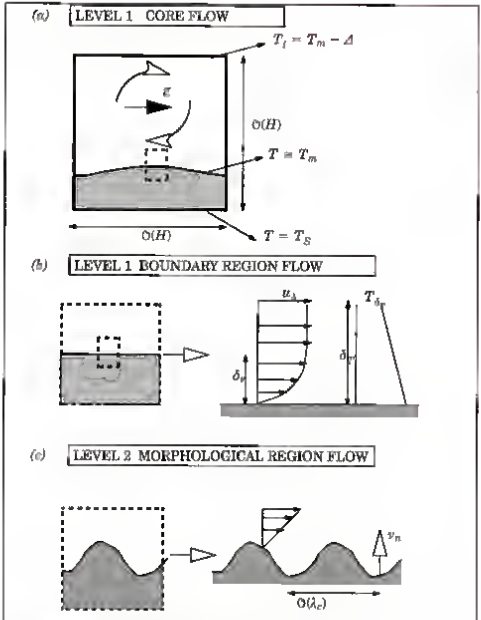

Fig. 2.5 Illustration of the levels involved in analysis of convective effects on microstructure evolution (a) Level 1 – core flow (b) Level 1 – flow near the macroscopic interface (c) Level 2 – flow at the morphological level

be imposed and T_m be the melting temperature The flow is assumed to be purely buoyancy-induced Sources of forced convection, although inherent in any realistic solidification process, are ignored Estimates for the scales at various levels will be obtained based on these imposed conditions and the material properties The following non-dimensional quantities may be defined for the situation illustrated

$$Pr = Prandtl\ number = \nu_l/\alpha_l \tag{2 14}$$

$$Ra = Raylegh\ number = \frac{g\beta_l\ \Delta H^3}{\alpha_l\ \nu_l} \tag{2 15}$$

$$Gr = Grashof\ number = Ra \cdot Pr \tag{2 16}$$

$$St = Stefan\ number = \frac{\Delta}{L/C_p} \tag{2 17}$$

In the above, β, α_l, ν_l, L and C_p are respectively the thermal expansion coefficient, thermal diffusivity, kinematic viscosity, latent heat and specific heat at constant pressure, and the subscript l corresponds to liquid phase The non-dimensional numbers for an organic melt and for a metallic melt are listed in Table 2 1 below

Table 2 1 Non–dimensional numbers for two frequently used materials Succinonitrile–Acetone is an organic mixture, while Lead–Tin is a metallic alloy (ν_l is the kinematic viscosity, α_l is the thermal diffusivity and D_l is the mass diffusivity).

Number	Succinonitrile–Acetone	Lead–Tin
Prandtl number (ν_l/α_l)	23	1.2×10^{-2}
Lewis number (α_l/D_l)	89	6.7×10^{3}
Schmidt number (ν_l/D_l)	2055	81

Two levels may be distinguished in the growth configuration Firstly (level 1 in Fig 2 5 (a)), there is a global or outer flow that occurs on account of buoyancy at the overall growth dimension H The balance of terms in the momentum equa

tion here may be taken to be between inertia and buoyancy forces This forms the core flow At the same macrosopic level, close to the solid-liquid interface (Fig. 2 5(b)), there are regions where diffusion of momentum predominates and balances the inertia/buoyancy terms While cross-stream diffusion is important, this region may not be a boundary layer in the classical sense The necessity for an intermediate length scale corresponding to the boundary region flow shown in Fig 2 5 (b) arises when $H > O(\lambda_c)$ This wide disparity in scales is usually encountered in solidification arrangements. Then the instability scale perturbations during inception and growth may not be subjected to the core flow, and it is more likely that the instabilities lie in the boundary region where diffusion is the predominant transport mechanism For other growth conditions when convection is not strong enough, a distinct intermediate layer may not exist In that case, the matching of the microscopic or inner region may be performed directly with the core flow The morphological scales represent the next level as shown in Fig 1 5(c). The scales at this level are determined based on pattern formation theory which assumes a diffusion dominated situation The critical feature at this scale is the interaction of heat conduction, latent heat release at the moving boundary and capillarity effects. To determine the effects of fluid flow at the global level on the microstructure, it is necessary to establish communication between the two levels with/without an intermediate layer, i.e the boundary region A sample scale analysis is presented here.

2.6.1. Level I. The Outer Scales

For the outer flowfield the length scale X_g, $Y_g = H$ and the temperature scale $\Delta = (T_l - T_m)$ The subscript g indicates a global scale T_l is the imposed constant temperature at the boundary of the liquid phase as shown in Fig 2 5 The velocity scale along x-direction U_g, is obtained from considering the balance of transport terms in the continuity and momentum equations. Continuity indi

cates that the y-direction flow velocity $V_g = O(U_g)$ Considering the momentum equations, and eliminating pressure by cross-differentiation, we obtain for balance between convection and buoyancy terms a buoyancy velocity scale

$$U_g = \sqrt{g\beta_l \Delta H} \tag{2 18}$$

Thus, the outer time scale is

$$\tau_g = \frac{U_g}{H} = \sqrt{\frac{g\beta_l \Delta}{H}} \tag{2 19}$$

Applying Eq (1 17), the velocity scale of interface motion as viewed at the outer scale is

$$V_{n_g} = \frac{k_l}{\varrho_l} \frac{\Delta}{H} = \frac{\Delta}{L/C_0 H} \frac{\alpha_l}{H} = \frac{\alpha_l}{H} St \tag{2 20}$$

This interfacial velocity scale is based on the macroscopic perspective in which the interface is only mildly deformed The interface is then driven by the gradients of the temperature field, and the diffusion of latent heat determines the extent of the temperature boundary layer and hence the front velocity It may be noted that at the level of the microstructure a selection principle is employed to estimate the front velocity At that scale the application of the selection principle described in Chapter 2 incorporates the crucial effects of capillarity and anisotropy, aspects which may be safely ignored at the macroscopic level The ratio of the front velocity in Eq (2 20) to the fluid flow velocity is obtained from

$$\frac{V_{n_g}}{U_g} = \frac{StH}{\delta_T \sqrt{\mathrm{Pr}\, Ra}} \tag{2 21}$$

For the small St and large Ra commonly encountered in solidification processing Eq (2.21) indicates that the interfacial velocity scale is such that $V_{ng} < O(U_g)$ Thus, at the outer scales the quasi-stationary assumption is reasonable The interface is thereby assumed to move slowly enough that its motion can be neglected in comparison to the fluid flow velocities.

2.6.2. Level I. Flowfield in the Interface Region

As a next step we require scales in the region near the solidifying/ melting interface. If such a region exists, the physical mechanisms that balance are diffusion and inertia/buoyancy. The matching between the core flow and the microscopic scales will have to be performed through this region. Hence, this boundary region will form an intermediate layer between levels I and II. In this boundary region estimates are required for:

1. δ_v, the intermediate viscous scale
2. δ_T, the intermediate thermal length scale
3. U_{δ_T}, the velocity scale in the thermal layer
4. U_{δ_v}, the velocity scale in viscous layer
5. Δ_δ, the temperature scale in the intermediate layers, appropriately subscripted to indicate the length scale in question.
6. τ_I, the time scale in the intermediate layer

These quantities are to be obtained in terms of the global quantities Δ, H and material properties, or alternatively in terms of the non-dimensional numbers in Eqs. (2.14 – 2.17).

Although as mentioned before the flows in the intermediate layers may not necessarily correspond to boundary layers, but merely represent a region where diffusion plays a dominant role, some features of boundary layers need to be noted. In the classical boundary layer theory, depending on the Prandtl number very different scenarios are possible as illustrated in Fig. 2.5. Such a distinction is important to make, since the Prandtl numbers for metallic melts and the organic melts used to model their behavior are vastly different (Table 2.1). Thus, care must be exercised in extrapolating results from experiments involving organic melts to metals, particularly when convective effects are involved. Here we obtain estimates for the above scales for each case.

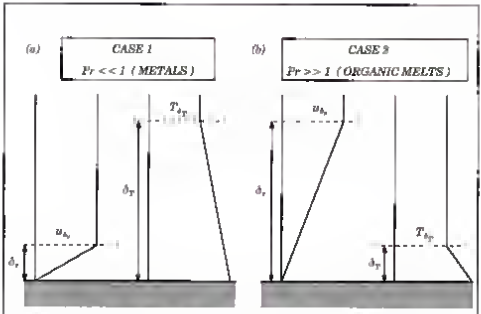

Fig 2 6 Illustration of the boundary layer types for different Prandtl numbers (a) Case 1 Metallic melts. (b) Case 2. Organic melts used to model the former

Case 1 (Metallic Melts) : The following conditions apply

$$Pr < O(1) \tag{2.22}$$

which implies that

$$\delta_T > O(\delta_v) \tag{2.23}$$

Hence from Fig 2 6 we estimate that

$$U_{\delta_T} = U_g = U_{\delta_v} \tag{2 24}$$

i e in the bulk of the temperature boundary layer the velocity scale = $U_g = U_{\delta v}$

Case 2 (Organic melts) : The scales are obtained as follows

$$Pr > O(1) \tag{2 25}$$

and

$$\delta_T < O(\delta_v) \tag{2 26}$$

Hence the appropriate velocity scale in the thermal boundary layer is given by

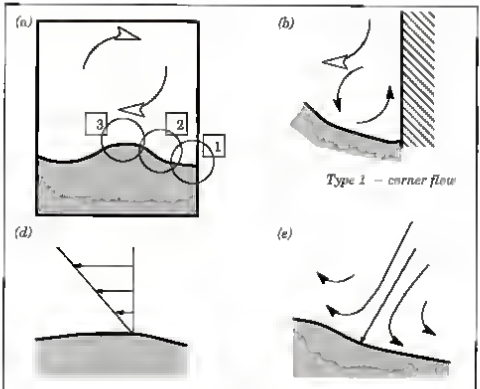

Fig 2 7 Flow features in a typical solidification arrangement (a) The macroscopic interface (b) type 1– corner flow (c) type 2– stagnation point flow (d) type 3 – boundary layer flow along a curved surface

$$U_{\delta_T} = \frac{\delta_T \; U_{\delta_T}}{\delta_v} = \frac{\delta_T \; U_g}{\delta_v} \qquad (2\,27)$$

Consider a typical solidification arrangement shown in Fig 2 7 In this arrangement the core flow is driven by buoyancy Different types of flow situations may be encountered depending on the global flow characteristics (Ostrach, 1983, Davis, 1990, Favier, 1990). These situations are illustrated in the figure In type 1, there is a corner flow situation and the microstructures formed in this region will be strongly influenced hy wall effects In type 2, a stagnation point flow arises between counterrotating vortices in the bulk flow In type 3, a boundary layer over

the curved macroscopic interface is encountered for Gr > O(1). Thus, several estimates of the flow characteristics and intermediate scales for the flowfield are relevant. It is clear that in any realistic arrangement, different regions of the macroscopic interface and hence the microstructures there experience a variety of transport phenomena. In addition, depending on the forces driving fluid motion, the interface can experience different conditions from onset to fully-developed flow (Davis, 1990, Davis et al., 1984, Favier and Rouzaud, 1983, Forth and Wheeler, 1989, McFadden et al., 1984). In what we are presenting therefore, we limit ourselves to the situation in type 2 shown in Fig. 2.7(d) in order to investigate the coupling of the global and microscopic level transport processes in their simplest form.

2.6.2.1. Scales in the intermediate viscous layer

Applying the usual boundary layer considerations, we can write the scales in the viscous boundary layer as

$$X_{\delta_v} = H \tag{2.28}$$
$$Y_{\delta_v} = \delta_v \tag{2.29}$$

where the subscripts represent the scales in the intermediate viscous layer of extent δ_v. The continuity equation yields, for the velocity along y-direction

$$V_{\delta_v} = \frac{\delta_v}{H} U_{\delta_v} \tag{2.30}$$

This assumption is predicated on the condition that $V_{n\delta v} < O(V_{\delta v})$, i.e. that the velocity of the interface, as viewed from within the intermediate layer is negligible compared to the v-component of the flow velocity there. The validity of this assumption depends on the ratio between the interface velocity as viewed from the viscous layer $V_{n\delta v}$ and the fluid flow velocity in that region given by Eq. (2.30).

$$\frac{V_{n\delta_v}}{V_{\delta_v}} = \frac{\left(\frac{St\ a_f}{\delta_T}\right)}{\left(\frac{\delta_v}{H} U_{\delta_v}\right)} = \frac{St\ a_f}{\delta_T} \frac{\sqrt{\mathrm{Re}}}{\sqrt{\varepsilon}\ \beta_f\ \Delta H} \tag{2.31}$$

where δ_T is the intermediate thermal length scale. In Eq. (2.31) it has been as-

sumed that

$$V_{n\delta_v} = \frac{St}{\delta_T}\,\alpha_l \tag{2 32}$$

since the interface is driven by gradients of the temperature field and this field relaxes over an extent δ_T Therefore as far as the interface motion is concerned the length scale used for computing the temperature gradients should be the thermal layer thickness δ_T The second equality results from the well known fact that the viscous boundary layer follows the scale

$$\delta_v = \frac{H}{\sqrt{\mathrm{Re}}} \tag{2 33}$$

which by the heat transfer analogy $Gr = Re^2$ can be written as ,

$$\delta_v = H\left(\frac{\mathrm{Pr}}{\mathrm{Re}}\right)^{\frac{1}{4}} \tag{2 34}$$

This may be simplified to the result

$$\frac{V_{n\delta_v}}{V_{\delta_v}} = \frac{St\ H}{\delta_T} \tag{2 35}$$

Thus, the consistency of the assumption $V_{n\delta v} < O\,(\,V_{\delta v}\,)$ can be judged once the magnitude of δ_T is estimated. For the estimation of thermal boundary layer thickness we now consider the cases 1 and 2 illustrated previously

2.6.2.2. Scales in the intermediate thermal layer

Case 1

From the situation shown in Fig 2 7 (a) this situation applies to metallic melts and

$$\mathrm{Pr} < O(1) \qquad \delta_v < O(\delta_T) \tag{2 36}$$

For this case, from Fig 2 7 (a) we can assume the following scales for the velocity

$$U_{\delta_T} = U_{\delta_v} = U_g = \sqrt{g\ \beta_l\ \Delta H} \tag{2 37}$$

For convection diffusion balance in the energy equation

$$\frac{U_{\delta_T}\Delta}{H} \sim \frac{\alpha_l\ \Delta}{\delta_T^2} \tag{2 38}$$

$$\Rightarrow \delta_T = \sqrt{\frac{\alpha_l\ H}{U_{\delta_T}}} \tag{2 39}$$

which gives upon some manipulation

$$\delta_T = O(H\,\mathrm{Pr}^{-1/2}\mathrm{Re}^{-1/2}) = O(H\,\mathrm{Pr}^{-1/4}Ra^{-1/4}) \tag{2.40}$$

In this thermal boundary layer of thickness δ_T, then

$$U_{\delta_T} = U_g = \sqrt{g\beta_1\,\Delta H} \tag{2.41}$$

$$V_{\delta_T} = O(\frac{\delta_T}{H}\sqrt{g\beta_1\,\Delta H}) \tag{2.42}$$

$$\Delta_{\delta_T} = \Delta \tag{2.43}$$

Now, we return to the ratio in Eq. (2.31) in order to determine the range of validity of the scales above. Thus,

$$\frac{V_{s\delta_T}}{V_{\delta_T}} = \frac{St}{\mathrm{Pr}^{-1/2}\mathrm{Re}^{-1/2}} = St\,\mathrm{Pr}^{1/4}Ra^{1/4} = St\;Gr^{1/4} \tag{2.44}$$

From this relationship, it is evident that if

$$Gr^{1/4}\;St > O(1) \tag{2.45}$$

i.e.,

$$Gr > O(\frac{1}{St^4}) \tag{2.46}$$

then the interfacial velocity magnitude will become comparable to $V_{\delta T}$ and thus the boundary layer picture will change. Therefore the above scales are valid only under the conditions

$$\mathrm{Pr} < O(1) \quad ; \quad O(1) < Gr < O(\frac{1}{St^4}) \tag{2.47}$$

In most cases of interest the Stefan numbers are small. Thus, there is a range of values of Grashof number under which the above conditions hold. The first inequality is necessary for a boundary layer type situation to exist, while the second inequality places an upper bound on the Grashof number based on the interface velocity, so that a *slow growth* condition can be applied. This latter condition permits the morphological stability theory, so that the scales at the macroscopic level can be obtained. However, for some practical applications, such as rapid solidification processing (Kurz and Trivedi, 1992) this approximation is not valid.

Case 2

As seen in Fig 2 7(b) for this case

$$\mathrm{Pr} > \mathrm{O}(1)\ \delta_v > \mathrm{O}(\delta_T) \tag{2 48}$$

The order of magnitude of velocity in the layer of thickness δ_T , designated $u_{\delta T}$ is given by

$$U_{\delta_T} = \frac{\delta_T}{\delta_v} U_s \tag{2 49}$$

From continuity, again assuming that $V_{\delta T} > V_{n\delta T}$,

$$V_{\delta_T} = \frac{U_s \delta_T}{H} = \frac{\delta_T^2}{\delta_v^2} \frac{U_s}{H} \tag{2 50}$$

For convective diffusive balance in the energy equation,

$$\frac{U_s \Delta_s}{H} \sim \frac{\alpha_l}{\delta_T^2} \Delta_s \tag{2 51}$$

which after simplification implies that

$$\frac{\delta_T}{H} = \mathrm{O}(\mathrm{Pr}^{-1/3}\,\mathrm{Re}^{-1/2}) = \mathrm{O}(Ra^{-1/4}\,\mathrm{Pr}^{-1/2}) \tag{2.52}$$

In this case, from the continuity equation

$$V_{\delta_T} = \frac{\delta_T}{H} U_{\delta_T} \tag{2 53}$$

and again, due to the same arguments as for Eq (2 32) above

$$V_{n\delta_T} = \mathrm{O}(\frac{St}{\delta_T} \alpha_l) \tag{2 54}$$

Therefore the scaling is valid only if $V_{n\,\delta T} < V_{\delta T}$, and this condition is now represented by the ratio

$$\frac{V_{n\delta_T}}{V_{\delta_T}} = St\ \mathrm{Re}^{1/2} = St\ Ra^{1/4}\,\mathrm{Pr}^{-1/4} \tag{2 55}$$

Therefore, the scaling breaks down if

$$Ra^{1/4}\,\mathrm{Pr}^{-1/4}\,St > \mathrm{O}(1) \tag{2.56}$$

$$\Rightarrow \frac{Gr^{1/4}}{\mathrm{Pr}^{1/2}} St > \mathrm{O}(1) \tag{2.57}$$

i e if

$$Gr > \mathrm{O}(\frac{\mathrm{Pr}^2}{St^4}) \tag{2 58}$$

Since in this case $Pr > O(1)$ and $St < O(1)$ for most solidification processes, the

scaling will hold for much larger Grashof numbers than in case 1. Thus, in organic melts where case 2 applies, the scaling presented here is more likely to hold than for metallic melts

2.6.3 Level II. The Morphological Scales

At the morphological level, several different scalings were performed by various authors (Brush and Sekerka, 1989, Langer, 1980). The difficulty in deciding the scales of the microstructural evolution stemmed from the classic difficulty of separating the scales of length and velocity, i e. in determining a selection criterion As mentioned befors several characteristic lengths and times exist for the interfacial features at the microscopic levels. The scales that one adopts therefore depends on the features that one is interested in capturing In the course of our work, it became apparent that an injudicious choice of scales will lead to inordinate amount of computational effort. This was due to conflicting requirements of characteristic physical times and time-stepping criteria imposed by numerical stability considerations For instance, in the diffusion controlled phenomena, a natural choice for the time scale would be a diffusion time scale However, it is well known that for low Stefan numbers, the interface motion is slow enough that the diffusion field relaxes almost instantaneously to transport the latent heat generated at the moving interface. Thus the quasistationary behavior of the field renders the diffusion time scale inappropriate in tracking the evolution of the phase front A better choice would be the time scale of motion of the front Similar considerations apply to the other aspects and variables in interface tracking at the microscopic level. In the following we present two scaling procedures for the micro-scales

Scaling procedure 1

In analyses of morphological instabilities, it is common practice to adopt the instability wavelength from linear stability considerations as the length scale

(Langer, 1980) This scale is given by

$$\lambda_c = \sqrt{d_o \delta_T} \tag{2.59}$$

In diffusion controlled growth it is not possible to explicitly determine the length λ_c This is because the thermal boundary layer thickness $\delta_T = \alpha_l / V_n$ which cannot be estimated theoretically for a general growth configuration The growth velocity can be controlled in practice through the imposed thermal conditions. The instability length remains dependent on the front velocity, a classical problem of selection. The quantity δ_T is therefore estimated to obtain λ_c The velocity scale is chosen to make the non–dimensional interface velocity to be O(1) to facilitate efficient computations and to focus on the important physical mechanisms Here it is important to adopt an appropriate inner temperature scale. The situation is shown in Fig 2.8. It is clear that an appropriate inner temperature scale is

$$\Delta_l = \frac{\Delta \lambda_c}{\delta_T} \tag{2.60}$$

Substituting in the Stefan condition Eq (1.17) gives

$$\rho_l L V_n v_n = \frac{\rho_l \alpha_l C_p \Delta}{\delta_T} \left(\frac{\partial T^*}{\partial n}\right)_{s-l} \vec{n} \tag{2.61}$$

where v_n is the non dimensional normal front velocity, and thus the front velocity

$$V_n = O\left(\frac{\alpha_l}{\delta_T} St\right) \tag{2.62}$$

The time scale has to be chosen carefully A straightforward time scale choice would be the diffusion scale, but this may be inappropriate for observing interfacial processes The time scale of the interface evolution is a slow scale, while that of diffusion is a fast scale For tracking the phase front, the front velocity rather than the diffusional velocity becomes important The ratio of the front velocity to diffusional velocity is

$$\frac{V_n}{\left(\frac{\alpha_l}{\lambda_c}\right)} = \frac{St \ \lambda_c}{\delta_T} \tag{2.63}$$

Therefore for small Stefan numbers the front velocity is much smaller than the diffusional velocities The time scale is chosen for O(1) motion of the interface as

follows The equation for translation of the interface defined by the curve $f(x, y, t)$ is non−dimensionalized to get

$$\frac{\lambda_c}{\tau_l}\frac{d\vec{X}^*}{dt^*} = V_n\ \vec{n}\ v_n = \vec{n}v_{\ n}\ (\frac{a_l\ St}{\delta_T}) \qquad (2\ 64)$$

whereby,

$$\tau_l = \frac{\lambda_c\ \delta_T}{a_l\ St} \qquad (2\ 65)$$

Note that in this case the parameters δ_T and St need to be input from the macroscopic scale. The value of St is of course imposed and δ_T is to be estimated based no the core flow Also, this type of scaling implies a missing piece of information, in that a selection criterion is not employed here Eq (2.59) only indicates a wavelength range expected on the basis of linear stability analysis In Eq (2.59)the value of δ_T is not available as a function of St or material properties In fact, for the pure conduction situation δ_T ie usually taken to be (a_l/V_n), which involves the front velocity in Eq (2 59) In order to separate the scales λ_c and V_n, a selection principle is necessary as pointed out in Chapter 1 Procedure 2 includes the microscopic solvability criterion in the scaling

Scaling procedure 2

Under the assumptions of applicability of the Ivantsov (1947) family of solutions (Isothermal paraboloids and pure conduction transport for temperature field) for small Peclet numbers,

$$Pe = \frac{\lambda_c\ V_n}{2a_l} \qquad (2\ 66)$$

For small Peclet numbers, the Ivantsov relation

$$St = \frac{\Delta}{L/C_p} = \exp(Pe)\ \sqrt{(\pi Pe)}\ erfc(\sqrt{Pe}) \qquad (2\ 67)$$

reduces to

$$St = \sqrt{(\pi Pe)} \qquad (2\ 68)$$

This gives the product of the length and velocity scales. In order to separate the two, accepting the marginal stability/ microscopic solvability selection criterion

mentioned in Chapter I (Kessler et al., 1988) we have another relation in λ_c and V_n of the form

$$\lambda_c^2 V_n = \frac{2\alpha_l \ \bar{d}_o}{\sigma^*} \tag{2 69}$$

where for compactness $\bar{d}_o$ is a capillary length defined as

$$\bar{d}_o = \frac{\gamma \ C_p \ T_m}{L^2} \tag{2 70}$$

and σ^* is a constant appearing in the selection criterion, as explained in Chapter I The above relation of course brings in the key physical ingredients of surface tension and anisotropy which are absent in the Ivantsov model Using Eqs (2 66) and (2 68) above to separate the length and velocity scales we obtain

$$\lambda_c = \frac{\pi \ \bar{d}_o}{\sigma^* \ St^2} \tag{2 71}$$

$$V_n = \frac{2\alpha_l \ St^4 \ \sigma^*}{\pi^2 \ \bar{d}_o} \tag{2 72}$$

The scales above are dependent purely on material properties and the imposed undercooling or Stefan number and the separation has been made possible by the application of selection

There are some important implications of such a choice of scales Now, let us in common practice for a pure conduction situation, the thermal diffusion layer extent be given by

$$\delta_T = \frac{\alpha_l}{V_n} = \frac{\pi^2 \ \bar{d}_o}{2St^4 \ \sigma^*} \tag{2 73}$$

Note that such an estimation of the diffusion layer thickness gives, by substitution in Eq (2 71), a λ_c of the same form as Eq (2 59)

Now consider the equation of front velocity, given by the Stefan condition, with the chosen scales for the dimensional quantities substituted

$$LV_n v_n = \alpha_l \ C_p \ \frac{A}{\delta_T} [\frac{\partial \Theta}{\partial n}]_{s^-l} \tag{2 74}$$

where Θ is the non-dimensional temperature. In the above we have normalized the normal temperature gradients as follows

$$\frac{\partial T}{\partial n} = \frac{(\frac{\lambda_s A}{\delta_T})}{\delta_T}(\frac{\partial \Theta_s}{\partial n^*}) \tag{2 75}$$

where

$$A_i = \frac{\lambda_s A}{\delta_T} \tag{2 76}$$

is an inner temperature scale as seen in Fig 2 8 Upon simplifying Eq (2 74) one sees that

$$v_n = O(\frac{\alpha_l}{\delta_T}\frac{St}{V_n}) \tag{2 77}$$

where the velocity scale is already chosen in Eq (2 72) Using Eq (2 72), one sees that the front velocity is not O(1) as it should be if all the scales are appropriately chosen Thus, one encounters the curious situation that the velocity scale chosen from the selection principle is inconsistent with the seemingly appropriate scales chosen to normalize the Stefan condition in Eq (2 74) It must be emphasized that the velocity scale in Eq (2 72) is obtained from considerations including the Stefan condition. It is a velocity scale that corresponds to the translation of the chosen Ivantsov paraboloids The Stefan condition contains information regarding only the diffusion of latent heat away from the interface and by itself does not provide any information regarding selection, as detailed in Chapter 1 As far as the macroscopic phase front is concerned, it is obviously driven by the temperature gradients in the two phases, which are determined by the diffusion of latent heat and the front velocity itself, a fact that underlies the severe nonlinearity of the solidification problem As pointed out in Chapter 1, there is generally no unique velocity scale that is determined by these considerations. On the other hand, the selected velocity results in the situation shown in Eq (2 77) This puzzling aspect of scaling arising out of the choice of scales based on a selection principle is yet to be resolved satisfactorily in the authors view

2.7 Equations at the Morphological Scales for Pure Conduction

Having decided on the length, velocity and time scales at the morphological level, we are now in the position to identify the scales of the field variables and to cast the equations at this scale in the appropriate non-dimensional form. At the instability scale, considering the fact that $\lambda_c < O(\delta_T)$, the temperature scale of concern, as seen in Fig. 2.8 is

$$\Delta_I = \frac{\lambda_c}{\delta_T}\Delta \tag{2.78}$$

Thus, with these scales, the equations at the morphological scale take the following forms

Heat conduction

$$\frac{\lambda_c}{\delta_T}\frac{Si}{\delta_T}\Theta_t = \nabla^2\Theta \tag{2.79}$$

where $\Theta = (T-T_m)/\Delta_i$ is the non-dimensional temperature. Substituting for λ_c, we get

$$\frac{\pi}{\sigma^*}\frac{\bar{d}_o}{Si}\frac{}{\delta_T}\Theta_t = \nabla^2\Theta \tag{2.80}$$

For δ_T, an estimate may be obtained from the boundary layer considerations detailed above, or a pure conduction estimate may be obtained. The equation for front velocity reads, after substituting for all available scales

$$v_n = \frac{\pi^2}{2Si^3}\frac{\bar{d}_o}{\delta_T}\sigma^*[\frac{\partial\Theta}{\partial n^*}]_{s-l} \tag{2.81}$$

The interface update then takes place according to

$$\frac{d\vec{X}}{dt^*} = [\frac{\partial\Theta}{\partial n^*}]\vec{n} \tag{2.82}$$

which leads to O(1) interface development in unit time.

The Gibbs–Thomson condition is given by

$$\Theta_i = -T_m(\frac{\delta_T}{\pi^2}\frac{\sigma^{*2}}{\Delta}\frac{St^4}{\bar{d}_o})\ \gamma^*(\phi)\kappa^* \tag{2.83}$$

where $\Theta_i = (T_i-T_m)/\Delta_i$ is the interfacial temperature, $d_o = \gamma/L$, and κ^* is the non-dimensional curvature of the interface.

2.8. Morphological Scales and Non-Dimensionalized Equations with Convection

In determining the scaled equations at the microscopic level we assume justifiably that $\lambda_c < O(\delta_v, \delta_T)$. The scales determined in section 2.6.3 are strictly applicable for the diffusion-controlled growth only. However, in the absence of preceding work on pattern selection in the presence of convection, we continue to adopt these scales even in the presence of fluid flow. The estimates based on pure conduction model are expected to hold in the presence of convection at the microscales, since the latter effect is not likely to be strong enough to significantly alter the physics at that scale, at least in the linear stages of growth. In fact, for any Prandtl number the interfacial instabilities are small enough so that the perturbations are embedded within the viscous as well as thermal boundary layer at onset and initial development, i.e. until the perturbations assume sizes comparable to the boundary layer thickness. Thus, the determination of the scale at incipience is more or less governed by diffusion. In what follows the ranges of parameters under which each of the assumptions made will remain valid will be specified.

In order to obtain the remaining scales in the inner (i.e. morphological) region, we return to the two cases presented previously. The general situation is shown in Fig. 2.6(a) above.

2.8.1. Case 1

For this case we have

$$Pr < O(1) \tag{2.84}$$

Let us assume that the following condition holds

$$O(\lambda_c) < O(\delta_v) < O(\delta_T) \tag{2.85}$$

This is usually the case for most growth environments. The scaling presented here is predicated on this condition. The inequality of the left is necessary for the application of morphological stability theories since these rely on pure conduction

transport of heat Thus, in performing the scaling at the morphological level, it is necessary that the convective influences on the instability be weak. The inequality above holds for all but very small undercoolings For very low undercoolings the emerging instability scale λ_c may be quite large (Tirmizi and Gill, 1987) It is not clear if convection modifies the linear stability of an unstable interface and thus the pure conduction scales adopted in the following. Substituting for all the known values from Eqs (2 32), (2.39) and (2 70) and simplifying the inequality results in

$$St^2 > O(\frac{\pi \bar{d}_o \, Re_H^{1/2}}{\sigma^* H}) \tag{2 86}$$

This sets a lower limit on the Stefan number If the Stefan number is very small, i e., the undercooling or front velocity is very small, the length scale of the instability will be large This implies a slower, thicker primary dendrite Thus, as the Stefan number is decreased the length scale of the instability or the dendrite tip radius increases, until in the limit it becomes comparable with a boundary layer thickness However, there is also an upper limit on the Stefan number For the scalings to be valid at all, the Peclet number needs to be very small For small Peclet numbers, the Ivantsov solution reduces to

$$St = \sqrt{\pi Pe} \tag{2 87}$$

Since $Pe < O(1)$ this implies that

$$St < O(\sqrt{\pi}) \tag{2 88}$$

Thus the bounds on the Stefan number for this situation may be expressed as

$$O(\frac{\bar{d}_o \, Re^{1/2}}{\sigma^* H}) < St < O(1) \tag{2 89}$$

The inner scales for the field variable, as seen from Fig. 2 8 are as follows

$$U_i = \frac{\lambda_c \, U_g}{\delta_v} \tag{2 90}$$

$$\Delta_i = \frac{\lambda_c \, \Delta}{\delta_T} \tag{2 91}$$

2.8.2. Case 2

For this case

$$\mathrm{Pr} > O(1) \tag{2.92}$$

From the boundary layer considerations in section 2.2.2, the thickness of the layers are

$$\delta_v = H\mathrm{Re}^{-1/2} \tag{2.93}$$

and

$$\delta_T = H(\mathrm{Pr}^{-1/3}\mathrm{Re}^{-1/2}) \tag{2.94}$$

The scenario pertaining to this case is illustrated in Fig 2.6(b).

Here

$$O(\lambda_c) < \delta_T < O(\delta_v) \tag{2.95}$$

Substituting for the known length scales and simplifying and considering as above the lower bound on Stefan number given by Eq. (2.68) the following condition results

$$O(\frac{\bar{\lambda}_c \mathrm{Re}^{1/2}\mathrm{Pr}^{1/2}}{H\sigma^*}) < St^2 < O(1) \tag{2.96}$$

The field variable scales are

$$U_i = \frac{U\bar{\lambda}_c}{\delta_v} \tag{2.97}$$

and

$$\Delta_i = \frac{\Delta\bar{\lambda}_c}{\delta_T} \tag{2.98}$$

2.9. The Non-Dimensionalized Equations Applicable to the Problem

It is now possible to set up the formulation of the morphological scales based on the scaling relationships developed above. The end result of the scaling procedure detailed above is to be able to express the inner scaled equations in terms of the specified material properties and the imposed outer growth conditions within the limitations mentioned at each stage. Keeping in mind the ranges of validity of all the procedures and scenarios presented, we can now write the non-dimensional forms of the governing equations shown in Table 2.2. These

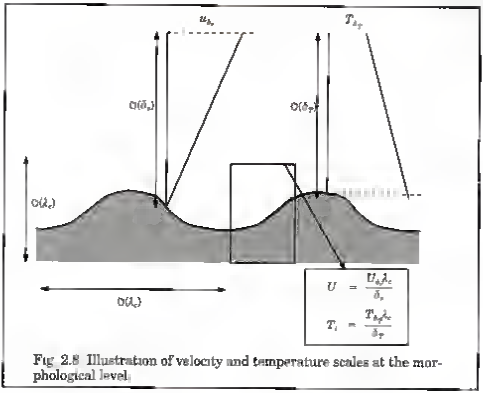

Fig 2.8 Illustration of velocity and temperature scales at the morphological level.

equations have been obtained by substituting all the normalized quantities and the respective scales into the governing equations and simplifying In particular, the Navier-Stokes equations with the Boussinesq approximation (Turner, 1973) have been non dimensionalized and presented in the Table The equations pertaining to interface motion, derived in Chapter I, i e., Eqs (1.12),(1 15) and (1 17) have been non-dimensionalized to obtain Eqs (2 103),(2 104) and (2 105) respectively At this stage the constants C_1, C_2, C_3 and C_4 contain quantities thet have been obtained in the previous sections. Each of these constants can be expressed in terms of material properties or experimental conditions for the specific system analyzed Thus, under a given set of macroscopic flow and heat transfer conditions, it is now possible to investigate the effects of macroscopic conditions on the microstructural properties Apart from the scaled equations (2 99)–(2 106), this

also involves applying boundary conditions on the computational domain for microstructure simulations. These boundary conditions are derived by matching the macro and micro flowfields, taking the scales at each level into account.

2.10. Setting Up a Micro–Model

A procedure for setting up a model at the microscopic level follows the following steps

1. Pick H, the growth chamber dimension
2. Pick Δ, the undercooling. Alternately choose a Stefan number
3. Depending on the material chosen (eg SCN, Pb–Sn) calculate the Prandtl number
4. Based on 1 and 2 evaluate Ra and Re for the outer flowfield
5. Obtain scales in the outer region
6. Depending on Pr, Case 1 or 2 applies. Compute boundary layer scales for the given conditions
7. At the microscale, evaluate λ_c , V_n and τ_i
8. Obtain the inner scales.
9. Confirm that the scalings are valid upto this stage. If not then indicate so and stop
10. Obtain the scaling constants in the non-dimensional form of the inner equation.
11. Obtain the inner region boundary conditions and begin solution procedure

The above procedure has been programmed into a preprocessing module and based on the imposed growth conditions and specified material, can provide the required constants to the flowfield calculations.

Table 2.2. Non–dimensional forms of the governing equations applicable at the microstructural level after scaling.

Continuity

$$\frac{\partial u^*}{\partial x^*} + \frac{\partial v^*}{\partial y^*} = 0 \tag{2.99}$$

u– momentum

$$\frac{\partial u^*}{\partial t^*} + C_1\,(\vec{u}^* \cdot \nabla u^*) = C_2\,(\nabla^2 u^* - \frac{\partial p^*}{\partial x^*}) + C_3\Theta \tag{2.100}$$

v–momentum

$$\frac{\partial v^*}{\partial t^*} + C_1\,(\vec{u}^* \cdot \nabla v^*) = C_2\,(\nabla^2 v^* - \frac{\partial p^*}{\partial y^*}) \tag{2.101}$$

energy

$$\frac{\partial \Theta}{\partial t^*} + C_1(\vec{u}^* \cdot \nabla\Theta) = C_4\nabla^2\Theta \tag{2.102}$$

The Gibbs–Thomson condition

$$\Theta_i = -\,T_m(\frac{\overline{d}_o}{\lambda_c A_i})\gamma^*(\phi)\kappa^* \tag{2.103}$$

Fluid velocity at the interface

$$\vec{u}^* \cdot \vec{n} = (\mathbf{1} - \frac{\varrho_s}{\varrho_l})\frac{2a_0\sigma^* St^4}{u_p\pi^2\overline{d}_o}v_n \tag{2.104}$$

Stefan condition

$$v_n = \frac{\pi^2\overline{d}_0}{2St^3\delta_T\sigma^*}[\frac{k_s}{k_l}(\frac{\partial\theta}{\partial n})_s - (\frac{\partial\theta}{\partial n})_l] \tag{2.105}$$

where

$$C_1 = \frac{U_{ft}}{\lambda_c} \tag{2.106a}$$

$$C_2 = \frac{\nu_{ft}}{\lambda_c^2} \tag{2.106b}$$

$$C_3 = \frac{g\beta_t\Delta\lambda_c x_t}{\varrho_l\delta_T u_t} \tag{2.106c}$$

$$C_4 = \frac{C_2}{\mathrm{Pr}} \tag{2.106d}$$

2.11. Conclusions

In this chapter we have presented the various methods currently available for tracking highly distorted fronts and outlined their advantages and limitations. This knowledge will guide us in designing the main features of the computational technique developed in subsequent chapters. One key aspect of morphological instability is the existence of multiple scales and the different physical phenomena that predominate at each scale. Based on this multi-scale nature of the transport processes and motivated by the need to design a method to analyze the interaction of the different scales, a simplified and specific scaling procedure is performed. From the many assumptions and validity bounds involved in the scale analysis, it is clear that the issue of the interaction between the macro- and micro-scales is very complicated. In the scaling procedure presented above, the instabilities are induced due to supercooling of the melt. In most realistic physical situations, there are impurities present in the melt, and then the diffusion of species becomes the rate-controlling mechanism. When the impurity-driven instabilities are involved, the situation is more complicated. There is a third boundary layer, arising from species diffusion and thus Schmidt number effects enter the picture. Then a scaling analysis has to include this additional effect. Also the scales of the microstructure take on entirely different forms. In addition to these inherent limitations at the microscopic level, the macroscopic flow assumed in the above analysis is much simplified. In reality several competing sources of convection exist and the appropriate scales for the velocity fields are to be decided based on the predominating influences. Thus, the scaling analysis presented here is merely a special case. However, the broad outlines of the procedures are likely to remain valid in typical solidification processes. The scales at each level are to be obtained in each case and are required inputs to the next level. Once the equations at the microlevel are set up, they can be solved for given global conditions. Evaluation of the effects

of the microstructure on macroscopic flow fields is far more involved and will not be addressed in this dissertation Having now obtained appropriate equations at each level, it now remains to come up with a numerical technique that can handle all scales It is to this task that we now turn

CHAPTER 3

A BOUNDARY–FITTED APPROACH TO SIMULATION OF INTERFACIAL INSTABILITIES

3.1. Introduction

As reviewed by Crank(1984) and Floryan and Rasmussen (1989), several methods have been proposed in the literature to track moving fronts each attended by strengths and weaknesses. One commonly used approach involves coordinate transformation to map the irregularly shaped physical domain onto a regular computational domain (Brush and Sekerka, 1989, Thompson and Szekely, 1989, Lacroix, 1989, Shyy, 1994) The numerical methods used in the transformation techniques are well established and straightforward to implement. The coordinate transformation method is thus a good starting point in developing a field solver and interface tracking ideas. With this in view in this chapter, we employ a boundary fitted grid that conforms to the interface and deforms with it The equations are cast in generalized curvilinear coordinates and solved on a transformed domain that is rectangular From this technique, we develop some aspects of the interface tracking scheme to be designed later In the formulation presented here, unlike mapping methods, it is possible to handle multiple–valued interfaces if a suitable grid can be generated Furthermore, the foundation has been developed in terms of computational capability by addressing some specific issues. We also bring to light the limitations of the moving grid formulation in application to the advanced stages of the instability phenomena

In many moving grid formulations the interface motion has been assumed to be slow enough to neglect the terms due to grid motion in the trans-

formed governing equations This approximation leads to a *quasi−stationary formulation* (Lacroix, 1989) We wish to develop an interface tracking procedure that is not restricted to slow moving fronts Therefore we first seek to assess the impact of a quasi-stationary approximation on the accuracy of numerical solutions This is the content of section 3 2 In section 3 3, we reformulate the interface treatment to avoid restriction to non branched and isothermal interfaces The procedure involves straightforward Lagrangian translation of the grid points on the interface The velocity and curve parameters (curvature, normal etc) at each point are obtained in the physical domain The proposed method is demonstrated to yield accurate solutions in terms of temperature field and interface location One can also incorporate with ease interfacial phenomena characteristic of smaller length scales such as curvature effects The computational procedure so developed is then applied to compute the motion of deformed interfaces The method will then be applied to illustrate the competition among the mechanisms affecting stability, such as surface tension and thermal diffusion Finally, in section 3 7, the method is applied to a system involving convection in the melt Here the convection field is not solved for but is imposed as a Couette flow The physical effects of this boundary layer model (Garandet et al , 1990) are consistent with the prediction of the nonlinear stability analyses (Forth and Wheeler, 1989, 1992).

3.2. Assessment of the Quasi-stationary Approximation

3.2.1. Formulation

The boundary-fitted grid is first applied to compute the motion of the phase interface for test cases that can be compared with analytical solutions This will aid in highlighting some aspects of the numerics, particularly accuracy considerations For a pure conduction problem with phase change between liquid and solid, the governing equations for the energy transfer and interface movement are respectively (Crank, 1984), in dimensional form,

$$\frac{\partial T_i}{\partial t} = \alpha_i \left(\frac{\partial^2 T_i}{\partial x^2} + \frac{\partial^2 T_i}{\partial y^2} \right) , \quad i = l, s \tag{3.1}$$

$$\varrho L \frac{\partial x}{\partial t} = - k_l \frac{\partial T_l}{\partial n} + k_s \frac{\partial T_s}{\partial n} \tag{3.2}$$

where T_i is the temperature in the ith phase, α_i the thermal diffusion coefficient, k_i heat conductivity, L the latent heat of fusion, and $x=s(t)$ defines the interfacial position. The partials with respect to n represent derivatives in the direction of the local normal to the interface. Subscripts s and l correspond to solid and liquid respectively.

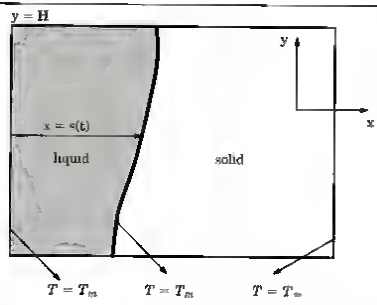

Fig. 3.1 Illustration of the computational domain for comparison with the Neumann solution for a planar phase front

The phase front here is macroscopic and hence usual macroscopic scales are used. The non-dimensional lengths are $X=x/H$, $Y=y/H$, $S=s/H$, H being a representative length scale to be chosen for the specific problem studied. Other non-dimensional quantities are $t^* = \alpha_l t/H^2$, $\varrho^* = \varrho/\varrho_l$ and $\Theta = (T-T_m)/(T_\infty - T_m)$, where T_m and T_∞ are respectively the melting temperature and the imposed

temperature at the appropriate boundary It is convenient to express the interface in the form of the function $x=s(y,t)$ (Lacroix, 1989) Consider heat transport in the liquid phase only. Then, Eqs (3 1) and (3 2), discarding the subscript, become

$$\frac{\partial\Theta}{\partial t^*} = \frac{\partial^2\Theta}{\partial X^2} + \frac{\partial^2\Theta}{\partial Y^2} \tag{3 3}$$

$$-\frac{\partial\Theta}{\partial t^*} = \frac{\varrho^*}{St}\frac{\partial S}{\partial t^*} \tag{3 4}$$

where $St=c_p(T_\infty - T_m)/L$ is the Stefan number

If $X=S(Y,t)$ represents the interface, then Eq (3 4) specialized to an isothermal interface, can be rewritten as

$$[1 + (\frac{\partial S}{\partial Y})^2]\frac{\partial\Theta}{\partial X} = -\frac{\varrho^*}{St}\frac{\partial S}{\partial t^*} \tag{3.5}$$

Following the transformation from Cartesian(X,Y,t) to curvilinear (ξ,η,τ) coordinates (Thompson et al., 1985) such that $X = X(\xi,\eta,\tau)$, $Y = Y(\xi,\eta,\tau)$ and $t^* = \tau$, Eqs (3 3) and (3 4) become

$$\begin{aligned}\Theta_\tau &+ \frac{1}{J}(X_\eta Y_\tau - Y_\eta X_\tau)\Theta_\xi + \frac{1}{J}(Y_\xi X_\tau - X_\xi Y_\tau)\Theta_\eta \\ &= \frac{1}{J}[\frac{1}{J}(q_1\Theta_\xi - q_2\Theta_\eta)]_\xi + \frac{1}{J}[\frac{1}{J}(-q_2\Theta_\xi + q_3\Theta_\eta)]_\eta\end{aligned} \tag{3 6}$$

and

$$\begin{aligned}&\frac{1}{J}[(Y_\eta\Theta)_\xi - (Y_\xi\Theta)_\eta][1 + (\frac{1}{J}[-(X_\eta S)_\xi + (X_\xi S)_\eta])^2] \\ &= -\frac{\varrho}{St}[\frac{\partial S}{\partial\tau} + \frac{1}{J}(X_\eta Y_\tau - Y_\eta X_\tau)S_\xi + \frac{1}{J}(Y_\xi X_\tau - X_\xi Y_\tau)S_\eta]\end{aligned} \tag{3 7}$$

where

$$q_1 = X_\xi^2 + Y_\eta^2 \tag{3 8}$$

$$q_2 = X_\xi X_\eta + Y_\xi Y_\eta \tag{3 9}$$

$$q_3 = X_\xi^2 + Y_\xi^2 \tag{3 10}$$

$$J = X_\xi Y_\eta - X_\eta Y_\xi \tag{3 11}$$

Eqs. (3 6) and (3 7) constitute the complete set of equations in the generalized coordinates for energy transfer and interface movement The quasi-stationary approach adopted by many researchers (Thompson and Szekely, 1989, Lacroix, 1989), simplifies the above equations by dropping all the terms involving coordi

note movement , i.e., X_f Y_f to reduce Eqs (3.6) and (3.7) to the following forms

$$\Theta_\tau = \frac{1}{J}[\frac{1}{J}(q_1\Theta_\xi - q_2\Theta_\eta)]_\xi + \frac{1}{J}[\frac{1}{J}(-q_2\Theta_\xi + q_3\Theta_\eta)]_\eta \qquad (3.12)$$

$$\frac{1}{J}[(Y_\eta\Theta)_\xi - (Y_\xi\Theta)_\eta][\frac{1}{J}(-(X_\eta S)_\xi + (X_\xi S)_\eta)^2] = -\frac{\varrho}{St}\frac{\partial S}{\partial \tau} \qquad (3.13)$$

To test whether such a simplification is acceptable, we design a situation where the interface moves as a planar front. The situation is illustrated in Fig 3.1. In addition, the temperature in the solid is considered uniform. Thus the heat transport is effectively one-dimensional and occurs in the liquid phase only. Boundary and initial conditions are therefore given by (Crank, 1984) ,

$$\Theta = 1, X = 0, \tau \geq 0 \qquad (3.14a)$$

$$\Theta = 0, X \geq S, \tau \geq 0 \qquad (3.14b)$$

$$\Theta(X, \tau = 0.1) = 1 - \frac{erf(\frac{X}{2\sqrt{0.1}})}{erf(\lambda)} \qquad (3.15)$$

$$S(X, \tau = 0.1) = 2\lambda\sqrt{0.1} \qquad (3.16)$$

where λ is the root of the following equation

$$\lambda e^{\lambda^2} erf(\lambda) = \frac{St}{\sqrt{\pi}} \qquad (3.17)$$

The exact solution for Eqs (3.3) and (3.4), with $\varrho^* = 1$, with the boundary and initial conditions given in Eqs. (3.14)–(3.17) is

$$\Theta = 1 - \frac{erf(\frac{X}{2\sqrt{\tau}})}{erf(\lambda)} \qquad (3.18)$$

Two numerical solution procedures are designed in order to compare the solutions obtained from the complete forms of Eqs (3.6) and (3.7) and the simplified forms of Eqs (3.12) and (3.13). These are.

(1) Full treatment. A standard procedure involving backward Euler time stepping along with a second-order central difference spatial discretization scheme is used to solve Eqs (3.6) and (3.7). This full set of equations is solved iteratively in

a coupled manner to continually update the nonlinear coefficients resulting from the coordinate movement and transformation

(2) Quasi-stationary treatment By invoking the quasi-stationary assumption, coordinate movement terms are neglected On account of Eqs (3 12) and (3 13), the equations governing energy transfer and interface movement are decoupled and only a simple explicit procedure is needed to update the interface location.

3.2.2. Results and Discussion

Three values of the Stefan number were chosen to test the performance of the above two numerical approaches The values of Stefan numbers and corresponding λ used are based on Eq (3 17) 11 grid points are used along the x-direction in each case For small *St*, i e, 0 1303, as seen in Fig 3 2(a), both full and quasi-stationary solutions are in close agreement with the exact solution in terms of the interface position as well as the temperature profile, although the full approach is marginally superior However, as expected, with increasing *St* the quality of solutions obtained from the quasi-stationary method is progressively degraded In contrast, good agreement is maintained between the solutions of the full approach and the exact solution Obviously, with a low *St* the interface velocity is modest, and the impact of neglecting grid movement terms on the numerical accuracy is not significant As *St* becomes larger, however, the simplification to the quasi stationary approach is no longer acceptable.

It may be noted that most of the work on such phase change problems is confined to the low Stefan number regime Although the Stefan number encountered in many naturally occurring processes is small, for some problems of current technological significance such as the continuous ingot casting of metal alloys (Shyy et al , 1992), Stefan numbers of order 1 are commonly encountered It is encouraging that the present solution procedure can handle the interface mo-

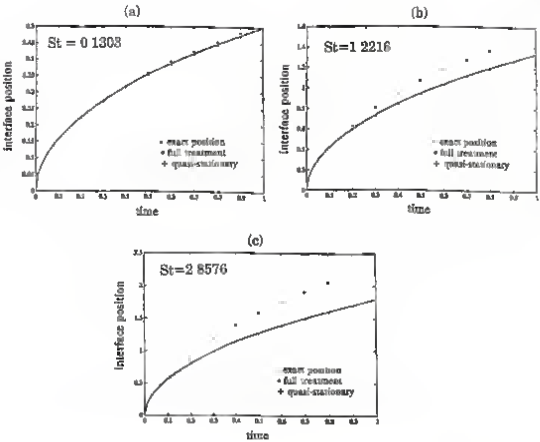

Fig 3 2 Comparison of interface trajectories predicted by the full equations and the quasi-stationary equations with exact solution for three Stefan numbers (a) St = 0 1303 (b) St=1.2218 (c) St=2 8576

tion for higher Stefan numbers over periods where the phase boundary has moved to more than twice the original domain size

3.3. A General Procedure for Interface Tracking

As mentioned in Section 3.2, Eqs (3 6) and (3 7) apply only to an isothermal interface Also, the form of those equations permits calculation of the motion of an interface that can only be expressed in the form $X=S(Y,t^*)$ and thus the in-

terface has to remain single-valued with respect to Y This precludes the possibility of capturing multiple-valued or branched interfaces. As a first step towards overcoming this difficulty, an alternate interface treatment has to be designed Consider the equation for interface advance,

$$-\frac{1}{St}v_n = \left[\frac{\partial\Theta_l}{\partial n^*} - \frac{\partial\Theta_s}{\partial n^*}\right] \tag{3 19}$$

where v_n is the non-dimensional normal velocity of the interface and $(\partial\Theta/\partial n)_{l,s}$ are the normal gradients of temperature in the liquid and solid respectively, and the local normal to the interface is given by,

$$\vec{n} = \frac{1}{|\nabla F|}\left(\frac{\partial F}{\partial X}\vec{I} + \frac{\partial F}{\partial Y}\vec{J}\right) \tag{3 20}$$

where $F=F(X,Y,t^*)$ is the curve defining the interface The interface shape is defined in a piecewise fashion to facilitate handling of branched interfaces Here a quadratic polynomial fit is performed for three successive nodal points at each point of the interface Thus, at the ith point on the interface we designate the curve, $Y_i = a_i X_i^2 + b_i X_i + c_i$, i.e., $F_i = Y_i - (a_i X_i^2 + b_i X_i + c_i)$ defines the interface The a_i , b_i and c_i are determined from the known values of $(X_j, Y_j)_{j=i-1,\ldots,i+1}$ The rationale for choosing a quadratic functional fit is due to the need to obtain the curvatures at the interface accurately Since the curvature involves the second derivative, this is the simplest curve fit that can provide the desired information The local curve definition then yields the derivatives (F_x , F_y and F_{xx}) at each point on the interface Thus the curvature at each point is obtained from,

$$\kappa = \frac{Y_{XX}}{(1 + Y_X^2)^{3/2}} \tag{3 21}$$

We may write Eq (3.2) as,

$$-\frac{1}{St}v_n = \frac{1}{|\nabla F|}(F_X\Theta_X + F_Y\Theta_Y) \tag{3 22}$$

In computing the interface normal velocity then, one seeks to obtain the derivatives F_x , F_y and Θ_x , Θ_y in Eq (3 22)

The derivatives of temperature may be obtained in the transformed coordinates itself, i.e.,

$$\Theta_X = \frac{(\Theta Y_\xi)_\eta - (\Theta Y_\eta)_\xi}{J} \tag{3.23}$$

$$\Theta_Y = \frac{(\Theta X_\eta)_\xi - (\Theta X_\xi)_\eta}{J} \tag{3.24}$$

F_x and F_y of course are directly available in the physical domain from the curve fit. Thus the new coordinates of the interfacial points are obtained from

$$X^{n+1} = X^n + \frac{\partial F}{\partial X}\frac{v_n}{|\nabla F|}\delta t^* \tag{3.25}$$

$$Y^{n+1} = Y^n + \frac{\partial F}{\partial Y}\frac{v_n}{|\nabla F|}\delta t^* \tag{3.26}$$

where δt^* is the time step size. Now that these new coordinates of the curve have been determined, the thermal field is solved for once again, the curve fit is performed at the interface and a fresh interface position is obtained from Eqs (3.25) and (3.26). All these procedures are performed in a fully coupled manner involving interaction among the temperature field, interface motion and grid movement at each iteration. The results for the temperature field in the one-phase, two-phase and perturbed cases compare well with available analytical results as will be demonstrated below.

3.4. Results and Discussion

3.4.1. Case 1. Calculations with Temperature Field Active in One Phase Only.

This alternative interface treatment is compared firstly with the results of section 3.2, where the thermal field is active in the liquid region only. The boundary conditions are given by Eq. (3.14–3.16). From Fig. 3.3 it is evident that for all three Stefan numbers tried, namely, 0.1303, 1.2216 and 2.8576, the accuracy of the present scheme is satisfactory and comparable to those in section 3.2, Fig. 3.2. As can be seen, the computed and exact temperature fields are in excellent

agreement Thus, the current generalized interface tracking procedure does not only cast off the limitations inherent in Eqs (3 12–3 13), but also yields accurate solutions In terms of the numerical results, the differences between interface treatment based on Eq (3 6) and Eq (3 22) are significant. It is simpler to directly use Eq (3 22) in the physical domain, avoiding the undue complexity entailed by the coordinate transformation Moreover the latter method is also more generic, capable of incorporating various interface phenomena and addressing more involved interface shapes

The error introduced in the time stepping is evaluated for St=0 1303 and St=1.2216 The error value used is the normalized difference in the computed and exact interface locations at non-dimensional time τ =1. The error variation for the computed time step sizes depends on the Stefan number, and is higher for the computationally more challenging St=1.2216 A Taylor–series analysis shows that the time stepping for the interface as well as temperature fields are first order accurate in δt However, the global accuracy achieved does not quite reach this order, since in reality the equations for interface motion and temperature field form a spatially and temporally coupled nonlinear system However, the accuracy is closer to first order for the lower Stefan number case since the nonlinearity is weaker

3.4.2. Case 2. Calculations with Temperature Field Active in Both Phases.

The calculation of interface motion is extended to the case where temperature gradients exist in both solid and liquid The configuration is as shown in Fig. 3 4 For the case of a planar interface and the domain in Fig 3 4, the exact solution is given as follows (Crank, 1984)

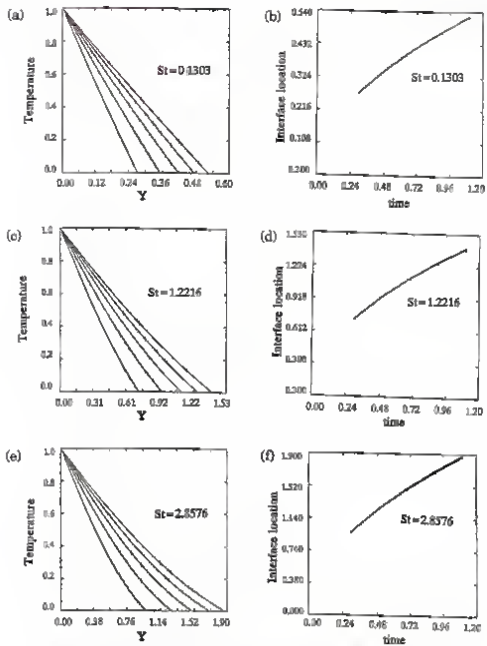

Fig. 3.3. Comparison of computed and exact solutions for St=0.1303, St=1.2216 and St=2.8576. The respective Stefan numbers are shown in the boxes. (a), (c) and (e) Exact and computed temperature fields at different time instants. (b), (d) and (f) Superposed exact and computed interface locations versus time.

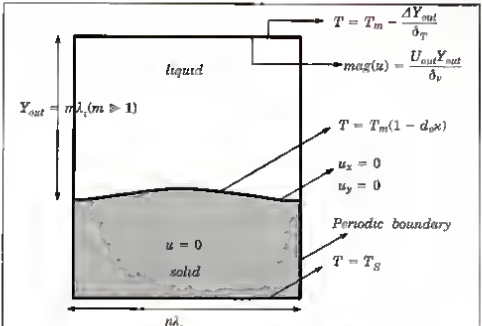

Fig. 3 4 Dimensional form of the boundary conditions on the computational domain.

The temperature fields in the two phases are given by ,

$$\frac{\Theta_{out} - \Theta_l}{\Theta_{out} - \Theta_i} = \frac{erf(\frac{Y_{out} - Y}{2\sqrt{k_l t}})}{erf\lambda} \tag{3 27a}$$

$$\frac{\Theta_s - \Theta_o}{\Theta_i - \Theta_o} = \frac{erfc(\frac{Y_{out} - Y}{2\sqrt{k_s t}})}{erfc(\lambda\frac{\sqrt{k_l}}{k})} \tag{3 27b}$$

Θ_{out} is the temperature at the outer (liquid) boundary $Y = Yout$, Θ_o is the temperature at the solid boundary $Y = 0$, Θ_i is the interfacial temperature and $\Theta_{l,s}(Y,t)$ are the temperature fields in the liquid and solid phases respectively

The interface location is given by,

$$S = Y_{out} - 2\lambda\sqrt{k_l t} \tag{3.28}$$

and λ is a constant obtained from,

$$\frac{e^{-\lambda^2}}{\lambda erf\lambda} - \frac{\Theta_o - \Theta_i}{\Theta_i - \Theta_{out}} \left(\frac{k_s \varrho_s C_{p_s}}{k_l \varrho_l C_{p_l}}\right)^{1/2} \frac{e^{-\lambda^2 k_l/k_s}}{\lambda erfc(\lambda \sqrt{k_l/k_s})}$$

$$= \frac{1}{\sqrt{\pi}\, C_{p_l}(\Theta_i - \Theta_{out})} \tag{3 29}$$

A comparison may be made with an exact solution, with the boundary conditions given as $\Theta = 2$ at the liquid boundary $Y = Y_{out}$, $\Theta = 1$ at the interface, and a time-dependent Θ is imposed at the solid boundary $Y = 0$ from the known value of the exact solution. Also the values of $St = 1$ and $\lambda = 0\ 3778$ are chosen. The ratios k_l/k_s, c_{pl}/c_{ps} and ϱ_l/ϱ_s are taken to be 1. The method of solution is found to yield good accuracy for the case computed. Good agreement was obtained between the computed and exact temperature fields in the two phases, as shown in Fig. 3 5(a), where the interface location corresponds to $\Theta = 1$. As can be seen from Fig. 3 5(b), the superimposed exact and computed interface locations are practically indistinguishable. The log(error) versus log(δt) plot in Fig. 3.5(c) continues to show deviation from the slope expected from the local truncation error analysis, as in the previous case.

3.5 Motion of Curved Fronts

3.5.1. Interfacial Conditions

The interface tracking method developed in section 3.3 is now applied to follow the development of the phase change front for long enough times to obtain substantial curvature of an initially slightly perturbed interface. In tracking the motion of curved fronts, additional physical and computational issues enter. Physically, when the phase interface is deformed surface tension seeks to round out regions of strong curvature. This effect is expressed by the Gibbs-Thomson formula,

$$T_{ieq} = T_{melting}\left(1 - \frac{\gamma \kappa}{L}\right) \tag{3 30}$$

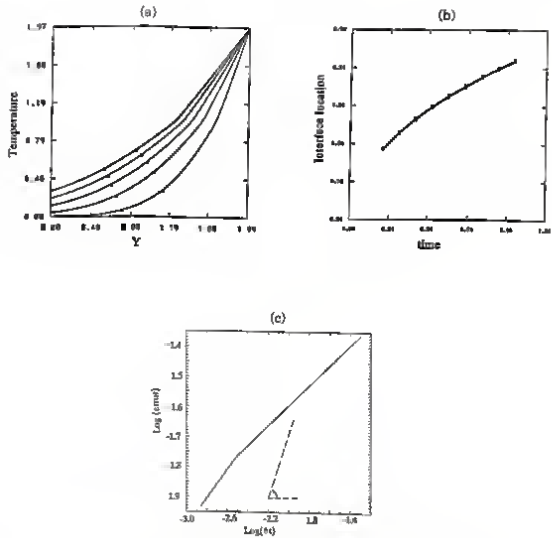

Fig. 3 5 Comparison of exact and computed results for the case where temperature gradients are present in both cases (a) The superposed temperature fields are shown at equal time intervals As can be seen the solutions are practically indistinguishable (b) Computed and exact interface positions with time. (c) Error versus dt plot with stability parameter dt/dx^2 held constant Error was obtained at $t^* = 0.5$ The angle drawn represents a slope of 1

T_m is the melting temperature of a flat interface. $T_{i|eq}$ is the modified temperature after accounting for the Gibbs-Thomson effect, and in this form is applicable to an interface in equilibrium. Here, κ is the local curvature of the front. It is clear that in faithfully simulating the crucial role of surface tension, an accurate computation of curvature is necessary. The curvature of the front and the normal are obtained from Eqs. (3.20) and (3.21). Thus, we demand accuracy in computing the derivatives F_x, F_y, F_{xx} of the curve defining the front.

3.5.2. Scales for the Morphological Instability Simulations

As described in Chapter 2, it is important to choose the proper scales to non-dimensionalize the governing equations. This is done in the interest of computational efficiency and facilitating viewing of the physical phenomena at the proper scales. Thus, at the micro-scale the representative length is taken to be

$$\lambda_c = O(\sqrt{d_o \delta_T}) \tag{3.31}$$

in line with the second scaling procedure outlined in Chapter 2. This instability wavelength lies in the range of microns. Therefore three distinct scales can be defined. The only length scale that is a property of the material is the capillary length d_o ($= \gamma/L$). Let $\varepsilon_1 = \lambda_c/\delta_T$, the ratio of instability wavelength to the diffusion length, $\varepsilon_2 = d_o/\delta_T$, ratio of the capillary length to the diffusion length and $\varepsilon_3 = d_o/\lambda_c$, the ratio of the capillary length to the instability length. Typically, for the small undercoolings encountered, ε_1, ε_2 and ε_3 are all small quantities. Thus, when viewed from the scale of the external diffusion field the interface is planar to first order.

In practice the sole parameter that is externally controlled for solidification from a pure melt is the melt undercooling Δ. The front velocity for a planar front is then a function of Δ and the size of the domain. In tracking the morphological development of the interface the length scale of concern is the instability

wavelength λ_c, which will be adopted as our length scale. Let us define the region at the scale of λ_c as the inner region and that corresponding to δ_T as the outer region (here we shall take $\lambda_c = O((\alpha_s \delta_T)^{1/2})$

As mentioned in Chapter 2, the temperature variations faced by the region adjoining the front are of order $\Delta\lambda_c/\delta_T$ ($<O(\Delta)$) and not Δ. An appropriate choice of scaling parameters has been found to be critical for computational efficiency. Adopting a temperature scale Δ results in extremely slow computational development of the front due to the resulting small values of non dimensional velocities.

Thus, with the scales decided upon above, the equation for velocity of the interface becomes,

$$\varrho L V_n v_n = \frac{\varrho \alpha_l C_{pl} \Delta}{\delta_T} \left(- \frac{\partial \Theta_l}{\partial n^*} + \frac{k_s}{k_l} \frac{\partial \Theta_s}{\partial n^*} \right) \tag{3 32}$$

Here, v_n is the dimensionless velocity, and V_n is the reference velocity scale. For O(1) front velocity, we obtain the velocity scale, $V_n = O(St\ (\alpha_l/\delta_T))$, where St is again the Stefan number.

The equation then becomes, in non dimensional form,

$$v_n = \left(- \frac{\partial \Theta_l}{\partial n^*} + \frac{k_s}{k_l} \frac{\partial \Theta_s}{\partial n^*} \right) \tag{3 33}$$

The form of the governing equation adopted depends on the scaling procedure applied. Hence, although Eq. (3.19) and Eq. (3 33) for the interfacial velocity were obtained from the same dimensional Eq. (3 2), they differ in appearance.

The time scale of motion of the interface is,

$$\tau = \frac{\lambda_c}{V_n} = \frac{\lambda_c \delta_T}{\alpha_s St} \tag{3 34}$$

Hence, the dimensionless form of equation for heat conduction is,

$$\varepsilon_1 St \Theta_\tau = \nabla^2 \Theta \tag{3 35}$$

where $\varepsilon_1 = \lambda_c/\delta_T < O(1)$

Hence, to first order the inner temperature field is governed by the Laplace equation and not the unsteady diffusion equation. The diffusion equation is relevant to the interfacial processes only when $St = O(1/\varepsilon_1)$, i e when the undercooling is large enough in comparison to L/c_p and the size scale of instability becomes comparable to the diffusion length (however, as the undercooling increases, the length scale of instability decreases).

The equations describing the phenomena at the instability scale now correspond exactly to the macroscopic situation pertaining to viscous fingering in Hele-Shew cells. This latter issue has been extensively probed experimentally and analytically (Tabeling et al., 1987, Saffman and Taylor, 1958, Pelce, 1988) and there exists the comforting possibility of drawing on the analogous physics thereof. In fact, the only obvious difference between the Hele-Shew cell and dendritic growth lies in the absence of anisotropy in the former. Such anisotropy has been imposed artificially (Ben-Jacob et al , 1987, Couder et al , 1986) and it turns out that the formerly featureless fingers now develop side-branched structures resembling dendrites.

We may now write the following expression for the non-dimensionalized interfacial temperature which is obtained from Eq (3.30)-

$$\Theta_{i_{eq}} = \Theta_m(1 - \frac{d_0\gamma^*(\varphi)\kappa^*}{\lambda_c}) = \Theta_m(1 - \varepsilon_2\gamma^*(\varphi)\kappa^*) \qquad (3.36)$$

where the superscripts * indicate non-dimensional quantities. The curvature has been non-dimensionalized in terms of $(1/\lambda_c)$.

Fig 3.4 illustrates the physical domain on which we carry out our computations and the boundary conditions applied. In actuality, the boundary conditions at $Y=Y_{out}$ and $Y=0$ are to be obtained from a matching procedure from the external field.

3.5.3. Features of the Computational Method

Eqs (3 33 – 3 36) are solved to follow the motion of a curved interface in the inner region A coupled implicit treatment along with the generalized interface update procedure is used A small perturbation is placed on the interface, and a steady state temperature field is taken as the initial condition Temperature boundary conditions are applied as described above at Y=0, i.e the solid boundary and at $Y = Y_{out}$, the liquid boundary At the sides of the domain we continue to impose an adiabatic boundary condition Due to the assumed symmetry, the interface is constrained to remain normal to the boundaries at $X = 0$ and $X = X_{out}$ Hence, at the boundaries, $F_x = 0$

An adaptively generated grid distributes grid points in the desired regions. This may be accomplished by spacing the points appropriately along the interface as follows (Shyy, 1987)

Let w_i be a weight function corresponding to the ith point along the interface, given by

$$w_i = (1 + \frac{\omega \chi_i^2}{\chi_{max}^2}) \tag{3 37}$$

where χ_{max} is the maximum value of the curvature along the interface, and ω is an adjustable parameter The arc length at any i, ψ_i is obtained from,

$$\psi_i = \psi_{tot} \frac{\int_0^{\xi} \frac{1}{w} d\xi}{\int_0^{\xi} \frac{1}{w} d\xi} \tag{3 38}$$

where ξ is the curvilinear coordinate running along the interface and ψ_{tot} is the total arclength of the front The integration is performed numerically using trapezoidal rule

When $\omega = 0$, the points along the interface are distributed at constant arc lengths. For $\omega > 0$, further clustering is achieved in regions of high curvature. It is emphasized in dendritic growth theory that the tip of the dendrite plays a crucial and sensitive role in determining its structure, in regard to wavelength and velocity selection. Thus it is desirable to place grid points preferentially at the tip by modifying the constant ω suitably. This procedure is adopted in our calculations below where ω is assigned the value 0.5 when $\chi_i > 0$ and 0.1 when $\chi_i < 0$.

3.5.4. Results and Discussion

The development of a perturbed interface, on the scale of the morphology, was tracked first for the case of zero surface tension. The initial perturbation of the interface was applied in the form of a cosine wave given by $Y_i = Y_{mean}(1 - 0.05\cos(2X_i/X_{out}))$. Symmetry was assumed and hence only half of the perturbation was treated. 41 grid points along X-direction, and along Y 101 grid points in the liquid and 41 points in the solid were used in the calculations.

The width of the domain for computation is taken to be 4 (lengths being non-dimensionalized by λ_c), which is the half wavelength of the disturbance. The height Y_{out} is taken to be 50. The interface is originally positioned at $Y_{interface} = 10$. The amplitude of perturbation is small, being 0.0125 times the wavelength. At the liquid boundary, in accordance with the scaling discussed above, a dimensionless temperature of $\Theta = -40$ is applied, while at the solid boundary at $Y=0$, $\Theta = 1$. Thus the perturbation faces an undercooled melt, and the Mullins-Sekerka instability (Langer, 1981) mechanism must operate. The effect of interface attachment kinetics is neglected in the calculations to focus on the interplay of diffusion and capillarity.

The results for the zero surface tension case, in Fig. 3.6, show the rapid development of the instability leading to the splitting of the tip of the protuberance and the formation of a cusp near the boundary. This is consistent with the

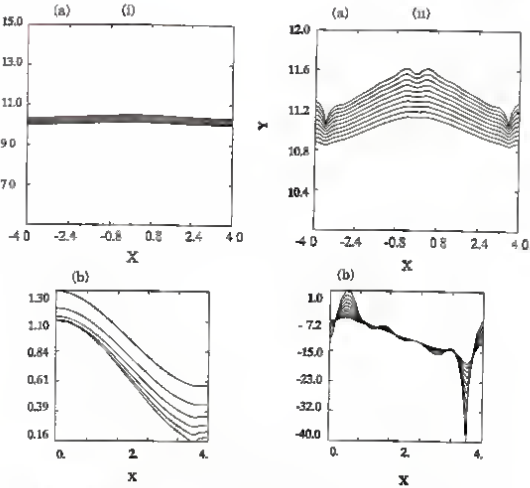

Fig. 3.6 Development of a perturbed interface without surface tension. Only the right half was calculated
(i) Early stages of growth (a) interface shape after reflection of the half computed (b) Velocity of the right half.
(ii) Later stages of growth (a) and (b) as above.

theory of travelling isothermal fronts or isobaric fronts in the case of Saffman-Taylor fingers (Bensimon and Pelce, 1986, Bensimon, 1986, Howison et al , 1985) It is found that in such cases, depending on the initial conditions, the disturbance may bifurcate via tip-splitting or may sharpen into cusps This is due to the fact that in the absence of surface tension, there is no physical mechanism

that provides the short-wave cutoff. The lower limit of resolvable scales is set computationally by the grid spacing. Thus, all scales below the single available length scale, namely δ_T down to the grid spacing are permissible. Moreover, the sharper the perturbation, the faster it is able to give up latent heat due to the point effect of diffusion, and hence the more unstable it is. This tendency to sharpen can either result in a tip splitting cascade or in the formation of a cusp. In fact the appearance of the cusp and the accompanying tip bifurcation ensue quite early in the development of the interface. The initial amplitude to wavelength ratio for the given perturbation shown in Fig. 3.6(ia) is 0.0125. At the final instant shown in Fig. 3.6(ua) the protuberance has grown to just 6 times its initial amplitude. On the left, in Fig. 3.6(ia), is shown the initial shape of the perturbation. The mean position of the interface at the final stages of the development shown is at $Y=11.2$ for the interface originally positioned at $Y=10$. Thus the interface does not progress very far along the Y direction before exhibiting tip-splitting and cusp formation. It is also noticed that even in the initial stages the development of the cusp is indicated as seen from the interface velocity plot, shown for the half wave calculated, in Fig. 3.6(iib). While leading to tip-splitting, from Fig. 3.6(iic), some regions on the interface are travelling faster than their adjacent points. These perturbations will again form distinct protuberances and propagate further until splitting occurs. Again, in the absence of surface tension, there being no lower limit to the length scales allowed, such successive instabilities are physically consistent. Also shown in Figs. 3.6(ic) and 3.6(iic) are the temperature profiles in the solid and liquid regions at the initial and final stages respectively. Obviously, the interface, corresponding to the discontinuity in the temperature gradient, has not progressed significantly before the instability occurs. The occurrence of the cusp, however, leads to difficulty in further computations and the calculations are

terminated at this point We seek to overcome this limitation by extending the current grid generation scheme in future work

The application of surface tension of value $\gamma_{eff} = 0.2$ modifies the interfacial temperature through Eq (3 36) In this case the interface development has been computed, and lies in strong contrast with results in the absence of surface tension For such a low value of surface tension the interfacial temperature assumes values of the order of only $O(10^{-2})$ However, this is sufficient to permit the growth of the perturbation to significant amplitudes as shown in Fig 3 7(iia) without the formation of cusps. Initially, the entire interface moves upward with speeds that are of the same order In fact, there is an initial transient, for the given initial conditions, when the interface velocity actually decreases This is shown in Fig 3 7(iib) However, soon after, the velocity begins to increase again, especially at the tip In the final stages of the evolution shown in Fig 3 7(iia) however, the interfacial velocity, shown in Fig. 3 7(iib) is markedly different in two regions In the region around the tip, the velocity is very much larger than at the sides. This is again due to the differences in temperature gradient between these regions Regions of negative curvature are warmer at the interface due to the Gibbs-Thomson effect This is apparent from the temperature contour plots shown in Fig 3.8, where the isotherms in the liquid are much farther in the region of negative curvature, i.e., at the sides This implies that that region is warmer than the tip, where the isotherms are highly clustered This effect, of the interface slowing down strongly in the regions near the trough has also been observed by DeGregoria and Schwartz (1986) in their simulations of the Saffman-Taylor fingering phenomenon. This illustrates the common features shared by the analogous situations of solidification and viscous fingering. With surface tension, the interface has progressed considerably in contrast to the case without In fact the mean interface position now is at $Y=16$ compared to 11 2 in the previous case The initial

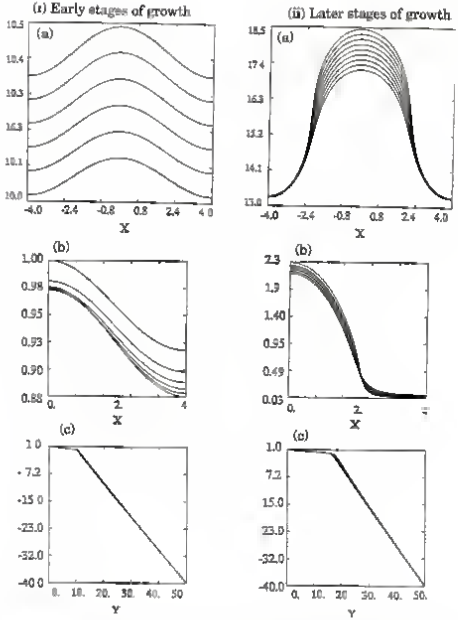

Fig 3 7- Development of perturbed interface with surface tension γ = 0 2 Arrows show sequence of development Only the right half was calculated (i) Early stages of growth (a) interface shape after reflection of the half computed (b) Velocity of the right half (c) Temperature profile at X=2 in the two phases (ii) Later stages of growth (a) ,(b) and (c) as above

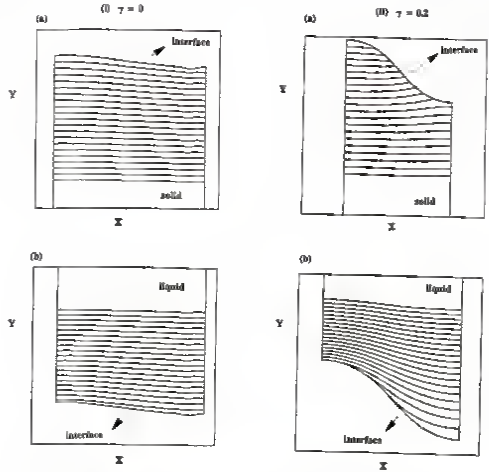

Fig 3 8 Temperature contours in the two phases close to the interface. Contours in the solid are shown only in the range 0 to 0 3. For the case of $\gamma=0$, the interface is an isotherm. For $\gamma=0$ 2 isotherms cross the interface

(i) Case without surface tension (a) Contours in the solid for surface tension $\gamma=0$ (b) Contours in the liquid for $\gamma=0$.
(ii) Case with surface tension. (a) Contours in the solid for $\gamma=0$ 2
(b) Contours in the liquid for $\gamma=0$ 2

amplitude to wavelength ratio of the perturbation is 0 0125 as in the zero surface tension case above. Here, the protuberance has grown to nearly 50 times its original size, in contrast with the previous case This case illustrates the subtle effect that surface tension provides in modifying the stability characteristics of the

phase interface When the perturbation is in the embryonic stage, the surface tension influences the interface temperature only slightly (10^{-2}) Thus it prevents any formation of strong curvatures However, as the protuberance grows, surface tension has an increasing effect on interfacial temperature and begins to influence the overall shape and velocity of the finger It is noted that the growth rate of the perturbation depends on the surface tension since the tip curvature of a bump on the solid is controlled by the capillary length scale In fact, increasing the value of surface tension to 1 for the cases mentioned above leads to the attenuation rather than growth of the initial perturbation

3.5 Preliminary Investigation of Convection Effects

Next, the effect of a modelled fluid flowfield is investigated The flowfield is imposed as a local Couette flow so that the magnitude of the fluid velocity at any section along x follows the Couette profile shown in Fig 3 9 The streamlines are then set parallel to the interface at each section Thus then represents a "deformable" boundary layer situation adopted by Garandet et al. (1990) Thus, due to the velocity field

$$u^2 + v^2 = u_T^2 = v^2 \tag{3 39}$$

and $v/u = \tan \theta(x)$, which determines u and v

Periodic boundary conditions are imposed on the sides of the computational domain for the calculations presented below The equation for energy now reads

$$\frac{\partial H}{\partial t} + C_1(u\frac{\partial H}{\partial x} + v\frac{\partial H}{\partial y}) = C_2\nabla^2 H \tag{3.40}$$

We call C_1 a convection factor In the calculations below, for cases with convection, we use $C_2 =$ 10 and $C_1 = 5$

Fig 3 10 shows a case with $\gamma = 0$, i e no surface tension, for the pure conduction case As seen in Fig 3 10(a) rapid development of the interface with time en

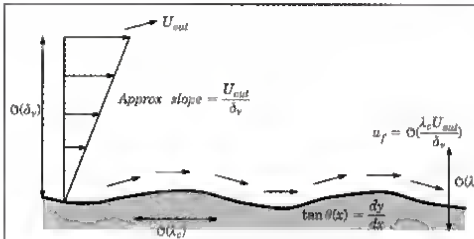

Fig 3 9 Illustration of velocity field assumed and the appropriate scales in the inner and outer regions for the flowfield

sues, leading quickly to the formation of cusps on the interface. The imposition of periodic boundary conditions results in the formation of a finger of shorter wavelength than the dominant finger This is explained as follows The region marked B is one of negative curvature The velocity at this point is slower than the surrounding portions due to the concentration of heat in the concave regions Thus, as seen in Fig 3 10(b), the regions marked C and A travel faster than region B Thus the curvature at B becomes progressively more negative leading precipitously to cusping behavior In the absence of surface tension no smoothing mechanism exists and the cusp deepens, ultimately stalling the calculation It is noticed that in the conductive case perfect symmetry is maintained across the centerline of the perturbation Also, the periodicity of the interfacial calculation is maintained well The Fig 3 10(b) shows that the velocity in the region B is much small-

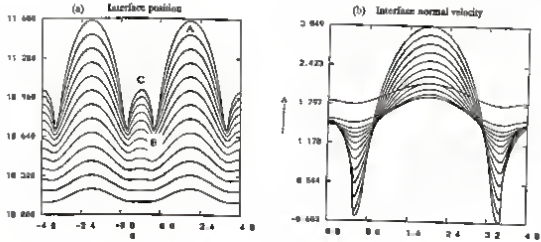

Fig 3 10 Development of interface with time for the pure conduction case with no surface tension (a) Evolution of interface shape with time Features are formation of a small finger in addition to the main propagating one Periodic boundary conditions imposed at the sides are well maintained (b) Normal velocity along the interface shown at different time instants The arrow shows the sequence in time

er than at region A In fact, in the final stages, the region B may actually be remelting, although the accuracy of the calculation in the final stages may be suspect

Fig 3 11(a) shows the development of the interface with time for $\gamma=0$, and for convection parameter $C_I = 5$ The introduction of the flow from left to right introduces a bias in the temperature field This bias is evident from Figs 3 11(b) and 3 11(c) Fig 3 11(b) shows the interfacial shape by subtracting the mean interfacial position from the total interfacial shape The arrows drawn on that figure show that the tip of the perturbation deviates slightly as it propagates Thus, the finger tilts in the direction of the flow as it grows Thus is also evident from Fig 3 11(c) which shows the normal velocity along the interface The point of maximum velocity shifts rightward But the effect of convection does not prevent the eventual development of cusps at the interface Thus surface tension is still a necessity in preventing singularities on the interface

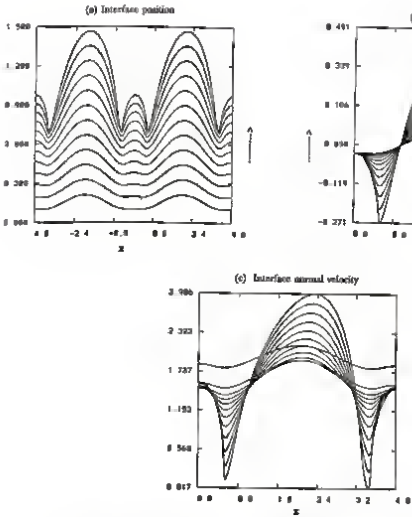

Fig 3.11 Development of interface with time for surface tension γ=0 and convection parameter C_1 =5 (a) Evolution of interface shape with time Features are formation of a small finger in addition to the main propagating one Periodic boundary conditions are well maintained. (b) Interface shape shown after subtracting mean interface position Deviation of the peak in the direction of flow is evident as time progresses. (c) Normal velocity along the interface shown at different time instants Maximum velocity is progressively biased to the right The arrows show the sequence in time

Fig 3 12 represents the case with $\gamma=0\ 2$ and $C_1=0$, i e pure conduction Periodic boundary conditions are again applied at the sides The most striking fact, in comparison to Fig 3 10 is of course the absence of the second finger in this case The action of the surface tension stabilizes the region B shown above and there is no tendency of the regions of negative curvature to lag behind the neighboring regions since the negatively curved parts are now warmer on account of the Gibbs-Thomson effect. This dramatically changes the picture as far as interface evolution goes Fig 3 12 is intended to affirm the robustness of the calculation procedure as far as tracking interfacial properties goes. Shown in Fig 3 12(b) is the shape along the interface at various time steps Good symmetry is maintained about the centerline and periodicity at the ends is perfectly enforced Fig 3 12(c) shows the interfacial normal velocity and indicates the rapidly progressing unstable behavior as the tip of the perturbation travels with increasing velocity in this developing stage of the instability

Fig 3 13 shows the motion of the interface for $\gamma=0\ 2$ and $C_1=5$ The distinguishing feature here is that the perturbation as a whole appears to be translating to the right, i.e. a travelling wave situation results The arrows marked on (a) display this behavior The vertical line is drawn to show this deviation of the peaks of the perturbation Fig 3 13(b) shows the interfacial velocity over one wavelength. The shift of the peak in the velocity is evident Also noticeable from this figure is the periodicity in the interfacial velocity, which is well-maintained, as seen by comparing the left and right boundaries This figure also confirms the travelling wave nature of the instability

In the light of the above observations, it may be noted that although the amplitudes of the perturbations are still not significant and the value of the convection parameter is unrealistic, some results demand attention. The travelling wave nature of the instabilities in the presence of convection has been indicated

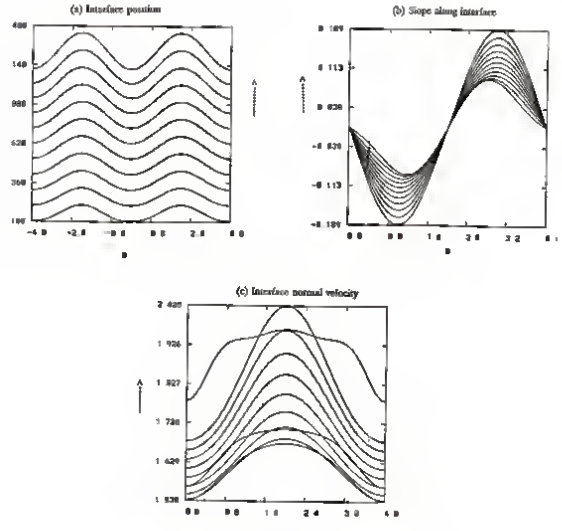

Fig. 3.12 Development of interface with time for a pure conduction case with γ=0.2
(a) Evolution of interface shape with time. The extra finger for γ=0 case is noticeably missing. Periodic boundary conditions imposed at the sides are well maintained. (b) Calculated slopes along the interface. No bias is evident. (c) Normal velocity along the interface shown at different time instants. Symmetry across centerline is observed. the arrow shows the sequence in time.

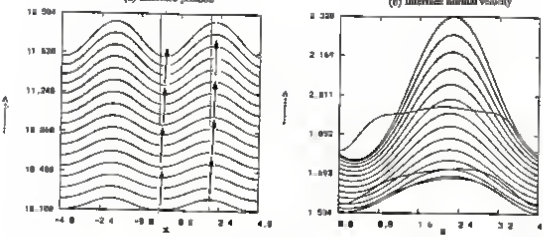

Fig 3 13 Development of interface with time for case with surface tension γ=0·2 and convection parameter C_1 =5 (a) Evolution of interface shape with time Interface remains smooth Periodic boundary conditions imposed at the sides are well maintained Interface as a whole appears to translate to the right (b) Normal velocity along the interface shown at different time instants Maximum velocity is progressively biased to the right The travelling wave nature of front motion is evident The arrow shows the sequence in time.

also by the linear stability analyses for impure materials (Forth and Wheeler, 1989, 1992) The effect of convection on fully-developed dendrites is likely to be interesting The current numerical method will need to be extended by introducing more sophisticated interface tracking techniques to capture the highly non–linear stages of the evolution Furthermore, the velocity field above was merely a model and in fact violates the continuity equation The fluid velocity field will also have to be solved as a further refinement of the computational procedures

3.7. Conclusions

In dealing with deformed boundaries with the structured grid methods, a boundary-fitted, generalized curvilinear formulation is usually employed The simulations presented in this chapter have exposed some of the strengths and

drawbacks of using such a formulation The key issues and conclusions may be summarized as follows

1 The quasi stationary approximation for interface motion is found to be inaccurate in capturing phase boundaries for higher Stefan numbers With the full treatment, the temperature field, interface calculation and grid movement all interact over each iteration and time step Such a computational method results in close agreement with analytical results for an isothermal interface

2 A generalized interface motion technique is developed, which is not limited to a single-valued or isothermal interface Computations show that this method produces results in close agreement with analytical solutions for the one-phase and two-phase cases

3 The spatio-temporal development of deformed interfaces, with the incorporation of the Gibbs Thomson effect due to surface tension, is in line with theory The subtle effect of surface tension in preventing formation of cusps and stabilizing the interface are borne out in the results Tip splitting and cusp formation are observed in the absence of surface tension. Addition of a small amount of surface tension completely changes the picture and a propagating finger is obtained for the duration computed The shape and behavior of the finger are in qualitative agreement with other investigators of the analogous viscous fingering phenomenon. In conjunction with the scaling procedure adopted, significant morphological development has been achieved in a computationally efficient manner The results obtained show clearly the effects of the competing mechanisms on the stability of a perturbed interface

4 Although the interface tracking method developed here can handle a multiple-valued situation there are several caveats attached to a procedure designed on the framework of this purely Lagrangian procedure Firstly, as the interface dilates the markers accumulate in regions where the interface is compressed and

rarify in regions that are stretched Eventually, this undesirable non-uniform distribution of particles can lead to deterioration of the interface information Thus, in order for Lagrangian tracking to be viable the interfacial markers will need to be periodically rearranged along with the grids in the vicinity of the interface Also, it is not clear how the method could be extended in the event of topological change of the interface In spite of these limitations, the method can be useful in elucidating the various aspects of the phase change process as long as the interface is not too deformed

5 The effects of convection have been studied by imposing a Couette-flow type situation, the so-called boundary layer model The results clearly show that surface tension is essential to the propagation of smooth surfaces even in the presence of convection. In agreement with nonlinear stability analyses, the interfacial instability is found to propagate in a travelling waveform, at least for the small perturbations studied in this work.

Due to the limitations imposed by the need for the grid to conform to the moving interface, the boundary-fitted formulation is unattractive as a simulation technique for highly distorted fronts Thus, if a technique can be designed to disconnect grid motion from that of the interface, so that the interface is the only moving component, greater flexibility in dealing with such situations would be achieved We pursue this objective in the next chapter

CHAPTER 4

AN INTERFACE TRACKING METHOD FOR ARBITRARILY SHAPED INTERFACES AND THEIR INTERACTIONS

4.1. Introduction

In this Chapter we develop an interface tracking scheme designed to capture complex shapes and their interactions. Several physical phenomena involve interfaces that on account of instabilities or external impulses, undergo severe deformations, such as dilatation, compression, fragmentation and collision. The physics involved in such processes places severe demands on the interface tracking scheme. For example, as shown in Fig. 1.1 in Chapter 1, the mature instabilities during solidification assume highly deformed geometries. In the events leading to complete solidification, a series of topological changes occur. Due to competition, branches readjust such that by a process of remelting or merger with other sidebranches coarsening or increase in length scales results. Furthermore, the interconnected solid matrix encloses isolated liquid pools which solidify upon cooling. In the case of dendritic branch detachment(Sato et al., 1987), or in equiaxed or globulitic crystal forms (Beckermann et al., 1994, Ni and Beckermann, 1993), convection and settling of isolated crystallites significantly influences the finally achieved grain structure. In some experiments, periodic wavelength readjustment of cellular phase fronts has been induced by changing the growth conditions (de Cheveigne et al., 1990, Cladis et al., 1990, Flesselles et al., 1991). In order to follow the entire spectrum of possible phenomena in the solidification process, it is necessary to be able to deal with a variety of topological

changes The formation of sprays (Lefebvre, 1989), and the shattering of droplets, and other surface instabilities in liquid-gas systems (Fromm, 1981) present challenges in tracking multiple, interacting interfaces In each case, the necessary boundary conditions at the interface are functions of the interface shape and thus the solution in the entire domain critically depends on the accurate determination of the interface shape and its derivatives

In Chapter 3, we followed the evolution of an unstable interface and illustrated the effects of surface tension on interfacial characteristics There, we employed marker particles to define the interface Joining the particles with parabolic segments enabled us to obtain accurate values of the curvature and normals at each point on the interface. A body-fitted grid (Shyy, 1987, Thompson et al , 1985) and generalized curvilinear coordinates were employed to map the irregular phase boundary onto a regular computational domain The boundary condition on the interface was, in this way, applied at the exact interfacial location The extension of the method to highly deformed interfaces requires two major modifications Since the immediate focus of our effort is to be able to resolve interfaces of possibly highly branched nature, our previous strategy of using body-fitted coordinates to conform exactly to the interface will need to be jettisoned. Secondly, the procedure of fitting parabolic curves as interfacial segments is inconvenient when the interface is highly contorted However, the broad outline of the interface tracking procedure is maintained and extended in this chapter The method to be developed herein is designed to track the interface over an underlying fixed Cartesian grid, such that the interface does not correspond to a grid line Thereby, a boundary conforming grid is rendered unnecessary However, the fact that the interface lies within a grid cell will necessitate other measures

in the solution of the field equations, which will be dealt with in subsequent chapters

The conditions engendered by the typical interfacial instability, which we seek to address via our numerical procedure, may be listed as follows:

1) The interface is likely to be highly branched. There also exists the possibility of fragmentation or merger of interfaces. The generation of a body-fitted grid to conform to the interface shape would then be impractical

2) The equations governing the instability phenomena depend critically on such features of the curve defining the interface as the local normal and curvature. These quantities appear in the form of derivatives of the defining curve $F(X,Y,t) = 0$ for the interface. The first and second derivatives F_x, F_y, F_{xx}, F_{yy} need to be obtained very accurately. The calculation of the derivatives is prone to numerical inaccuracy, since these are obtained by the division of small numbers by other small numbers. Their accuracy is nevertheless of utmost importance for a successful numerical calculation

The above primary restrictions influence the choice of numerical scheme for interface tracking. Additionally, a robust numerical procedure is desired, which does not in its implementation further complicate an already formidable problem. We require a simple interface update procedure that is relatively inexpensive. In the marker-based method

(a) The number of data points involved in interface tracking equals the number of marker particles. No additional equations are to be solved for each cell of the domain as in the VOF (Hirt and Nichols, 1981, Liang, 1991) or the level set method (Sethian and Strain, 1992)

(b) There is no ambiguity regarding interface location as in the VOF method. Crisp, smooth interfaces can be obtained and slopes and curvatures calculated accurately

(c) No elaborate logical operations are involved in obtaining an updated interface shape

Hence, we have chosen to develop a grid supported marker-particle scheme to enable us to simulate the dynamics of interface development In what follows, to facilitate the presentation of the methodology developed, the domains defined by the interface are termed solid and liquid, with the particular instability of a solidifying front as a working example The applicability of this tracking procedure is, of course, not limited to any particular physical phenomenon

4.2. Interface tracking procedure

4.2.1 Basic methodology

There are three essential elements to our interfacial tracking procedure, namely cells, interface particles and interfacial curves connecting the marker particles The interfacial particles define the terminal points of the interfacial curves Daly (1967,1969) employed a cubic spline fit to define the interfacial curves However, when the interface became multi-valued with respect to the dependent variable, he switched to a circular arc definition in such regions Thus, decisions were involved on the type of curve fit to be used for a particular segment of the interface The method therein was a standard marker-particle method in that particle depletion/ accumulation was surmounted by adding/deleting particles In Chapter 3, we employed piecewise parabolic approximations to define the interface and obtained an accurate interface tracking facility with the aid of marker redistribution based on equal arclength intervals. However, in using parabolic arcs, for multiple-valuedness such as shown in Fig. 4.1, the representation $Y_i = A_i X_i^2 + B_i X_i + C_i$ would have to be switched to the form $X_i = A_i' Y_i^2 + B_i' Y_i + C_i'$ which will involve keeping track of the turning regions

A simple way around this situation is to use circular arc elements to obtain interfacial segments Thus, one expresses the interfacial curves as, $(X_i - A_i)^2 +$

$(Y_i - B_i)^2 = R_i^2$ where R_i is the radius of the osculating circle at point i and A_i and B_i are the coordinates of the center of the osculating circle. The calculation using circles enables evaluation of normal and curvature in a very simple fashion. The determination of the direction assumed by the normal, which is required to point from the solid into the liquid, is also facilitated and will be discussed shortly. Furthermore, the use of circular arcs is especially attractive when the estimation of local curvature is needed. With circular arcs representing the interface shape, constant curvatures will be maintained between any two consecutive marker points, which is consistent with most of the numerical schemes for the solution of the governing field equations, such as the heat transport equation. The curvature will not change between the neighboring marker points, meaning that the accuracy of the scheme will not be artificially inflated.

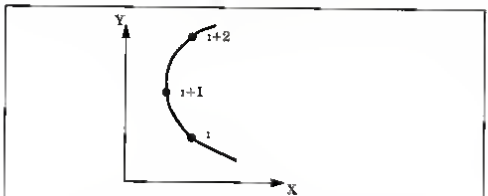

Fig. 4.1. Illustration of turning location on interface.

The disadvantage attached to the circular arc representation is the difficulty in dealing with straight interfaces, since the curve fit will then return an infinite value for R_i. However, if required such straight sections could be approximated using a parabolic arc representation, which does not suffer from this difficulty. Or even more easily, a simple cut-off criterion can be incorporated, whereby a straight line, instead of a circle is assigned for the curve in such regions.

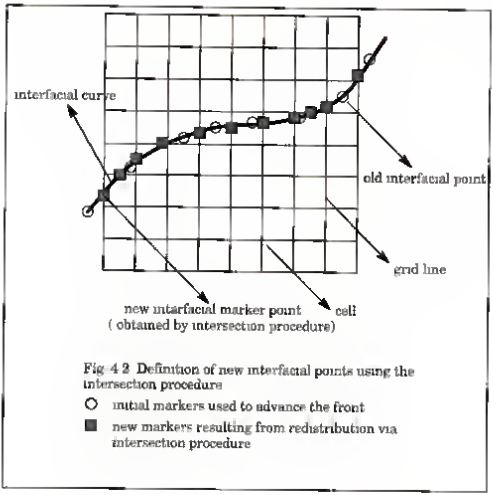

Fig 4 2 Definition of new interfacial points using the intersection procedure

○ initial markers used to advance the front

■ new markers resulting from redistribution via intersection procedure

The use of cells in line with Miyata (1986), offers significant advantages. The procedure employed is illustrated in Fig 4.2 Let the open circles in Fig 4 2 represent an initial distribution of interfacial points or the interfacial point locations obtained after advancing the interface at any given time step. The points are found lying within the cells These interfacial points are connected using circular arcs as follows

For three given points, such as shown in Fig. 4 3, we obtain A_i, B_i R_i by elimination among the relations $F(X_i, Y_i, t) = 0$, $F(X_{i+1}, Y_{i+1}, t) = 0$, and $F(X_{i-1},$

$Y_{i-1}, t) = 0$ The intersection of each segment of the interface with the grid lines is then obtained in a straightforward manner The filled squares on the figure represent the new locations of the interfacial points Thus, at each step, an entirely fresh set of particles is obtained The advantage of such a procedure is that as the interface expands, new intersection points are automatically generated, and the numerical accuracy dictated by the current grid layout is maintained The problem of particle rarefaction/accumulation is thus avoided. New points are automatically generated as the interface invades a particular cell In this regard, the

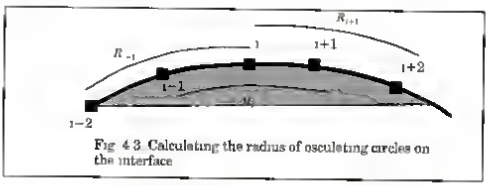

Fig 4 3 Calculating the radius of osculating circles on the interface

shape function used to link the original marker particles is of critical importance in maintaining accuracy during the particle reassignment procedure As will be demonstrated later, the use of constant curvature concept to link the particles proves to be very satisfactory The resolution of the interface tracking scheme is here limited by the grid spacing However, this is not necessarily a limitation Since the interfacial point motion is governed by the gradients of the thermal field, the maximum expected resolution is in effect controlled by the resolution of thermal gradients, i e , the grid spacing Thus the improved resolution obtained by using several interfacial points per cell is merely artificial If further resolution is necessary in any region of the interface, adaptive regridding can be performed to improve both the interface and field variable resolution The other advantage with locating interfacial particles on cell faces is that this facilitates the computation of interfacial velocity and the assignment of boundary condi-

tions and control volumes corresponding to cell control points. This information is necessary anyway and no superfluous operations are introduced by the simple intersection procedure. Once the new interfacial points are determined and they are again connected via interfacial curve segments, directions of the normals can be determined.

Consider the shape of the interface as shown in Fig. 4.4. The osculating circles at different points of the interface are shown. If one were to obtain the normal to the circle at a point, one would compute

$$\vec{n} = \frac{(X_i - A_i)\vec{i} + (Y_i - B_i)\vec{j}}{R_i} \tag{4.1}$$

The directions of the normal to the osculating circles at the sample points are shown along with the required normal direction, which is designated by convention to point from the solid to the liquid. Also, at points such as 1 and 5, the curvatures would erroneously be indicated as being positive (since R_i is always positive), while the expected values are negative, as viewed from the solid. Therefore a decision as to the sign of the normal and curvature is required to be made. This problem is not unique to the circular arc representation. It is in fact more involved to resolve this issue with, say, the parabolic arc representation. The criterion that has been found to work well in determining whether to invert the sign of the normal is outlined here.

(1) Nomenclature : The interfacial points are firstly assigned numbers in sequence such that the solid lies to the right as one advances along the interface, as shown in Fig. 4.5. When renumbering interfaces after mergers etc., this convention is adhered to.

(2) Decision regarding inversion : Four basic types are identified and are displayed in Fig. 4.6 (a) – (d). In cases A and D, the signs of the normal and curvature are inverted. In cases B and C, the signs are retained. This is in line with our inter-

facial point numbering convention, whereby the solid lies always to the right as we traverse the interface. In case A for instance, the center of the osculating circle at the point i lies in the liquid. This is so since $X_i > A_i$. For this case, $Y_{i+1} > Y_{i-1}$. The normal therefore points from the liquid into solid and needs to be reversed.

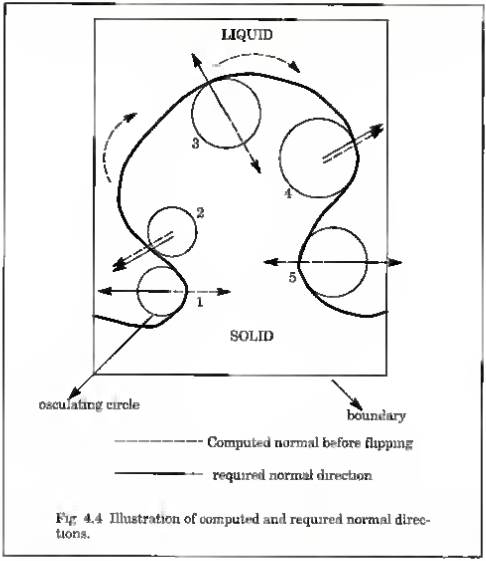

Fig. 4.4 Illustration of computed and required normal directions.

The criterion for case B is $(Y_{i+1} > Y_{i-1}$ $X_i < A_i)$. In such a case, the center of the circle lies in the solid, and no reversal is necessary. Cases C and D may be argued

similarly It is important to adopt these conventions, in order to remove any ambiguity in defining the phases adjoining the interface. These procedures are hereafter followed in all the tracking procedures and have been extremely useful in the simulations presented in subsequent chapters

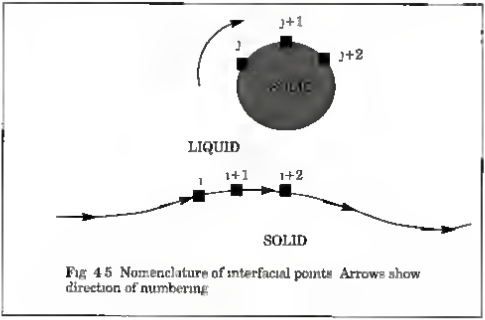

Fig 4 5 Nomenclature of interfacial points Arrows show direction of numbering

4.3. Mergers of interfaces

4.3.1 Procedures for Merger

Another advantage of the use of cells in the interface tracking procedure is related to the treatment of mergers. The treatment of mergers has received little attention in connection with marker-based methods, since it has been thought to involve intense logical manipulation This is indeed the case in the absence of an underlying grid, such as in body-fitted coordinates These difficulties are mitigated considerably when one associates with each point of the interface a cell number as detailed below Let us define the following data arrays

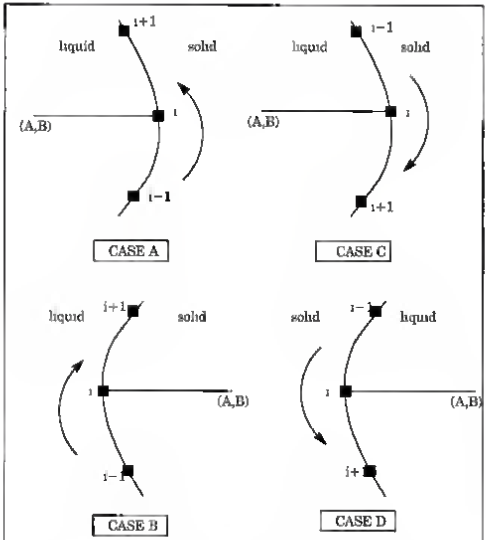

Fig. 4.6 Illustration of conditions for switching of normals

For each interfacial marker particle we record

Interfacial marker particle number i

Index of cell to which the point belongs (x and y index of cell) $cellx(i)$, $celly(i)$

After having found the cell number in which a particular interface point lies, that cell is declared as an interfacial cell. Thus, cells in the bulk are identified by setting $cell\_flag(i,j) = 0$, while cells containing interface segments are flagged $cell\_flag(i,j) = 1$. Conversely, with each cell, the associated point numbers are obtained. This is achieved by sorting through the interfacial cells and finding the identity of the interfacial markers that lie in the cell. Thus,

call number (x, y) $cellx(i)$, $celly(i)$

interfacial point number in that cell $pointnum(cellx(i), celly(i), n)$, where n is the number of markers in that cell

The use of *pointnum*, which contains the integer value indicating the index of the marker particle in that cell, enables us to reduce the number of sorting operations when the interfaces interact. There are three steps in the merger procedure

(1) Detecting merger locations

(2) Setting up for executing mergers

(3) Picking up the new merged interface

Each of these steps will be explained below

Step 1. Detecting mergers .

Equipped with the information outlined above, the merger locations are detected. Consider elements of the interface shown as in Fig. 4.7. In Fig. 4.7, the markers (j+1 to j+4) and (i to i+2) are found in adjacent cells. This information is provided by the cellnumber values $cellx(i)$, $celly(i)$ and $cellx(j)$, $celly(j)$ accompanying these points. Thus, to detect merger, one traverses along the interface, as

in the situation shown in Fig. 4.8, where the marker points along both interfaces are numbered along the clockwise direction.

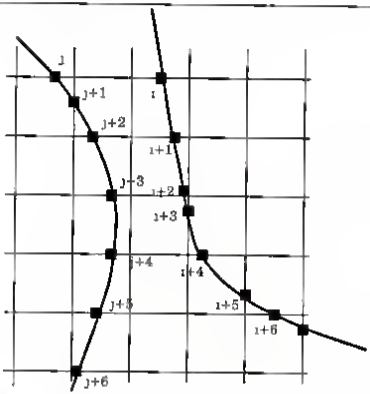

Fig. 4.7 Illustration of interfacial point arrangement during impending merger

Let it transpire that the points (j to j+n1) and (i to i+n2) fall in adjacent cells. This can be done by checking for, say, the point j+3 in Fig. 4.7, the four cells, i.e., top, bottom, right and left side cells. If any of these cells contains a point, then the number of that interfacial point is obtained from the value of *pointnum*. Now, however, in particular reference to point j+3, the point j+4 will lie in the bottom cell. This is merely a neighbor and not a candidate for merger with j+3. In order

to avoid erroneously indicating merger in such a situation, merger is declared only when the following is true

Let the index value of the interfacial point in the current cell be *pointnumber_current* and that in the adjacent cell be *pointnumber_adjacent* *Pointnumber_current* and *pointnumber_adjacent* are obtained from the stored array associating each cell with the corresponding interfacial marker points, namely *pointnum*.

If (an adjacent cell contains an interfacial point) then
  If (abs(*pointnumber_adjacent* − *pointnumber_current)* > say 4) then
    declare merger
  else
    the *pointnumber_adjacent* is just a neighbor No merger
  endif
endif

The latter condition is to prevent adjacent points or very close points from being declared erroneously as merger candidates The value 4 assigned above is chosen since we expect that each cell contains no more than two interfacial markers If merger is detected, we perform the merger operations Thus, in the situation depicted in Fig 4 8, one firstly designates the points j to j+n1 and i to i+n2 as points which have merged Specifically, one incorporates arrays of merger points The merger points occur in pairs, i.e., j connects to i and j+ n1 connects to i+n2 Thus we declare :

mergept1 (1) = j
mergept2 (1) = i
mergept1 (2) = j+n1

mergept2 (2) = i+n2

We also eliminate the points lying between i and i +n2 and j and j+n1 as this is a region that will have merged

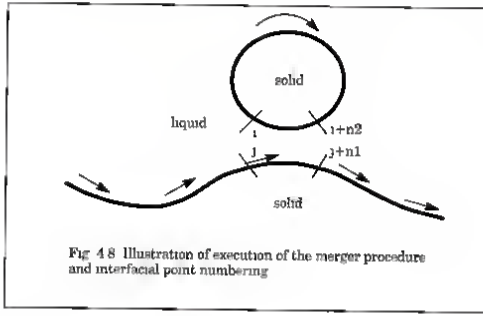

Fig 4 8 Illustration of execution of the merger procedure and interfacial point numbering

Step 2. Setting up to execute merger

In the procedures above however, assigning i,j and i+n2, j+n1 as merger points and joining the pairs accordingly usually leads to very sharp curvatures in that region, since, as can be envisioned by joining j and i in Fig. 4 8, the curvature of the interface changes abruptly over one cell width This occasions numerical difficulties associated with the large curvatures To avoid such complications we smooth the merger event by smearing the merger region slightly This is done as follows -- (i) step back *nstep* points from j, i e., j* = j – *nstep* (ii) step forward *nstep* points from i, i.e , i* = i+ *nstep* (iii) step back *nstep* points from i+n2, i e , i +n2*=i+n2– *nstep* (iv) step forward *nstep* points from j+n1 , j+n1* = j+n1+

nstep The asterisk indicates the merger point after smoothing The choice of forward or backward steps for smoothing can be directly determined by the direction of the sequence of marker points along the interface This smoothing by *nstep* points relaxes the sharp curvature situation that may result after merger The appropriate value of *nstep* depends on the grid spacing employed In our calculations, for a 161X161 uniform grid, *nstep* = 8 has been found to be suitable, and is used in all calculations unless specified otherwise. The merger procedure may now be explained with reference to the situation illustrated in Fig 4 9, where four circles approach each other to merge

Firstly, the nomenclature of interfacial point numbering is to be noted The directions of the arrows on the interfaces shown in Fig 4 9 indicate the direction of point numbering The solid circles expand and merge. The merger points (after smoothing) are i1,i2, .. etc. The pairs are

mergept1 (1) = i1,*mergept2* (1) = j1

mergept1 (2) = i2,*mergept2* (2) =j2

mergept1 (3) = k1,*mergept2* (3) = l1

mergept1 (4) = k2,*mergept2*(4) =l2

and so on Thus, the start of a merger segment is indicated by the odd indexed merger point, while the end of the segment is given by the even indexed merger point Therefore in the above, *mergept1* (1) is the starting point of a merging segment while *mergept1* (2) is the end point of that segment

For each merging circle, we record the start point number and end point number as shown in Fig 4 10 The string *istart* to *iend* forms a segment , i e., one complete object. Thus for the object shown above, corresponding to the index *nseg* for example, the point number of the start point of the string defining the object

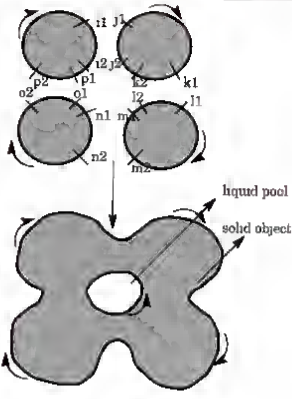

Fig. 4.9 Merger of multiple objects to create more than one closed object

is *istart (nseg)* The end point of the string is *iend (nseg)* Thus each of the four circles has a designated start point and end point value The marker points are numbered by a simple sequence, punctuated by *istart(nseg), iend (nseg)* to give the identity of each interface Let us number the four circles 1 to 4 clockwise. Thus *istart(1)* =1 If each circle is composed of 50 points, *iend(1)* =51, *istart(2)* =52, *iend(2)*=102 etc.

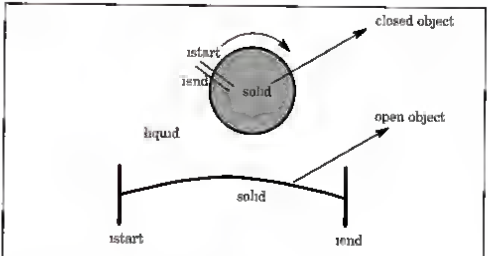

Fig. 4.10 Starting and ending points and nomenclature of open and closed segments

Step 3. Picking up the merged interfaces

Now, after the merger has been declared to occur, one has to form a solid object as shown and one is left also with a liquid pool. The merger procedure has to pick up both these objects. Additionally, since for the interface defining the liquid pool, the solid lies to the right, the nomenclature direction for each object should be as shown in Fig. 4.8. This is so that the pool is identified correctly as being in the liquid phase. To achieve this, we proceed as follows. Let us call the start points (*istart*), the corresponding end points (*iend*) and the merge point pairs (*mergept1*, *mergept2*) *significant* points. Such *significant* points facilitate the merger procedure by reducing the number of points to be searched to ensure merger has been effected at all candidate locations. Thus, instead of sorting through each interfacial point to determine whether all the interfacial points have been taken care of during merger, one merely searches through the *significant* points, which are generally very few in number. Also, the use of *significant* points enables one to perform the connections between merging interfacial seg-

ments as described below

(1) Begin a startpoint loop, i e , until all the startpoints *istart* (1 to 4) have been covered march along the interface collecting points without deleting them from the merger process. All the points along the interface that are encountered are immediately flagged 'done' to indicate that such points have already been covered by the merger procedure. As shown in Fig. 4 10, suppose we start from *istart(1)* =1 We check the point lying in front of the current point along the interface Since the next point has not yet been covered in the merger procedure, i.e it has not been flagged 'done', we pick up that point We proceed in this fashion along the interface, each time checking the point ahead and flagging it as done when we pick up that point Thus, we travel clockwise on circle 1 picking up the as yet untouched points encountered We assign the picked up points to new interfacial point arrays, say *xint_new (icount)* , *yint_new(icount)* where *icount* is a counter that records the number of points collected thus far for the new interface We stop when we hit a *significant* point, which in this case happens to be the merge point i1 Stepping one point ahead of i1 will land us in the merger region In this region, the points have already been eliminated from the interface. The only alternative then is to join this merge point to its pair We thus join i1 to its corresponding merge point pair j1. We now find ourselves on circle 2 We march along that curve in the direction decided upon previously, and as shown by the arrows If the next *significant* point encountered is an end point , which is likely, then we connect the end point to the corresponding start point (a start point for a particular segment is associated with an end point and vice versa) and carry on. If the next *significant* point is a merge point, then we check if the next point along the interface has already been eliminated from the interfacial marker array, i e , if it is part of the merger region If it is, then the only alternative is to connect the merge point

to its pair on the other interface and continue, all the while flagging points covered as 'done' If not, then we continue to march along the same interface The procedure results in the capture of the entire outer curve of the merged solid surface shown in the Fig 4 10 The procedure stops when one encounters a point ahead that has already been covered (i e flagged 'done') , which in this particular case will be *istart(1)* At this point an entire closed curve has been traced Thus, *istart(1)* will form the start point of the new segment, whose new *nseg* value will be 1 The *icount* value resulting after the entire shape has been traced out will be the new end point value *iend(1)* of this segment.

To pick up the remaining parts of the interfaces not covered so far, such as the pool of liquid left out in the middle, one then employs a merge point sweep, i.e., one goes to the first mergepoint that has not yet been covered in the previous procedure. Here this is the point i2 Beginning now from i2 (which again is promptly flagged 'done'), one advances along the interface The next *significant* point encountered is p1 Join to its pair o1 and continue The procedure is carried out as described above and results in the pool of liquid. It is noted that the points are automatically picked up in the appropriate direction in agreement with our nomenclature convention by this procedure. All the necessary information regarding the post-merger interface is also obtained at the end of the merger treatment.

The interface undergoing merger can also be of the open type as illustrated in Fig 4 10 Similar considerations as detailed above apply to such interfaces The situation with the breakup of interfaces is similarly handled. For instance, consider the situation depicted in Fig 4 11

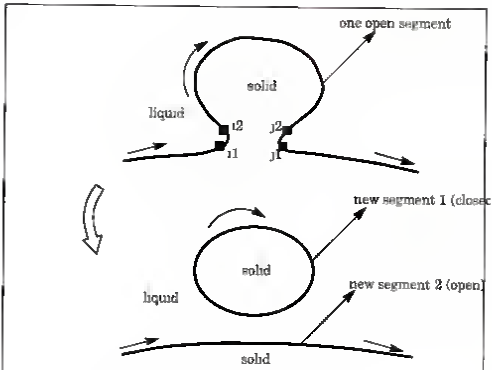

Fig 4 11 Illustration of breakup procedure.

The merge point pairs are (i1,j1) and (i2,j2). Thus, one starts at the start point of the open interval and reaches point i1. Here the points i1 to i2 have already been eliminated as merger regions. So we do not proceed beyond i1, but join it to its pair j1 and carry on. Thus the open segment has now been obtained. We then search for the left over start points. In this case the only available start point, i e , of the original open segment has already been covered. So a mergepoint sweep is performed. The mergepoint i2 is first encountered. One travels from i2 to j2 in the direction of the point sequence on that interface, as shown by the arrow. The region beyond j2 has been eliminated already. So one merely joins j2 to i2 and thus the second segment, of closed type is obtained. Once a complete new segment is

obtained, the type of segment is recorded, namely whether it is open or closed. Currently, we employ and require only one open interval. The segments are arranged in the order of open intervals first, followed by closed solid and liquid pools. The merger detection procedure first takes care of the first, and only, open interface segment and then the start point and merge point searches pick up all the closed objects and left over pools in succession. The strategy then has been to narrow the range of points to be examined to only a few significant points, thus rendering the entire merger procedure very efficient. This also adds to the logical clarity of the entire complex problem. In what follows, we present results pertaining to some cases tried so far in applying the merger procedure.

4.3.2 Summary of Merger Procedure

The merger procedure described above may be summarized as follows. 1. Detect merger locations. 2. Set up data arrays. 3. Collect open interface along with its merged appendages. 4. Perform start point loop for collecting closed interface segments. 5. Perform merge point loop to obtain remaining closed interfaces and pools. 6. Redefine the interface by updating interfacial point string with newly obtained string of points. 7. Perform the curve fit to obtain new normals and curvatures. 8. Translate particles to new positions in cells. 9. Perform intersection procedure to obtain fresh interfacial points. 10. Test for merger. Return to 1.

4.4. Results

4.4.1 Results for Non-Merging Interfaces

The interface tracking method developed herein is first tested for accuracy. The method is capable of handling interfaces of closed and open types. For both types periodic conditions are enforced at the ends of the interface. In Fig. 4.12 we follow the expansion of a circle on a 161x161 grid. The initial radius of the

circle is 1 and the circle expands to a radius of 5 at the end of the calculation. The expansion occurs at a given normal velocity $v_n = 1$. In Fig. 4.12 (a) we show the interfacial shape at equal intervals of time. The time step used $dt = 0.01$, and the circle reaches a radius of 5 in 400 time steps. Fig. 4.12 (b) shows the curvature along the interface at the same time intervals as Fig. 4.12 (a). The interfacial curvatures are found to be constant as expected. Fig. 4.12 (c) shows that the number of points on the interface increases from less than 80 at the start of the calculation to more than 200 at the end. Fig. 4.12 (d) shows the development of radius with time. The superposed crosses are the expected radii according to the imposed linear growth rate. The agreement is excellent, the error being in the vicinity of the machine roundoff.

The case presented in Fig. 4.12 corresponds to constant interfacial curvature which is naturally suited to the present circular arc interfacial representation. As will be demonstrated in the following, other generic cases of variable curvatures can be equally well handled by the present technique as well. However, it is observed that wiggles in the curvature can occur at the locations where the interface is horizontal or vertical. It is also found that in the absence of an intersection procedure, the curvature behaves very well. Thus it appears that these small oscillations are caused by errors in evaluating the new interfacial locations. Such behavior of curvature is also reported in Daly's (1968) work. Some corrective measures have been taken in improving the curvature calculations. These are:

(i) The value of the radius R_i assigned to point i is an equally weighted average of the radius values of the three points used in obtainmg the interfacial curve passing through the point. As shown in the Fig. 4.6, the points involved in calculating R_i are i, $i-1$ and $i+1$. The radius value assigned to point i is given by,

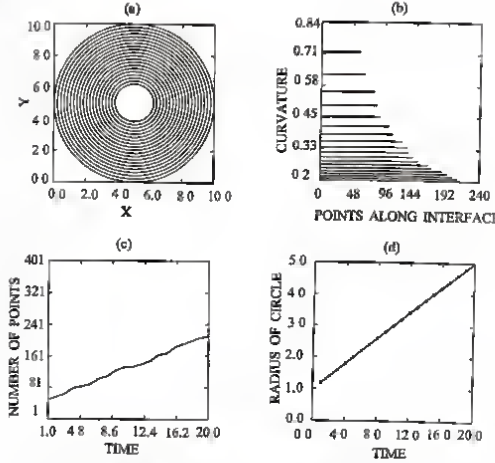

Fig 4 12. Evolution of a circle for imposed uniform radial growth. (a) Shapes of expanding circles at equal intervals of time (b) Curvatures along the interface at the same time instants as in (a) (c) Plot of number of points along interface versus time. Number of points increases as circle expands (d) Superposed computed and expected linear radius variation with time. The crosses correspond to exact values

$R_i^* = (R_i + R_{i-1} + R_{i+1})/3$ Some such smoothing of the curvature value is found to aid in preventing the small wiggles in curvature along the interface. The curvature, being evaluated from the second derivative of the interfacial curve occasions more problems with accuracy than the interface shape and slope which are found to be smooth

(2) It is ascertained that the points on the interface are not too close together It was found that when interfacial points are very closely spaced significant errors and jumps in curvature values can result mainly due to the difficulty in numerically evaluating the derivatives We therefore run through the interfacial points and calculate the arc lengths between two successive points If the arclength corresponding to a particular point is less than a given fraction of the average arclength that point is deleted By experimentation it was determined that points spaced less than 0 7 times the average arclength from its immediate neighbor could be deleted to obtain smoother curvature behavior Generally, very few points actually qualify for such treatment and the number of points defining the interface does not fall significantly

As an example displaying varying interfacial curvature, Fig 4 13 involves growing an open interface Here an initial perturbation of the form

$$Y_i = 2.0 + (1 - \cos(2\pi X_i/10)) \qquad (4.2)$$

is applied and the velocity function for this case is $V_{ni} = Y_t - Y_1$ The velocity function has been modeled to mimic the effect of undercooling in morphological instability The given velocity function causes the interface to bulge out and the final interface shape in Fig 4 13 (a) is seen to be multiple-valued with respect to x and y The number of points in this case as shown in Fig 4 13(b) increases from 161 (= 161X161 Cartesian grid was used) initially to approximately 300 finally, caused by the obvious reason that the overall perimeter of the interface increases with time, resulting in increased number of intersecting points between the interface and grid lines Figs 4 13 (c),(d) show curvatures along the interface at different time instants. The shape of the curvature plot is also seen to change considerably with time The curvature obtained is found to be very smooth without any wiggles even when the interface is highly deformed and the difference in curve

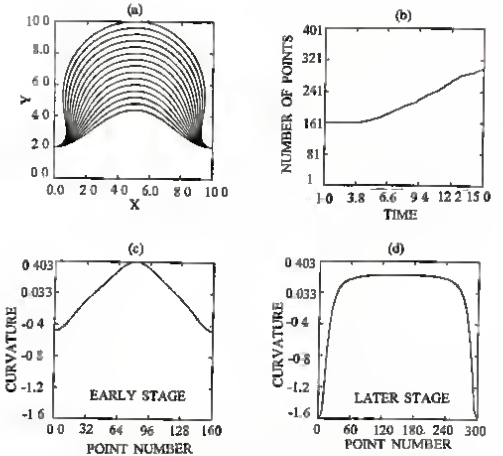

Fig 4 13 Simulation of finger growth using a velocity function (a) Shape of the growing finger at equal intervals of time. (b) The number of points along the interface is shown to increase with time for the growing finger (c) Curvature along the interface early in the development of finger (d) Curvature along the interface in later stage of development

ture between the center and the sides is significant

As a further demonstration, Fig. 4 14 shows the interface shape with a double wave The curvatures are shown in Figs 4 14 (c,d) and are found to be remarkably smooth Fig 4.15 shows the development of an initial interfacial perturbation of the form

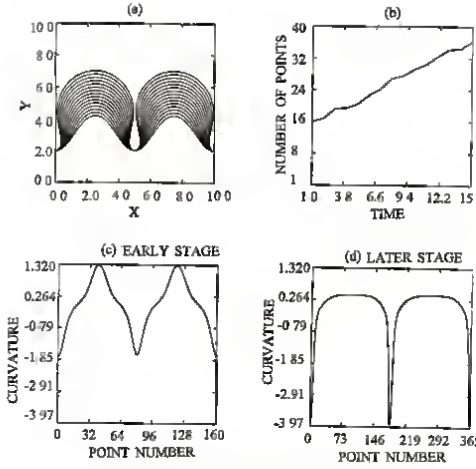

Fig 4 14 Growth of two fingers under an imposed velocity model (a) Shape of two fingers at equal intervals of time. (b) The number of points along the interface is shown to increase with time for the growing finger (c) Curvature along the interface early in the development of fingers. (d) Curvature along interface in later stage of development

$$Y_i = 3.5 + (1 - \cos(2\pi X_i/X_{out}) + \cos(8\pi X_i/X_{out})) \qquad (4.3)$$

The highly contorted final interface shape is well captured The curvatures at various instants are shown in Figs 4.15(b–d) In this case wiggles in the curvature may be detected in the Figs 4 15 (c,d) , although the general distribution is quite good. In this case, the wiggles appear to predominate in the regions where the cur-

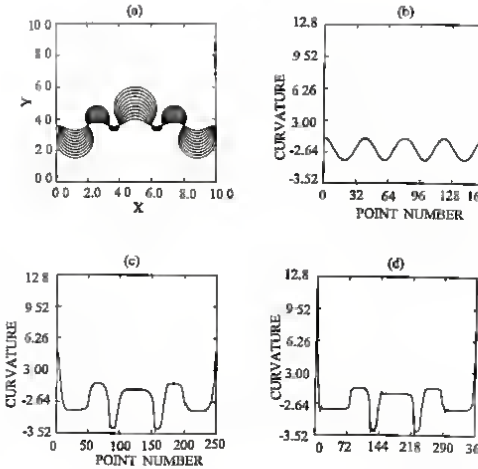

Fig 4 15 A highly convoluted interface evolving under an imposed velocity field (a) Shape of highly deformed interface at equal intervals of time. (b) Curvature along interface in the initial stages of growth (c) Curvature along interface late in the development of fingers (d) Curvature along the interface at the end of the calculation

vature transitions from a positive to a negative value or vice versa This turning of the interface occurs over a very small number of points, possibly over one or two cells only, and hence the interface definition suffers Some further fine-tuning of the intersection procedure and/or a grid refinement procedure is perhaps necessary to smooth out the remaining wiggles.

4.4.2 Results for Merging Interfaces

We first test the merger procedure to determine the effect of grid spacing and the smoothing factor *nstep* in successfully simulating the merger event. Figs. 4.16 (a) – (d) show the merger of two circular regions, the growth velocity being modelled as $v_n = 1$. 81x81 grid points are used in Fig. 4.16 (a), with *nstep*= 1. 81x81 grid points and nstep=5 are used to obtain Fig. 4.16(b). Fig. 4.16(c) and (d) correspond to 161x161 grid and *nstep*=8 and *nstep*=12 respectively. The progressive improvement in the intermediate interface shapes from (a) to (d) is evident, and the final interface shape in Fig. 4.16(d) is quite satisfactory. Employing a finer grid in itself contributes to the improved results in the merger region. Using a generous value of smoothing *nstep* leads to further improvement. However, too large an *nstep* value may lead to dissipation in the region where mergers occur. Adopting *nstep* = 6 in all further calculation, we present test cases to validate our merger/breakup procedure.

Fig. 4.17 shows the interaction of an upward travelling (the normal velocity of all three interfaces is $v_n = 1$) open interface with two expanding circles, whose centers are at (2.5,7) and (8.5,7) in a domain of dimension 10 x 10 units and initial radii are both equal to 1. The procedure first captures the merger of each circle with the open interface. The resulting single open object then grows and there is a further merger which occurs between the circular bulges at around x=4.5 at a later time. Thus, multiple simultaneous mergers and successive mergers are both demonstrated in this example.

In the next example shown in Fig. 4.18, a protuberance is caused to grow, using a velocity function $V_n = (Y_i - Y_I)$. The fingers in the middle grow outward and expand, leading to the situation shown in Fig. 4.18 (b) where merger impends. Fig. 4.16(c) shows the situation immediately upon merger. There is, in the center, a pool of liquid that has been captured as desired. That the normals for the

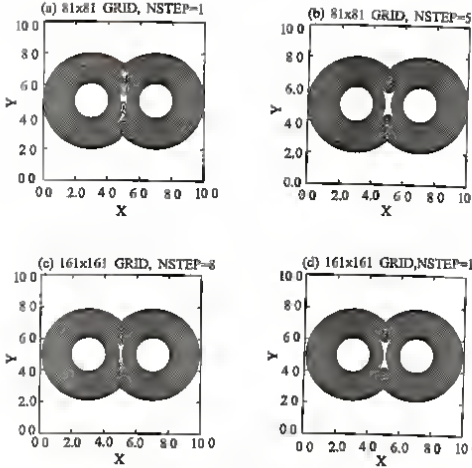

Fig. 4.16 Mergers of circles implemented with different parameters (a) 81x81 grid with smearing, *nstep* value of 1. (b) 81x81 grid with *nstep* =5 (c) 161x161 grid with *nstep* =8 (d) 161x161 grid with *nstep*=12 The result noticeably improves with grid refinement

pool are directed correctly is evident from Figs. 4.18(c–d) where the pool shrinks with time until it disappears as it should. The still growing highly distorted final solid is well captured. Figs. 4.18 (e) and (f) show curvatures along the interface at times corresponding to the shapes shown. The symmetry of the curvatures obtained is highly satisfactory. However, for the pool of liquid, the number of points available (approx. 30) is perhaps not sufficient, for accurate computation of cur-

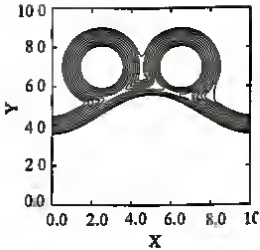

Fig 4 17 Interaction of an upward moving open interface with two circular objects. The circles are centered at (2 5,7 0) and (6 5,7 0) First mergers occur between each of the closed interfaces with the open interface At a later time at x = approx 4 5 a second merger occurs between parts of the same interface. This case shows multiple intersections in space as well as time.

vature. The resolution there may be enhanced by local grid refinement if required.

A further test of the merger procedure lies in assessing its ability to handle breakups In Fig 4 19(a), (b) , two circles expand and coalesce to form one single solid object (161X161 grid, *nstep*=8). At the instant shown in Fig 4 19(b) the merger is reversed, i e , the velocity function now is $v_n = -1$, so that we expect to obtain two circles from the merged shape of Fig 4 19 (b) The breakup process is shown in Figs. 4.19(c–d) and the final separated elements are shown in Fig 4.19 (e) Curvature corresponding to 4.19(d) is shown in Figs. 4 19(f). It is evident that the marger-breakup sequence is not reversible There is significant dissipa-

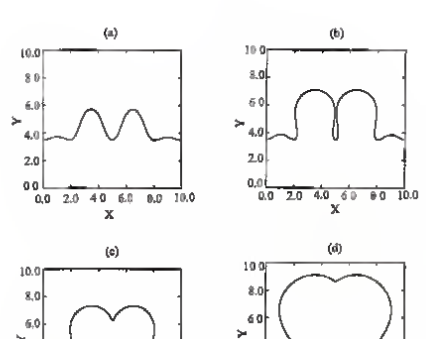

Fig 4.18 The merger of two growing fingers. (a) and (b) The fingers grow and spread under the given velocity model (c) Model has occurred at the center of the domain (d) The finger shape after merger There is a pool of liquid left after the merger The finger expands, while the pool of liquid left after the merger The finger expands, while the pool of liquid shrinks, and finally disappears (e) and (f) Curvatures along the interface corresponding to (a) and (c) The discontinuity in curvature is on account of the liquid blob being formed

tion involved in the simulation and such damping, in the form of the value of *nstep* is essential for handling the rapid change of curvature occurring in the region of mergers. However, with improved resolution the situation may be significantly improved. The above test demonstrates the ability of the merger procedure to handle breakup phenomena.

Another example is shown in Fig. 4.20 where an open interface merges with a growing closed object. The merger is then reversed and the separation of the two objects results. The final shape obtained subsequently, as in Fig. 4.20 (e) is very similar to the initial shapes involved in the merger phenomenon.

4.5. Conclusions

In this chapter, an interface tracking method employing markers with connecting circular arc linkages and cells has been developed. Employing circular arcs offers certain advantages in obtaining such interface features as curvature, slopes, and direction of normals. The interface is tracked on a Cartesian grid. In order to assess the efficacy of the method, several tests were designed. The tests performed employ an imposed velocity field on the interface designed to mimic the physical situation of undercooling. Several of the limitations usually associated with explicit interface tracking schemes have been resolved. The use of cells has facilitated the tracking of an interface that increases in perimeter with time. New points are automatically incorporated on the interface via an intersection procedure, thus circumventing the problems and corrective measures accompanying marker particle depletion/accumulation. It is envisaged that the intersection procedure will aid in solving the field equations also. A strategy has been developed, applying fairly simple one-dimensional data arrays to simulate mergers and breakups of interfaces. This step has removed the most compelling limitation attached to Lagrangian tracking schemes. With the inclusion of the Eulerian

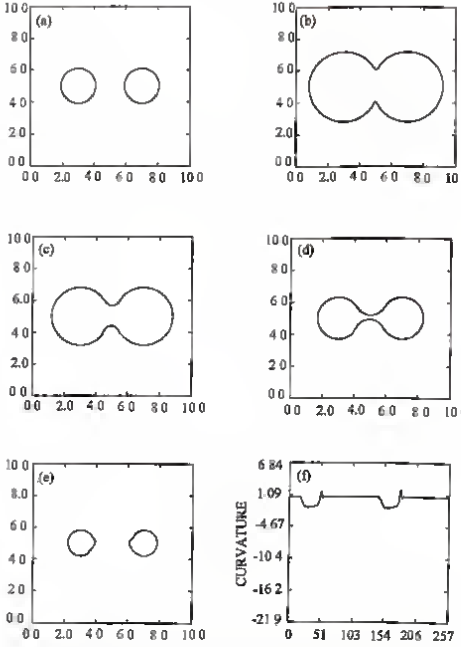

Fig 4.19 Case of merger of two circles and reversed of merger to cause breakup of resulting object. In (a) and (b) the two circles expand and coalesce. At that point, the process is reversed. In (c) and (d) the resulting dumbbell shaped object contracts until it breaks off into two objects in (e). Reversibility is not achieved as seen from the shape and the size of the object seen in (e). (f) Curvature along interface shown in (d)

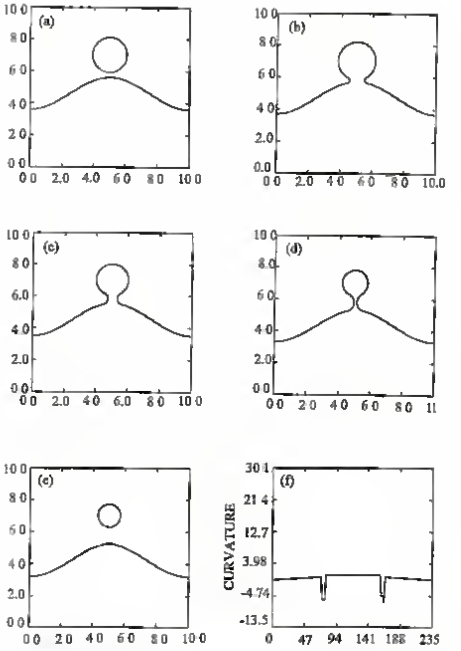

Fig. 4.20. Merger of an open and a closed interface and reversal of merger to induce breakup. (a) The initial shape of the interface. (b) Coalesced form of the composite interface. (c) and (d) the interface shapes as the breakup procedure is in progress. (e) Interfaces after breakup. (f) Curvature along interface shown in (b)

grid feature and some strategies to lighten the logical burden, performing the merger/breakup tasks has been facilitated. The test cases tried thus far have successfully executed the expected merger and breakup tasks. The next step in our simulation efforts involves integrating the new approach to interface tracking with the field equation solver. The field solver needs to operate on a Cartesian grid layout and transfer information regarding front velocity to the interface tracking module. The front velocity will be obtained upon solution of the field equations. In turn, the interface shape and position will serve to impose internal boundary conditions for the field solver. The subsequent chapters attempt to establish this communication.

CHAPTER 5

A METHOD FOR THE SIMULATION OF DIFFUSION–CONTROLLED INTERFACIAL INSTABILITIES

5.1 Requirements of the Numerical Method

Having laid out the physics of some typical morphological instability phenomena and developed the framework for tracking shapes on a Cartesian grid, we now turn to the solution of the field equations, incorporating the interface treatment detailed in Chapter 4. We can characterize the demands on the numerical techniques developed to solve the field equations as follows:

a) The interface grows in perimeter in the course of the instability. Additionally, repeated branching results in a highly convoluted shape. Topological changes may result (Sato et al., 1967). Interfaces may merge or fragment. The solution procedure is therefore required to follow the evolution of an interface under these circumstances. In chapter 4 we developed an interface tracking procedure that can handle all these circumstances. However, there the interface velocity was imposed based on heuristic models to achieve desired distortions of the interface. In this chapter we actually compute the interfacial velocities based on the temperature field governed by pure diffusion.

b) The behavior of the interface is very sensitive to the intricate details of the boundary conditions applied at the interface. In particular, as we demonstrate later, surface tension is a highly delicate mechanism and exerts subtle effects on the finally attained shape. Since the surface tension multiplies the curvature of the interface, the numerical scheme is required to compute the interface shape and

the first and second derivatives of the interfacial curve accurately in order to faith fully represent the physics The boundary condition given by the Gibbs-Thomson condition then needs to be applied in the solution procedure at the exact location of the phase boundary, which is now internal to the computational domain

c) The interface velocity is given by the Stefan condition

$$\rho L v_n = (\ k_s \vec{\nabla} T_s - k_l \vec{\nabla} T_l \ ) \qquad \vec{N} \tag{5.1}$$

Here, ρ, L, v_n and k are respectively density, latent heat, normal velocity of the interface and thermal conductivity, $\vec{N}$ is the normal to the interface and the sub scripts l,s represent liquid and solid phases. This is in fact the statement of conservation of heat for a control volume positioned at the interface. Thus, unless a field equation solver is developed to enforce this condition strictly at the interface, the interfacial velocity will be inaccurately obtained The focus of this work is the interfacial behavior It is therefore imperative that a conservative control volume formulation be designed to treat the fluxes at the interface accurately *Ad hoc* discretizations employing finite difference approximations and interpolations at the phase boundary are to be avoided

5.2 Outline of the Current Approach

Keeping in view the requirements imposed on the numerical method by the physics, we design a solution methodology to track highly distorted fronts The method can be classified as a mixed Eulerian Lagrangian procedure The field equations, in this chapter only the heat conduction equation, are solved on a fixed Cartesian grid The interface is the Lagrangian component and we use a marker–based tracking scheme detailed in Chapter 4 The communication between the interface tracking modules and the field equation solver involves.

a) Information from the interface tracking part on position, orientation and curvature in order to define the control volumes, heat fluxes and cell phases for the field equation solver.

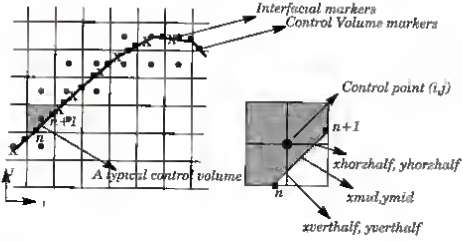

Fig. 5.1 Illustration of arrangement of interfacial and control volume markers and definition of a typical control volume; n and n+1 are indices of the control volume markers.

b) Information from the thermal field, yielding the normal gradients $\partial T/\partial n$ in each phase at each marker particle location. These gradients are used to obtain the velocities at each such point.

Consider the grid layout shown in Fig. 5.1. Two primary tasks are involved in simulating the crystal growth phenomenon:

1. Interface tracking. The interface separating the two phases is tracked in Lagrangian fashion. Conventionally, the drawback with using a particle-defined interface has been that as the interface stretches/compresses the particle distribution becomes uneven and depletion/accumulation can result (Floryan and Rasmussen, 1989). Also, the particle based schemes have been presumed to pose formidable problems when topological changes occur on the interface. In chapter 4 we have shown how these two main shortcomings commonly associated with

surface tracking methods have been overcome. Furthermore, some of the procedures involved in the interface tracking part are useful to the field solver.

2. Solution of the Field Equations. Once the interface location is explicitly specified, it remains to compute the temperature field $T(x,y,t)$. When the interface cuts through a grid as in Fig. 5.1, the control volumes to be considered are no longer regularly shaped. Also, the interface is now an internal boundary. A conservative control volume treatment is designed, so that the boundary conditions are imposed at the *exact* interface location in each control volume. The details are presented in Section 5.4. Thus, there is no ambiguity regarding the location of the interface, and the evaluation of heat fluxes through each face of the irregular polygonal control volume is performed by conventional methods (Wang and Widhapf, 1989). Backward Euler time stepping along with a control volume integration method (Patankar, 1980) is employed, thus alleviating the time-step restriction usually associated with the explicit schemes. In what follows, we demonstrate how diffusion fluxes can be treated in a conservative fashion and arbitrarily shaped, fragmented control volumes can be pieced together in each phase to yield a conservative formulation. Thus, we break with convention in using a fixed Cartesian grid for a surface tracking scheme, instead of a boundary conforming grid. We envisage that the facility of working with a Cartesian grid will aid us in extending our method to incorporate the effects of convection. However, in this chapter we restrict ourselves to a pure conduction situation.

5.3 Formulation

The following equations are solved on the domain displayed in Fig. 5.2. Heat conduction in each phase,

$$\frac{\partial T_i}{\partial t} = \alpha_i \nabla^2 T_i \qquad i = l, s \tag{5.2}$$

and conservation across the interface, yielding an expression for the interfacial

velocity,

$$\rho L v_n = (k_s \nabla T_s - k_l \nabla T_l) \quad \vec{N} \tag{5 3}$$

with the boundary conditions

$T(X,Y_l,t) = T_l$ at the top (liquid side) and $T(X,0,t) = T_s$ at the bottom (solid side), with temperature continuity, $T_l(X_i,Y_i,t) = T_s(X_i,Y_i,t)$ at the interface At the sides of the domain adiabatic conditions are imposed, i e ,

$$\frac{\partial T}{\partial N}(0\ Y,t) = \frac{\partial T}{\partial N}(\Xi,Y,t) = 0 \tag{5 4}$$

where Ξ is the extent of the domain, along x−direction in the Fig 5 2 At the interface, the Gibbs-Thomson condition is applied, in the form,

$$T_l = T_m (1 - \gamma\kappa/L) \tag{5 5}$$

where an isotropic surface tension has been assumed.

It is important, in simulating the morphological instability phenomena, to take account of the length and time scales of the physical mechanisms Linear stability analysis of a planar interface indicates that the critical wavelength for morphological stability is given by (Langer and Muller-Krumbhaar, 1978),

$$\lambda_c = O(\sqrt{(d_o \delta_T)}) \tag{5 6}$$

Here, $d_o = \gamma/L$ is the capillary length scale of the order of Angstroms, δ_T is the thermal diffusion length scale, typically of O(mm) Thus, λ_c = O(microns) The instability events that we are interested in all occur at the scale of λ_c Thus, as described in Chapter 2, the chosen scales are λ_c for the length scale, and $\Delta\lambda_c/\delta_T$ for the temperatures scale, where Δ , the applied undercooling = $T_l - T_m$, T_l being the temperature at the liquid boundary The velocity scale is chosen to be V_n = O($St\ \alpha_l/\delta_T$), where α_l is the thermal diffusivity and the time scale of motion of the interface is $\tau = \lambda_c/V_n = \lambda_c \delta_T/\alpha_l St$

Non−dimensionalizing the equations above with the scales decided upon, and defining a field $\Theta_l = T_l^* - T_m^*$, we obtain the following equations for Θ_l,

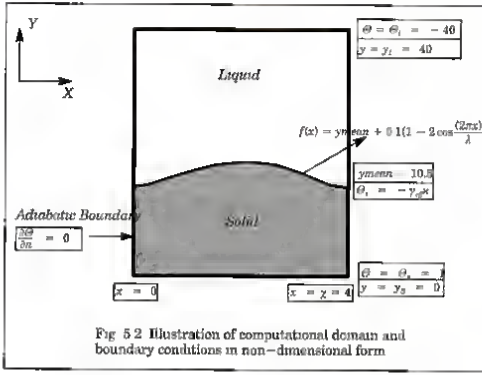

Fig 5.2 Illustration of computational domain and boundary conditions in non−dimensional form

$$\frac{\lambda_c}{\delta_T} St \frac{\partial \Theta_l}{\partial t^*} = \nabla^{*2}\Theta_l \qquad l = l,s \tag{5.7}$$

where $\lambda_c/\delta_T << 1$ and the starred quantities are dimensionless For the small Stefan numbers, i e. undercoolings, usually employed in crystal growth experiments, $\varepsilon_1 = \lambda_c St/\delta_T << 1$ In our calculations we set $\varepsilon_1 = 5x10^{-4}$ The interface motion equation, for the non-dimensional velocity v_n now reads,

$$v_n = (-\frac{\partial\Theta}{\partial n_l} + \frac{k_s}{k_l}\frac{\partial\Theta_s}{\partial n_s}) \tag{5.8}$$

with the boundary conditions, $\Theta(x,y_s,t) = \Theta_s$ and $\Theta(x,y_l,t) = \Theta_l$ at the solid and liquid boundaries, (x,y) are now non-dimensional coordinates and v_n is the dimensionless velocity

The Gibbs-Thomson condition assumes the form, $\Theta_i = -\varepsilon_2\Theta_m\gamma^*\kappa^* = -\gamma_{eff}\kappa^*$, where $\varepsilon_2 = d_o/\lambda_c$ and we designate $\gamma_{eff} = \varepsilon_2\Theta_m\gamma^*$ to be the effective surface tension The adiabatic boundary conditions are,

$$\frac{\partial \Theta}{\partial n} = 0 \quad at \quad x = 0, \quad x = \chi \tag{5.9}$$

where $\chi = S / \lambda_c$ is the non-dimensional domain length in the x-direction

Since Eq (5.7) has the small parameter ε_1 in front of the time derivative, the temperature field is nearly quasi-stationary. Thus, the solution to the Laplace equation is imposed as the initial temperature field in each phase. The interface is perturbed in the form, $f(x,y,0) = ymean + 0.1(1-2\cos(2\pi x/\chi))$. A $ymean$ value of 10.5 was usually specified. The evolution of this initial perturbation was then followed in time.

5.4 The Solution Methodology

Consider the situation depicted in Fig. 5.1, which shows an interface lying arbitrarily on a grid representing part of the computational domain. The interfacial curve, as explained in Chapter 4, is tracked with the aid of marker particles indicated by crosses in the figure. Two primary tasks are to be performed in advancing the interface and thermal field in time.

1. Given the interface position, and the boundary conditions imposed thereon, the temperature field is to be obtained at the next time level.
2. From the gradient of the thermal field calculated, the velocities at the marker positions are computed, the interface is advanced to its new position, and the boundary condition is recomputed.

We now describe the salient features of the procedure for executing these tasks.

5.4.1 Obtaining the thermal field

Given the interface position, the thermal field calculations involve the following procedures:

(a) To classify the control volumes and associate with them the indices of the control volume markers, if any, lying on the faces on the volumes. Only two faces of

the cell are allowed to be cut by the interface

Let us first gather all the pieces of information that knowledge of the interface location provides Consider Fig 5 1 Joining the *interfacial markers* (x's) with straight line segments one identifies the interfacial control volumes and obtains the *control volume markers* (filled squares), from the intersection of these segments with the grid lines The straight line segments are consistent with the second-order accurate control volume formulation, where the field variable is assumed to vary linearly between control points The identified interfacial cells are stored in a one-dimensional array In each cell, the indices of the control volume (CV) markers are stored Considering a typical control volume as in Fig 5 1 and knowing the x and y locations of CV markers indexed n and n+1, other necessary details can be easily extracted to gain complete knowledge of the configuration of the control volume. In particular the intersection of the interfacial segment shown with the vertical and horizontal half cell lines are obtained These are stored in arrays *xverthalf(i,j), yverthalf(i,j),* and *xhorzhalf(i,j),yhorzhalf(i,j)* For cells in which the horizontal or vertical half cell lines are not cut, the initial negative values assigned to these arrays are retained Also, the midpoint of the interfacial segment is identified and designated *xmid(i,j),ymid(i,j)* Thus, each interfacial cell is fully characterized in terms of the manner in which it is cut by the interface

(b) To identify the phase in which a control point belonging to a computational cell (indicated by the circles in Fig 5 1) lies

This is easily done employing the data from (a) One traverses each column of cells starting from j=1, where a flag is initialised to *solid* Upon encountering a cell in which an interfacial segment lies, one determines whether the segment

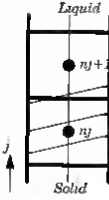

Fig 5 3 Cases in the identification of the phase of control volumes

has crossed the vertical half-line in that cell Three cases are likely as shown in Fig 5 3 In case a, since *yverthalf(i,j)* lies below the control point (i,j), the flag is set to liquid in cell nj and the control point (i,j) is identified as lying in the liquid phase In case b, since *yverthalf(i,j)* lies above the control point (i,j), the flag is set to liquid, while the control point (i,j) is identified as solid This is done so that when the phase of cell nj+1 is being decided upon, the control point in that cell is identified by the flag as liquid In case c, although the interfacial segment does lies in cell *nj*, the vertical half-cell line is not cut by the interface in cell nj Then the flag is retained as solid, and the identification of cell nj+1 as a liquid cell takes place in that cell This procedure of flag resetting is repeated upon encountering an interfacial cell once more in that column

(c) Assemble the control volumes and compute the fluxes to ensure conservation.

Here, a careful rethinking of conventional differencing procedures is called for Consider again the situation shown in Fig 5 1 As a first step the control volume formulation is to be generalized to the polygonal (maximum 5-sided) control volumes that occur at the interface Interfacial features requiring finer grid reso-

lution will be automatically smoothed out, in accordance with the merger procedure developed One applies Green's theorem to the typical control volume shown in Fig. 5 4

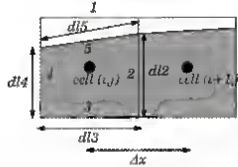

Fig. 5 4 Nomenclature of control volume sides and dimensions.

For the heat conduction equation

$$\varepsilon_1 \frac{\partial \Theta}{\partial t^*} = \nabla^{*2}\Theta \tag{5 10}$$

Integratng over the control volume for the 2– d situation, one has

$$\int_A \varepsilon_1 \frac{\partial \Theta}{\partial t^*} dA = \int_A \nabla^{*2}\Theta dA \tag{5 11}$$

Upon applying Green's theorem, one obtains

$$\int_A \varepsilon_1 \frac{\partial \Theta}{\partial t^*} dA = \oint_l (\nabla^* \Theta \quad \vec{n}) dl \tag{5 12}$$

where the line integral on the right represents the summation of normal fluxes out of the control volume faces Writing the above equation in summation form

$$\varepsilon_{1\,i,j} \frac{\Theta_{i,j}^{\,k+1} - \Theta_{i,j}^{\,k}}{\Delta t} A_{i,j} = \sum_{i=1}^{m} \left(\frac{\partial \Theta}{\partial n}\right)_i^{k+1} dl_i \tag{5 13}$$

The terms $(\frac{\partial\Theta}{\partial n})_i$ here are the normal gradients at each control volume face, dl_i are the lengths of the control volume faces and m denotes the number of control volume sides (4 or 5) and $A_{i,j}$ is the area of the control volume (i,j) The superscript on the right hand side implies that an implicit scheme is to be employed For the control volume shown in Fig 5 4, the fluxes on faces numbered 2, 3 and 4 are easily determined For example, for side 2, we write

$$(\frac{\partial\Theta}{\partial n})_2^{k+1} = \frac{\Theta_{i+1,j}^{k+1} - \Theta_{ij}^{k+1}}{\Delta x} \qquad (5\ 14)$$

where Δx is the grid spacing as shown in the figure Thus the flux through face 2 is obtained from,

$$(\frac{\Theta_{i+1,j}^{k+1} - \Theta_{ij}^{k+1}}{\Delta x}) - dl_2 \qquad (5\ 15)$$

The length of side two is easily determined from the details provided by operations in (a)

The flux through the interfacial segment, side 5, is crucial as far as interfacial behavior is concerned and will be discussed next Before we proceed with the description of the method to evaluate $(\frac{\partial\Theta}{\partial n})_5$, we call attention to the interfacial normal velocity expression, Eq (5.8) The calculation of $(\frac{\partial\Theta}{\partial n})_5$ thus serves two purposes First, it supplies the interfacial heat flux to the temperature field calculation Second, this quantity will be required in computing the interfacial velocity The fact that the same procedure is used for both purposes renders the interface propagation computations consistent with the field solver

Now consider the cell (i,j) shown in Fig 5 4 In order to obtain the normal gradient at the interfacial segment in that cell, $(\frac{\partial\Theta}{\partial n})_5$ we project a probe into each phase in the direction of the normal to the interface at that segment, as shown in

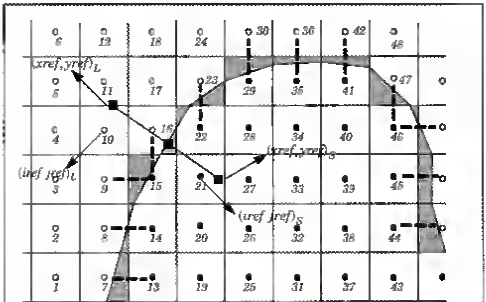

Fig 5 5 Illustration of cut cells definition of partner cells, and method for evaluating normal gradient at the interface (see cell 16) Normal is projected from point (*xmid,ymid*) in cell 16 along the normal at that point The probe of length dp ends at the points (*xref, yref*) in each phase (*xref,yref*) is the index of cell in which (*xref,yref*) lies Solid phase control points are denoted by filled circles, liquid phase by open circles Partner cells are indicated by the linkages between cells

Fig 5 5 Let the normal be given by $\vec{n} = n_x\vec{i} + n_y\vec{j}$ Let the length of the probe be dp This length is chosen so that the endpoint *xref,yref* of the probe lies in an adjacent cell Thus an appropriate value of dp would be the length of the diagonal of the computational cell, which will ensure this condition for all orientations of the interface Thus, $dp = \sqrt{\Delta x^2 + \Delta y^2}$ is assigned. The probe then is given by, $\vec{dp} = dp(n_x\vec{i} + n_y\vec{j})$ If the value of temperature at the end point of the probe, *xref, yref* shown in Fig 5 5 can be obtained, then,

$$(\frac{\partial\Theta}{\partial n})_S = \frac{\Theta(xref,yref,t) - \Theta(xmid,ymid,t)}{dp} \qquad (5\,16)$$

where Θ (*xmid, ymid, t)* is specified, for given surface tension , from the known

value of curvature at the interface there Thus the Gibbs–Thomson condition is incorporated in the calculation The location $xref = xmid(i_q) + dp\ n_x$ and $yref = ymid(i_q) + dp\ n_y$. The cell (iref,jref) in which point (*xref,yref*) lies is easily identified The phase in which (*xref,yref*) lies is known *a priori*, since by convention the normal is specified to point from the solid to liquid The values of normal gradients in each phase are therefore extracted by projecting probes into both phases along the normal direction.

Now, to obtain the value of temperature $\Theta(xref,yref,t)$, a biquadratic shape function is fit to the temperature field in the vicinity of the interface The six coefficients appearing in the biquadratic form, $F(x,y) = ax^2+bxy+cy^2+dx+ey+f$, are obtained by choosing six cells in the *same phase* around the point (*xref,yref*) and inverting the resulting 6x6 matrix by a Gaussian elimination procedure In this process, it is also to be ensured that the six points chosen for fitting the biquadratic should cover three i and three j levels, which is obviously necessary for a biquadratic representation to be valid For example, in the case of the cell 16, the probe, extended from the point (*xmid, ymid*) in that cell, ends in cell 10, in order to obtain the value of temperature at the point (*xref,yref*) which lies in the liquid phase, we need to choose six cells in the liquid phase The choice of five cells is straightforward in this case These are cells numbered 4,16,11,9 and 10 itself The sixth cell remains to be chosen. Depending on which quadrant of the cell 10 the point (*xref,yref*) lies, the cell along the diagonal that is closest is picked In this particular example, that cell is numbered 17 Similarly for the temperature at (*xref,yref*)$_s$, i e, in the solid phase, cells 15,21,27,22,20 and 26 are used Thus, once $\Theta(xref,yref,t)$ is obtained from the functional form, the normal flux is obtained in each phase from Eq (5 16) The $\frac{\partial \Theta}{\partial n}$ value in the *same phase* as the control point

(i,j) is then fed into the control volume expression for that cell Thus, the flux through each face of the control volume shown in Fig 5 4 has now been obtained

To ensure conservation in the vicinity of the interface, however, several other procedures are necessary Consider cells numbered 29 and 30 in Fig 5.5 Between the two control volumes, there is a trapezoidal piece , shown hatched, that is unaccounted for To enforce conservation, it is necessary that the flux across the interface computed for cell 29 as described above be transmitted to cell 30 The procedure involves the identification of three types of cells –

a) Bulk cells A cell that has all its neighbors in the same phase. The control volume formulation for such cells is straightforward

b) Interface adjoining cell. A cell, such as cell 30, that has a neighbor in the opposite phase, but is not itself an interfacial cell.

c) An interfacial cell A cell, such as 29, through which the interface passes.

To enforce conservation, for cells of type b) and c) we need to identify *partner cells* The choice of partner cells has been indicated in Fig 5 5 for each cell by the linkages shown Each interfacial cell is assigned one or more partner cells (for example cells numbered 9,15,16) When the control volume fluxes are assembled for the interfacial cells, the fluxes into the designated partner cells are modified appropriately For example, let cell 29 belong to the solid phase, and cell 30 lie in the liquid While performing the flux calculations for cell 29, we compute the $\frac{\partial \Theta}{\partial n}$ value in each phase at the interface. The flux $\frac{\partial \Theta}{\partial n}$ value in the liquid phase is then transmitted to cell 30 We recall that these fluxes also go into determining the normal velocity of the interface thereby maintaining consistency In addition, the control volume shape and area of the partner cell are redefined, so that the cell 30 for instance, absorbs the hatched trapezoidal region Thus there are no missing pieces in the mosaic of control volumes and all the hatched regions are incorpo-

rated into the appropriate partner cells, along with the fluxes at the interface This assembly process is not difficult to execute. The procedures only apply to the one-dimensional interfacial cell array, and there are only eight separate cases of interfacial cell and partner types as can be deduced from Fig 5 5

The control volume flux assembly procedures have been checked for symmetry by examining the numerical values of the difference coefficients for a specified symmetric interface shape and letting it evolve over time Also, the cell assembly direction was reversed, so that the interfacial cell and its partner exchanged roles, which yielded identical results

(d) Compute the temperature field.

Once the fluxes have been assembled for all the cells in the domain the solution for the temperature field is performed with an iterative procedure, fully coupled with the interface motion The alternate line SOR procedure is employed, leading to a tridiagonal matrix equation which is easily solved. The feature of importance is that over each iteration, the interface is updated along with the temperature field in each phase, and the converged solution yields the thermal field as well as interface position at the new time level

5.4.2 Computing the Velocities of the Interfacial Markers

At this stage, we have already obtained the information necessary for computing the normal velocities of the interface However, the gradients $(\frac{\partial \Theta}{\partial n})_{i,j}$ are now available at the locations *(xmid, ymid)* in each control volume. However, the interfacial markers are not usually located at the points *(xmid, ymid)* Thus, one has to obtain the value of the temperature gradients at the locations of these markers, in order to calculate their velocities To transmit this information to the locations of the interfacial markers, we utilize the array corresponding to the locations *(xmid,ymid)* along the interface The value of the arclength at each point

$(xmid,ymid)$ while traversing the interface is obtained and the $(\frac{\partial\Theta}{\partial n})_{i,s}$ values fit to piecewise quadratic functions of arclength, s e.,

$$(\frac{\partial\Theta}{\partial n})_{i,s} = a_i\psi^2 + b_i\psi + c_i \qquad (5.17)$$

where ψ is the arclength along the interface in the ith interface segment Thus, knowing the value of ψ corresponding to the interfacial marker locations one can identify the segment in which the point lies and thus the value of $(\frac{\partial\Theta}{\partial n})_{i,s}$ can be calculated from the appropriate functional form. The interfacial marker is then translated along the normal $\vec{n}$ such that

$$x^{n+1} = x^n + \Delta t v_n n_x \quad y^{n+1} = y^n + \Delta t v_n n_y \qquad (5.18)$$

This specifies the new location of the interfacial marker at convergence

5.5. Results and Discussion

5.5.1 Grid addition/deletion

The computational domain is configured as shown in Fig 5 6. The domain is partitioned into three regions Coarse grids are employed in the regions I and III, away from the interface, while fine grids are employed in the region II close to the interface However, as the interface rapidly grows out of region II there is a need for introducing a fine grid that precedes the interface in order to be able to calculate the gradients ahead of it with desired accuracy To achieve this, grid lines are added such that a sufficiently extended region ahead of the interface is replenished with fine grids throughout the evolution of the interface. The values of field variables in this region are obtained by linear interpolation. The grid addition takes place at a frequency depending on the extent of the domain traversed by the interface

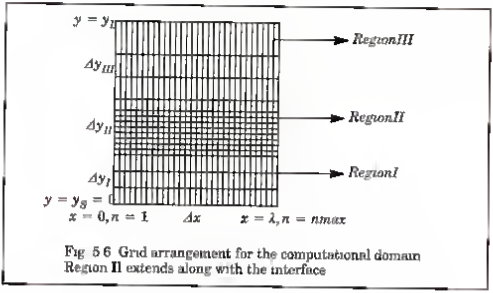

Fig 5 6 Grid arrangement for the computational domain Region II extends along with the interface

5.5.2 Planar interface propagation

We first test the solution scheme for accuracy by employing known exact solutions for a planar interface The Neumann solution for an interface that is melting is given by (Crank, 1984)

$$\Theta(x,y,t) = 1 - erf(\frac{y - y_I}{2\sqrt{t}}) \;/\; erf\xi \qquad (5\ 19)$$

$$S(t) \;=\; y_I \;-\; 2\xi\sqrt{t} \qquad (5\ 20)$$

where $\Theta(x,y,t)$ is the temperature, $S(t)$ is the interfacial position, and ξ is given by the relation,

$$\xi e^{\xi^2} erf\xi \;=\; \frac{St}{\sqrt{\pi}} \qquad (5.21)$$

St is the Stefan number given by $C_p(T_l - T_m)/L$ The boundary conditions are, $\Theta(x,y_l,t) = 1$, i e at the liquid side and $\Theta(x,y,t) = 0$, $y \leq S(t)$, $t \geq 0$, i e. the solid is at uniform temperature. The initial conditions are specified at time $t_o > 0$, taking account of the singularity at $t=0$ (Yao and Prusa, 1989). Thus,

$$\Theta(x,y,t_n) \;=\; 1 - erf\left(\frac{y - y_i}{2\sqrt{t_n}}\right) \;/\; erf\xi \qquad (5.22)$$

and the initial interface location is given by the expression,

$$S(t_n) \;=\; 2\lambda\sqrt{(t_n)} \qquad (5.23)$$

Fig 5.7 compares the exact and numerical solutions obtained for Stefan number St= 0.1303, ξ=0.25. The calculations were performed with 41 grids along x, and 41 grids along y direction. The value of Y_l was taken to be 4. The initial position of the interface was at *Ymean*=3.61. The computation was performed for 1000 time steps and over the period of calculation the computed and exact interface locations are in excellent agreement as seen in Fig. 5.7(a). The superposed exact and computed temperature fields are shown in Fig. 5.7(b).

A more stringent test of the planar interface propagation is in computing the higher Stefan number case, St=2.8576, ξ=0.9, shown in Fig. 5.8. The computations are performed with 61 grid points along the y-direction. Again remarkable agreement is obtained for computations over 100 time steps. For this higher Stefan number case, the interface moves more rapidly and a significant portion of the domain(Y_l=4) has been traversed by the interface.

From the above experiments it is clear that for a planar interface, the conservation statement across the interface is honored by the control volume formulation and the interface position is accurately obtained for a wide range of Stefan numbers.

5.5.3 Experiments with Non-planar Interfaces

In the computations to follow, we employ *nmax* grid points along the x-direction, where *nmax* is 21, 41 or 81 as mentioned. Since χ=4, and Y_l = 40 in

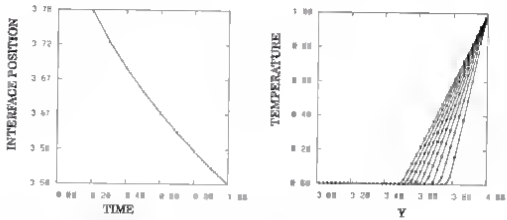

Fig 5 7 For Stefan No = 0 1303, comparison of exact and computed values (a) Interface position against time (b) Temperature along Y at different times

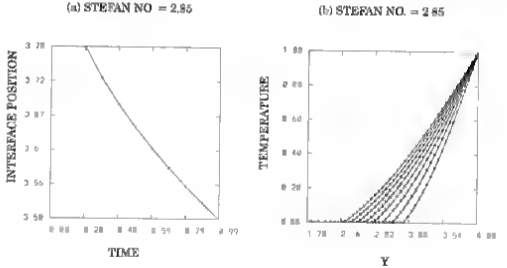

Fig 5.8 For Stefan No =2 85, comparison of exact and computed values (a) Interface position against time (b) Temperature along Y at different times.

all subsequent calculations, we have $\Delta x = 4/nmax$. Depending on the value of Δx, we employ grid points in the region II, such that $\Delta y_{II} = \Delta x$. As mentioned before, as the interface grows and propagates grids are added ahead of and deleted behind the interface. Thus the extent of region II increases as the computation proceeds.

The domain of computation is shown in Fig. 5.2. The liquid end was maintained at $\Theta_l = -40$, with the solid side at $\Theta = 1$. The side boundaries are adiabatic, i.e. $\frac{\partial \Theta}{\partial x} = 0$. The system of equations solved and the boundary conditions applied render the situation more akin to viscous fingering in Hele–Shaw cells than to a free dendritic growth environment. Thus, comparison with the boundary integral computations (DeGregoria and Schwartz, 1986) of that problem is justified, although such computations are performed for a semi-infinite domain.

5.5.3.1 Zero surface tension

The evolution of an isothermal interface was tracked on grids with $nmax = 21, 41$ and 81. The results are presented in Figs. 5.9, 5.10 and 5.11 respectively. Clearly, for the isothermal interface the results are governed to a large degree by the grid spacing. The behavior of interfaces with zero surface tension has been under scrutiny, with calculations indicating cusp-formation or tip-splitting (Bensimon and Pelce, 1986). Since in the absence of surface tension no stabilization mechanism exists at any length scale, i.e., there is no smoothing effect, the disturbances of all wavelengths are amplified. Thus, finite-time singularities can form on the interface. Our calculations show that on the $nmax = 21$ grid, displayed in Fig. 11, the perturbation grows for the period of calculation and loses symmetry. The source of asymmetry comes from the uni-directional procedure used to define the interface shape and temperature gradients. For $nmax = 41$, Fig

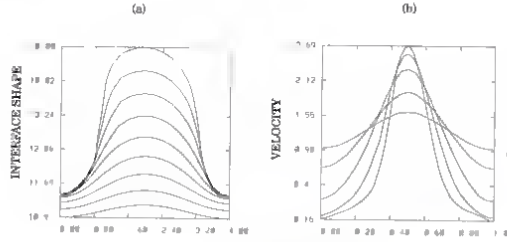

Fig 5 9 Development of interface for zero surface tension, nmax=21 grid Upto time=1 5 in steps of dt=0 2 (a) Interface shapes et different time instants. (b) Velocity along the interface at 5 time instants Arrows show sequence in time.

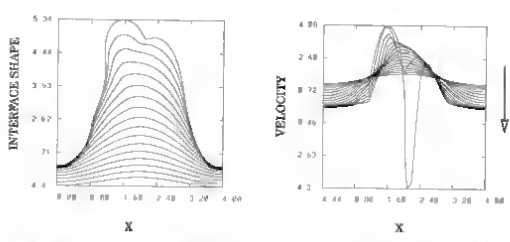

Fig. 5.10 Development of the interface for zero surface tension, nmax=41 grid. Upto time=1 8 in steps of dt=0.1. (a) Interface shapes at different time instants (b) Velocity along the interface at time instants corresponding to (a)

5 10, the interface first loses its symmetry, similar to the 21 grid case, and as time elapses, the perturbation wavelengths permitted by the grid lead to a tip–splitting instability A trough is formed upon tip–splitting, and rapid accumulation of latent heat ensues there leading quickly to the formation of a cusp in that region. Thus, the sharp corner created there cannot be smoothed out in the absence of surface tension For the finest grid, $nmax=81$, the interface becomes unstable to grid–scale oscillations These short wavelength oscillations grow faster than the disturbances that are captured on the coarser grid and a cusp rapidly forms at the boundary where the imposed periodicity condition becomes incompatible with the asymmetric breakdown of the interface The results on this fine grid correspond to our previous results obtained by employing boundary–fitted adaptive grids There, in the absence of surface tension, a cusp formed at the boundary, and short wavelength oscillations developed on the interface The simulation in this case, could however be carried farther than previously, because the grid is not required to conform to the interface.

The behavior of the interface under different grid resolutions has been investigated It is interesting that with the different grid resolutions, different modes of instability, including asymmetry, singularities and tip–splitting can appear Figures 5 9 to 5 11 indicate that there is no preferred morphological shape for the zero surface tension case Furthermore, because there is no prevailing physical length scale contained by the instability development itself, the numerical resolution in effect controls the smallest length scales of the instability As the grid is refined finer instability scales appear implying that no grid independent solution can be obtained with zero surface tension The progressively perturbed nature of the interface, with improved grid resolution can be seen from the velocity profiles in Figs 5 9(b), 5 10(b) and 5 11(b) It is noticed in each case that asymmetry develops in the interface profiles. It was found in most of our calculations

where the interface was highly unstable (i e. for zero and low surface tensions) that asymmetric breakdown persisted In addition, the breakdown always occurred on the same side of the domain, namely on the left. Such asymmetric breakdowns have been remarked upon in connection with experiments on the Saffman–Taylor instability (Tabeling et al, 1987) and in the Boundary Integral simulations of DeGregoria and Schwartz (1985) In the latter, when symmetry was not imposed, the interface became unstable asymmetrically When sufficient surface tension is present, it will be shown that the asymmetry is eliminated Thus, for the highly sensitive low surface tension cases, any small noise generated in the course of the computation leads to a breakdown of the smooth perturbation

5.5.3.2 Low surface tension

The sensitivity of the solution procedure can be demonstrated by adding a surface tension $\gamma_{eff} = 10^{-3}$ where, as defined previously, $\gamma_{eff} = \varepsilon_2 \theta_m \gamma^*$ Since the curvature is O(1), the Gibbs–Thomson condition will lead to interface temperature variations of $O(10^{-3})$ This modification of the temperature at the interface is extremely small when compared to the non–dimensionalized undercooling value $\Theta_l = -40$ imposed at the liquid boundary When this small value of surface tension is added the $nmax = 81$ calculation does not lead to a cusp at the boundary and the interface remains smooth By comparing Figs 5 11 and 5 12, it is seen that even such small γ_{eff} eliminates the singularities at the interface. However, the perturbations along the interface continue to grow Following the interface evolution further from the stage shown in Fig 5 12(a), a series of instabilities on the interface appears These instabilities develop in the vicinity of the tip and result in the asymmetric convoluted structure shown in Fig 5 13(a) To help present the interface characteristics more clearly, the interfacial velocity is shown plotted against arclength along the interface in Fig 5 13(b) The interface is highly distorted in this case, demonstrating the ability of the numerical technique developed here to

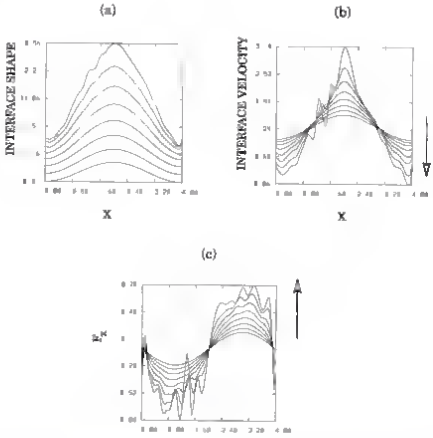

Fig 5 11 Development of the zero surface tension interface on an nmax=81 grid The computations were stopped at t=0 8 due to cusp formation at the boundary (a) Interface shape plotted at equal time intervals (dt=0 1) (b) Velocity along the interface plotted at the same time instants (c) f_x along the interface against x Arrows show sequence in time

handle such strongly multiple–valued shapes It is also noted that while one side of the interface appears to break into a cascade of protuberances in the vicinity of the tip, the other side remains quite stable The further development of the side branches is found to be arrested due to the accumulation of heat in the sides of the growing finger The imposition of the adiabatic side–wall condition prevents the removal of heat from this region Figures 5 13(c) and (d) show the isothermal

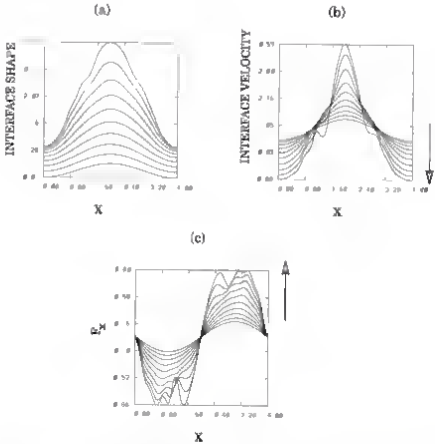

Fig 5 12 Development of the interface on the nmax=51 grid for surface tension γ_{diff}=0 001 Upto time t=0 8 No cusp is formed (a) Interface shape plotted at equal time intervals (dt=0 1) (b) Velocity along interface at same times (c) f_x along the interface against x.

contours in the vicinity of the interface in the early and later stages of the development shown in Fig 5 13(a) As is clearly seen, the temperature field calculation responds to the highly distorted nature of the interface, even for such a low value of the interface temperature Furthermore, the clustering of the isotherms to the left of the tip clearly drives the instability in that region leading to a mutually enhancing dynamic process between the interface and thermal field. In comparison

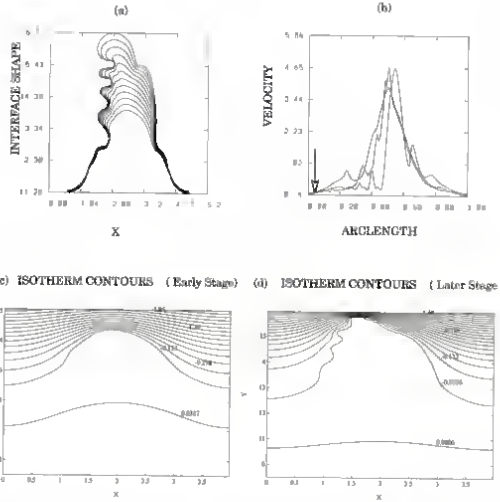

Fig 5 13 Development of interface for low surface tensions (10^{-5}) on nmax=81 grid From time t=0 8 to t=2 0 (a) Interface shapes at different time instants Successive instabilities occur along the interface (b) Velocities along the interface drawn at three instants of time against arclength (c) Isotherm plot at early stage showing asymmetry (d) Isotherms at later stage showing response of thermal field to distorted interface even for the very low value of surface tension

the isotherms on the right side are seen to be less crowded.

Figure 5 14(a) shows the evolution of the perturbation on the $nmax$=41 grid for $\gamma_{eff}=10^{-3}$ In this case again the instability results in tip splitting However, it is notable that while for the zero surface tension case the trough formed upon tip−splitting developed into a sharp corner, here surface tension rounds out the corner thus illustrating the subtle stabilizing effect

Developing further on the issue of surface tension as a subtle mechanism, we impose, continuing from the final stage shown in Fig 5 12, a surface tension $\gamma_{eff}=10^{-2}$ The subsequent evolution of the interface is followed and contrasted with the $\gamma_{eff}=10^{-3}$ case shown in Fig 5 13 The result is displayed in Fig 5 15 The successive instabilities have been completely suppressed by surface tension Also, interestingly, the resulting stable finger growth appears to be regaining symmetry as can be seen from the plots of velocity and interfacial derivatives, which are smooth in this case, but for residual short wavelength modes from the instabilities in the formative period Figures 5 13 and 5 15 are based on the identical initial conditions but different γ_{eff} in subsequent stages. The different results obtained demonstrate that the numerical technique maintains the history of the interface with satisfactory accuracy

5.5.3.3 Imposition of symmetry

For low surface tension cases computational studies that impose symmetry may result in interface patterns different from those without such constraint, due to the fact that the morphology of the interface is highly path dependent Any change in the boundary conditions or computational details will create different numerical noises, which in turn yields different final interface shapes. To illustrate the impact of enforcing symmetry on the interface for low surface tension,

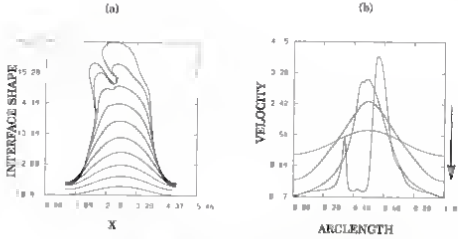

Fig 5 14 Development of interface for low surface tension $\gamma_{eff} = 10^{-3}$ for nmax=41 grid Addition of surface tension rounds out the trough after tip−splitting Upto t=2 0 (a) Interface shapes at equal intervals of time (dt=0 1) (b) Velocity of the interface shown at 4 different time instants, ax e function of nomalized arclength

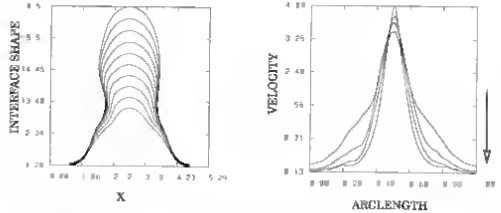

Fig 5 15 Effect of increasing surface tension for nmax=81 grid Surface tension $\gamma_{eff} = 10^{-2}$. Interface evolution from t=0 8 to t=2 0 The initial condition is the final stage in Fig 14 (for $\gamma_{eff} = 10^{-3}$, t=0 8). (a) Interface shapes at equal intervals of time showing stabilization and symmetrization (b) Velocity along the interface at four different time instants showing symmetrization

we compute the development of only half the perturbation by imposing symmetry condition for the other half For the $nmax=81$ case with low surface tension $\gamma_{eff} = 10^{-3}$ the resulting symmetric structure is shown in Fig 5 16 There is again a series of instabilities in the vicinity of the tip reminiscent of the structures observed in the Saffman–Taylor experiments with tip bubbles (Couder et al., 1986) On a finer grid, $nmax=161$, a similar phenomenon results as shown in Fig 5 17, except that in this case the tip breaks down at shorter wavelengths, and the instability development is much more rapid than in the case of the coarser grid calculations Thus, imposition of symmetry does not influence the stability of this low surface tension interface. The shape of the computed interface is however, very different from the case where symmetry is not explicitly imposed Nevertheless, the wavelengths in both Fig 5 16 and Fig 5 17 are quite comparable, which is consistent with the fact that grid resolution is the main cut–off length scale with zero or low surface tension. It should be clarified however that as long as surface tension is non–zero, there exists a physical length scale to control the morphological length scale of the interface. The results discussed so far, however, are for very low surface tensions which creates a length scale too small to be resolved by the grid spacing employed here

5.5.3.4 Stable fingers for significant surface tensions

The extreme sensitivity of the low surface tension cases to grid spacing, which yield widely different behaviors upon refinement prompts us to confirm grid independence for the more stable higher surface tension cases As already explained, this exercise can be conducted only for non–negligible surface tension cases

Fig 5 18 compares the interface shape and velocity of an interface with $\gamma_{eff} = 10^{-2}$, $nmax=41$ (full lines) and $nmax=81$ (open circles) While in the initial stages of development the profiles as well as interface velocities are in agreement,

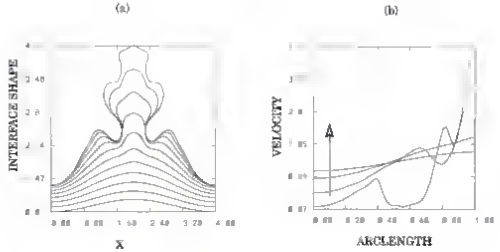

Fig. 5.16 Effect of imposition of symmetry on development of interface for low surface tension ($\gamma_{eff} = 10^{-3}$) on nmax=81 grid. (a) Interface shapes shown after reflection (b) Velocity along left half of interface against normalized arclength.

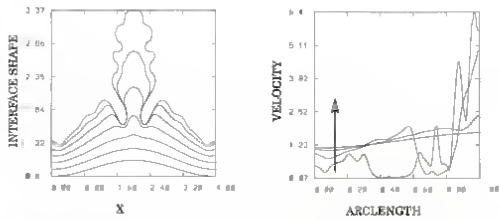

Fig. 5.17 Effect of imposition of symmetry on development of interface for low surface tension ($\gamma_{eff} = 10^{-3}$) on nmax=161 grid. (a) Interface shown after reflection (b) Velocity along left half of interface against normalized arclength

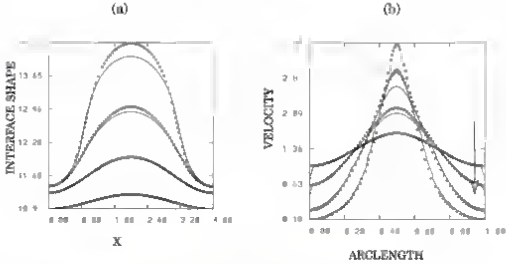

Fig 5 18 Comparison of solutions for surface tension $\gamma_{eff} = 10^{-2}$ on nmax=41 (full lines) and nmax=81 (open circles) grids (a) Interface shapes at different time instants (b) Interface velocities at same times as in (a)

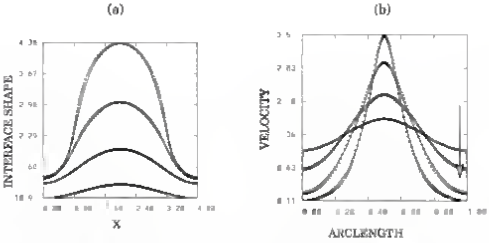

Fig 5-19 Comparison of solutions for surface tension $\gamma_{eff} = 10^{-2}$ on nmax=81 (full lines) and nmax=161 (open circles) grids (a) Interface shapes at different time instants (b) Interface velocities at same times as in (a)

as the perturbation develops to large amplitudes the coarser grid calculation underestimates the instability magnitude In fact the final stage of the fine grid calculation shows a vastly different value of velocity Fig 5 19 compares the same interfacial development for $nmax$=81 (full line) and $nmax$=121 (open circles) As can be seen, the two calculations maintain close consistency, even in the large amplitude stage The velocities in the final stage are in close agreement Thus, for high enough surface tension, grid effects are suppressed and the stable finger growth converges under grid refinement. In subsequent calculations we employ $nmax$=81

Figure 5 20 shows the development of a finger for $\gamma_{eff} = 10^{-2}$, along with the derivatives along the interface. The first observation to make regarding these results is the well maintained symmetry of the front Figure 5.21 shows the development of the finger for γ_{eff}=0 1 . The interfaces are shown at the same instants of time The effects of surface tension are brought forth by comparing these two sets of results The qualitative features are in agreement with the computations of DeGregoria and Schwartz (1986) who used the boundary element method In particular, the rapid accumulation of heat on the sides of the finger leads to a rapid slowdown of the interface in that region. The front propagates upward farther in the higher surface tension case before the instability gathers momentum The amplitudes of the $\gamma_{eff} = 10^{-2}$ finger (aspect ratio $\approx$ 4) is greater than the $\gamma_{eff} = 0$ 1 finger (aspect ratio $\approx$ 2 5) demonstrating the higher degree of instability for lower surface tension As can be seen in the plot of the interfacial derivatives against x (Figs 23 (c),(d) and (e)) , the higher surface tension (10^{-1}) causes the finger to spread laterally, leading to a multiple−valued interface with respect to x The sides of the lower surface tension (10^{-2}) finger are almost flat and vertical, indicating minimal lateral spreading The circular arc fits for representing the interfacial segments hold up very well even for such a flat vertical surface. As can be

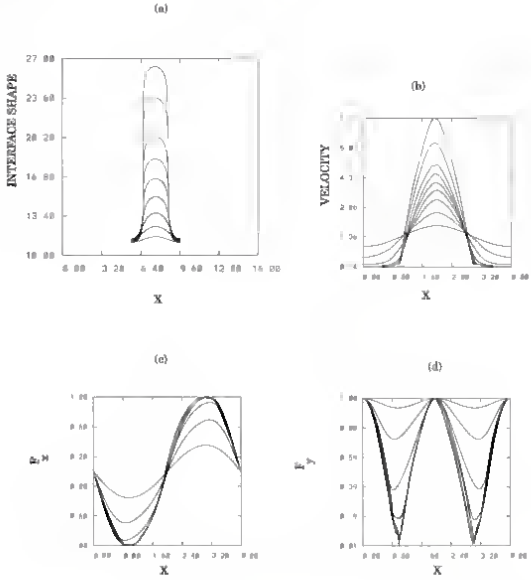

Fig 5 20 Development of interface for surface tension $\gamma_{\text{eff}} = 10^{-2}$ Upto t=4 0 (a) Interface shapes at equal intervals of time The finger has been drawn to scale (b) Velocity along interface against x (c) $\mathbf{F}_x$ along interface against x. (d) $\mathbf{F}_y$ along interface vs. x

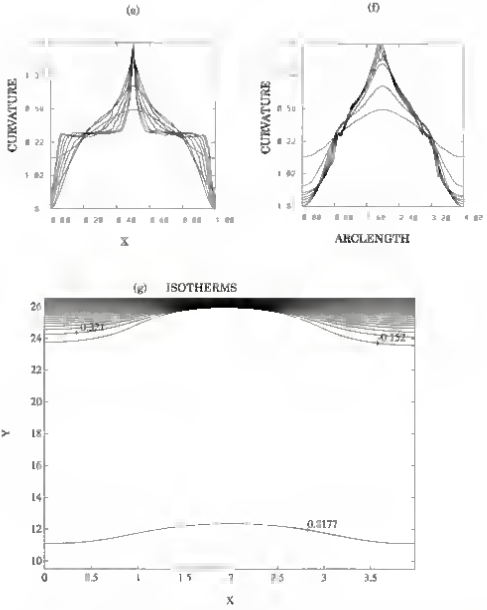

Fig 5.20 – – continued (e) Plot of curvature along the interface against x (f) Plot of curvature against arclength (g) Isotherm contours including entire interface

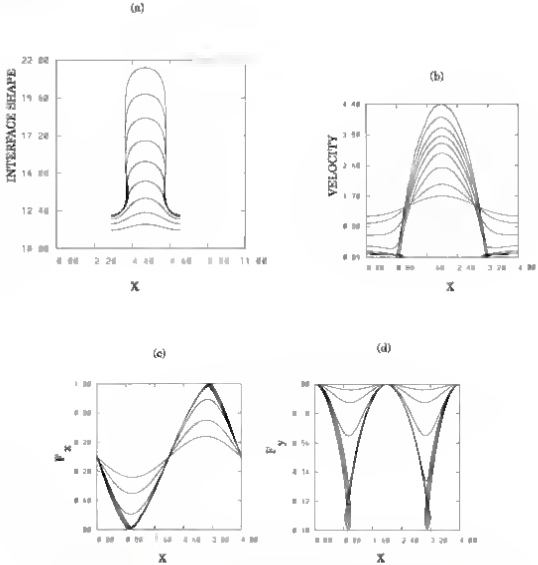

Fig 5 21 Development of interface for surface tension $\gamma_{eff} = 10^{-1}$ Upto t=4 0 (a) Interface shapes at equal intervals of time. The finger has been drawn to scale (b) Velocity along interface against x. (c) F_x along interface against x (d) F_y along interface vs x

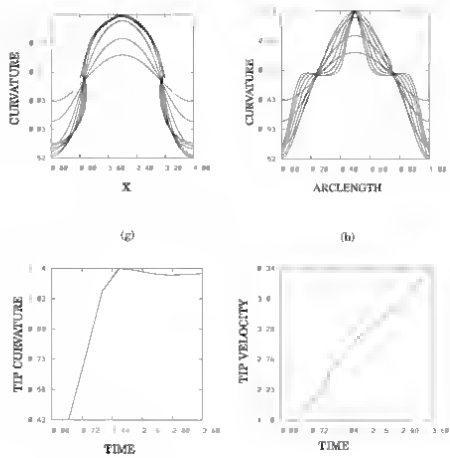

Fig 5 21 — continued (e) Curvature along interface versus x. (f) Plot of curvature against normalized arclength (g) Tip curvature variation with time (h) Tip velocity with time.

seen by comparing the plots of curvature against x , the finger in the higher surface tension case has a more rounded tip and there is a wide region near the tip where the curvature is nearly a constant. In contrast, for the case of $\gamma_{eff}=10^{-2}$ the finger is sharper at the tip At the stage of the development shown, as seen from the plots of interfacial derivatives against x the interfaces in both cases ap—

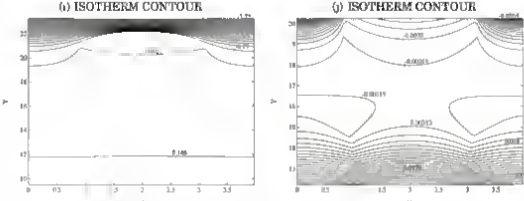

Fig 5 21 – – continued (i) Isotherm contours for entire finger (j) Isotherm contours for portion of finger not including tip.

pear to have attained stable, shape–preserving growth. This may also be seen for the $\gamma_{eff} = 0.1$ case from the plots of tip curvature and velocity with time, shown in Fig 5 21 (g) and (h) However, as observed by Saffman and Taylor (1958), over a substantial length and time, the growth velocity of the finger is not constant and the tip is still accelerating due to the finite domain size in our calculation. As the finger reaches an asymptotically invariant shape, the tip velocity will approach constant values.

Fig. 5 21(i) shows the isotherms in the vicinity of the interface for the $\gamma_{eff} = 0.1$ case. The finger in this case extends from about Y=12 to 21. Clearly the clustering of the isotherms at the tip drives the instability The Gibbs–Thomson effect causes the isotherm corresponding to $\Theta = -2.2 \times 10^{-2}$ to curve inward in the tip region where the curvature is positive The symmetry of the isotherms confirms our previous statement regarding the ability of the surface tension to suppress asymmetry Fig 5 21(j) shows isotherms across the interface. The effect of the Gibbs–Thomson condition is seen to propagate far down the solid finger as evident from the curvature of the -2.19×10^{-2} isotherm at Y=18, which is well into the solid finger The curvatures of the isotherms however change sign further

down, as for the Θ=3.53 x 10^{-3} isotherm. The isotherm plot for γ_{eff} = 0.01, Fig 5.20(g), shows no sign of the Gibbs–Thomson condition for the available contour resolution. The first negative isotherm is in the correct position since the tip of the finger is located approximately at Y=27, in agreement with the isotherm plot.

The results presented above have demonstrated that the numerical method developed can perform the task of tracking multiple–valued, large amplitude, unstable interfaces. The effects of surface tension have been remarkably well represented. The temperature field has been computed with fidelity as evident from the plot of isotherms for the highly nonlinear stages of instability.

5.6. Conclusions

We have now developed a method for tracking highly distorted fronts on fixed Cartesian grids under the influence of conductive heat transport. The facility afforded by the Cartesian grid in terms of setting up the control volume formulation leads to a conservative heat flux treatment across the moving interface. The execution of these procedures is fairly simple and involves dealing with a one–dimensional array of interfacial cells. Non–interfacial cells are assembled as usual. Thus, in contrast with other Eulerian methods, it is possible here to explicitly specify the location and shape of the interface and to apply the boundary conditions at the exact location of the interface. In strictly Lagrangian methods on the other hand, the grid translates with the interface and needs to be periodically smoothed and redistributed. The non–boundary–fitted grid layout here circumvents such problems. The method has been tested first against available exact solutions. For a planar interface the Neumann solutions for a melting problem have been accurately reproduced by the numerical solutions. The results for the deformed interface illustrate clearly the effects of surface tension. In the absence of surface tension, singularities quickly develop on the front for sufficient grid res-

olution The interaction of grid resolution, which governs the wavelength of noise on the interface with the surface propagation is seen to affect the interfacial evolution In particular, at very low surface tensions the disturbances allowed by the grid strongly influence the fate of the interface Thus care needs to be exercised in interpreting results in this range of surface tension parameter For sufficient interfacial tension, the results have been demonstrated to converge under grid refinement The initial perturbation develops in time into long fingers, as in the Saffman–Taylor problem The qualitative features are in agreement with other simulations of the fingering phenomenon The finger shapes reach steady–state, while the tip continues to accelerate due to the fixed domain size and boundary conditions.

As demonstrated in this chapter, it is now possible to track unstable, multiple–valued interfaces with conduction heat transfer in the solid and liquid phases The solution methodology developed can be extended in its essential features to include convection in the melt While the inclusion of convection calls for several additional details to be incorporated in the numerical technique, this chapter provides most of the guidelines for the development of field solvers employing an implicit in time, control volume formulation The extension to include convective transport is accomplished in the next chapter

CHAPTER 6

A COMPUTATIONAL TECHNIQUE FOR FLUID FLOWS WITH MOVING BOUNDARIES

6.1 Introduction

Although the idealized diffusion-controlled free dendritic growth process has resulted in deep insights into the physical mechanisms, it is accepted that in any realistic solidification processing arrangement it is impossible to avoid some form of convection (Brown, 1988, Glicksman et al , 1986, Favier, 1990, Ostrach, 1983) Fluid flow can arise in a variety of ways. Consider some typical solidification processes shown in Fig 6 1 In these crystal growth techniques, capillarity effects at the free surfaces lead to Marangoni convection, and the pulling of the crystal leads to forced flow Usually the crystal is also rotated in order to enforce uniformity along the circumferential direction, again leading to forced convection Additionally, in the presence of gravity, natural convection can occur due to the large temperature gradients imposed in the axial as well as radial directions The macroscopic solid-liquid interface therefore evolves under the influence of various forms of convection, whose strengths and flow features can vary depending on growth conditions In growing crystals of desired homogeneity one is concerned with precise control of the transport phenomena. In particular the distribution of impurities can be significantly affected by the presence of interfacial instabilities due to solute being trapped in regions between the cellular and dendritic structures described in Chapter 1 Such microsegregation can be influenced by convective effects In addition, the impurity and temperature distribution in

the vicinity of the interface is a function of the global flowfield and heat transfer characteristics. It is therefore clear that crystal growers have to contend with highly non-homogeneous unsteady growth environments and flowfields. In maintaining the uniformity of grown crystals it is important to assess or minimize/control the effects of convection at the global as well as morphological levels. For these reasons, the effect of convection on the macroscopic phase interface as well as the microstructure is an issue that has begun to receive increasing attention.

Based on the research on the fluid dynamics aspects, there is now abundant evidence on the effects of convection in the melt on the characteristics of the phase interface. For example, Fang et al. (1985) have experimentally observed a strong coupling of crystal-melt interface shape with convection in a long circular cylinder of pure Succinonitrile. The experiments of Gau and Viskanta (1986) on the melting of Gallium clearly demonstrate the effects of natural convection on the deformation of the macroscopic solid-liquid interface. Depending on the strength of convection, measured by the Rayleigh number, the interface can be severely distorted by the flow pattern. Several computational efforts have attempted to reproduce the experimental results, with varying degrees of success (Lacroix, 1984, Lacroix and Voller, 1990). A recent experimental result (Campbell et al., 1994) differs from the experiment of Gau and Viskanta as well as previous computations. The difficulty associated with identifying the interface in the opaque metallic melt, the high melting points in such systems and ambiguous initial conditions are the possible causes of the discrepancies. Herein lies a fundamental pitfall, in that while for diffusion controlled environments it is possible to employ transparent, low latent heat of fusion organic melts, it is not clear that such is the case when convection is included. This is because, as described in Chapter 2, the Prandtl numbers ($\mu C_p/k$) which define the relative importance of convection to thermal diffusion are vastly different for metals as compared to organic melts.

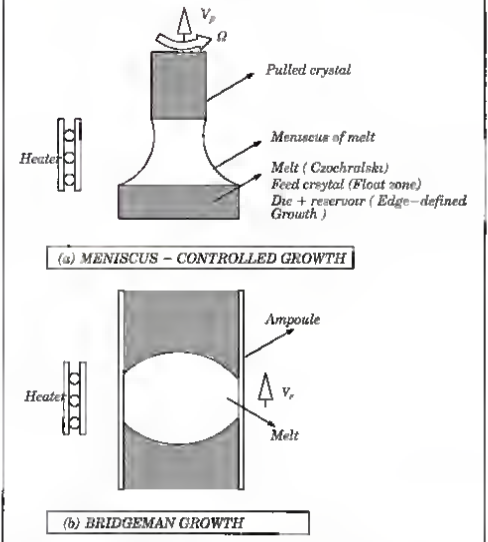

Fig 6 1 Two examples of solidification processing arrangements Different types of convection are possible, e.g , natural convection, forced flows due to pulling and rotation of crystal and shrinkage and Marangoni convection (a) Meniscus–controlled growth (b) Bridgeman growth.

Thus, the flow field in each case is likely to be very different, and it is no longer valid to extrapolate results regarding flow features and their effects from organic to metallic melts. Thus, even in the case of the macroscopic flow field, reliable experimental results for validation of solution techniques are scarce.

At the level of the microstructure the effects of convection are less well understood than in the macroscopic case. The onset of convection, and the interaction between the morphological instability and the convection induced instability of the interface in binary alloys has been investigated by means of linear stability analyses (Davis, 1990). The results appear to indicate that, but for very small growth rates, the scales of the morphological instability are widely separated from the convection induced instability, at least as far as the onset is concerned (Davis et al., 1984, Favier and Rouzaud, 1983, Forth and Wheeler, 1989 1991, Glicksman et al., 1986, McFadden et al., 1984). It is predicted that convective effects can induce travelling waveforms on the phase interface, even in the linear regime. The effect of forced and natural convection on a fully developed dendrite has also been treated analytically by adopting the Ivantsov paraboloid solution for the translating dendrite tip by Ananth and Gill (1989,1991). It has been shown that uniformly translating paraboloids are consistent solutions of the combined heat and Oseen flow equations. This is a useful result and enables one to simply extend the Ivantsov model from the pure conduction case to that where convection exists. However the analysis is restricted to the vicinity of the tip, where the Ivantsov paraboloid is indeed a valid solution to the pure conduction problem. As with any model based on the Ivantsov solutions a selection mechanism has to be devised. Ananth and Gill (1989) employ the microscopic solvability criterion to select out the appropriate solution. This of course involves the assumption that the solvability mechanism is valid, and that it also applies in the presence of convection. The experiments of Tirmizi and Gill (1987) on ice dendrites clearly demonstrate the effects

of natural convection on the growth of dendrites. Other issues of significance are the possibility of dendritic branch detachment due to forced convection effects (Sato et al., 1987). Such detachment is probably a mechanism for the columnar to equiaxed transition in melts. Recent experiments have shown the importance of convection on the transport and sedimentation of globulitic crystals, which eventually determines the shape of the macroscopic phase front (Beckermann, 1994). Boussou et al. (1990) conducted an experiment where an oscillatory velocity field was imposed on a Succinonitrile-Acetone dendrite growing in a directional solidification arrangement. It was shown that the dendritic sidebranching events were significantly influenced by the imposed forcing. In a natural dendrite, the dendritic side-branching events on the sides of the dendrites are essentially uncorrelated, on account of their being induced by noise as mentioned in Chapter 1. When the external forcing was imposed, the side branching was highly coherent. Furthermore, spectral analysis of the sidebranches revealed a resonance mechanism with the forcing frequency. In particular, for a range of frequencies the side-branching could be controlled, while outside this range the effects of forcing were minimal. As expected, the efficacy of the forcing was greatest in the vicinity of the natural dendritic sidebranching frequency. This experiment hints at the possibility of controlling microstructures by modifying the macroscopic flowfield.

The growing demand for high-quality alloys and semiconductors calls for a means to predict and possibly control the distribution of impurities/ additives in grown crystals. Instabilities at the solid-liquid interface can lead to patterns in the deposition of impurities (microsegregation) that may be detrimental to the performance of the materials solidified. It is important to be able to estimate such inhomogeneities in crystals, and their relation to the macroscopic flow features and solute concentration. The subject of convective influence on cellular/dendritic growth is an open area of research. Numerical simulation has, to our knowledge

not been reported at this time In what follows, we attempt to commence the simulation of the full crystal interface evolution problem with melt flow, for shapes that are not constrained to be of small distortion

In this chapter we develop a numerical simulation technique that can handle the conditions that are encountered during a typical solidification process, viz

a. the solid–liquid interface is a phase discontinuity, boundary conditions in each phase have to be applied for the fluid flow equations on this moving internal boundary The interface is a source of heat, mass and momentum and can be arbitrarily distorted.

b The method developed should be able to handle fluid flow in solidification processes at the macro- and micro-scales.

c. Other demands on the solution procedure are similar to those on the pure conduction system.

Hitherto, the computations of the full phase change problem including the Navier-Stokes equations have been restricted to the macroscopic aspects The most popular methods employed for the computations are purely Eulerian in nature, and employ variants of the enthalpy method (Lacroix and Voller, 1990, Shyy and Rao, 1993 Voller and Cross, 1981, Smith, 1981). The interfaces are then deduced from the contours of a transported scalar, such as fluid fractions. The interface is imparted a thickness in order to overcome the classical difficulty in dealing with sharp gradients/discontinuities in an Eulerian framework Thus, a porosity is assigned in the vicinity of the solid-liquid interface and a D'Arcy type term is included to smooth the drastic jump in viscosity across the interface (Shyy and Rao, 1993, Voller and Prakash, 1987). Thus, unless a very fine grid is employed in the vicinity of the interface, it is not possible to track a sharp phase front by these techniques At the level of the macroscopic interfaces the purely Eulerian methods are indeed useful for the following reasons

1. The macroscopic interface is unlikely to be highly distorted Thus, the interfacial boundary conditions which are functions of the interfacial curvature and slope such as the temperature and concentration at the phase front are unlikely to significantly impact on the global thermal and velocity fields In other words, the Gibbs-Thomson condition is unlikely to play an important role for small curvatures

2 For most materials containing impurities, there exists a mushy zone, which represents a region where the solid and liquid coexist. The information regarding the microstructure is averaged over this region If one is not concerned with detail in regard to the micro-scales, the interface can be smeared over this mushy zone This type of treatment of course lends itself to the purely Eulerian treatment where the interface is required to have a finite thickness.

3 The Eulerian methods, as mentioned before, also easily handle topological changes However, the accuracy of the computations in such events cannot be assessed

When the focus is on interfacial behavior at the microscopic levels, the issues that assume importance are capillarity, interfacial distortion and interfacial motion The interface then has to be treated as a discontinuity, which limits the applicability of a purely Eulerian scheme In order to deal with the situation at the morphological scales, we design a solution procedure along the lines of the method developed for the pure conduction problem in Chapter 5 The mixed Eulerian-Lagrangian, time implicit foundations of the method are maintained and the fluid flow equations are discretized Since we deal with incompressible flow for solidification from the melt, an attractive solution technique is the frequently employed pressure-based method (Patankar, 1979, Shyy,1984) In particular the general solution methodology follows the SIMPLE algorithm which we outline in Section 6 2 below In Section 6 2 1, we describe, for a general conserved variable

ϕ, the application of a control volume formulation and the discretization scheme. In section 6.2.4 we clarify the treatment of the individual terms for each of the flow variables and explain the various issues involved in relation to conservation and consistency. We cast the equations in the computational notation of the pressure-based methodology. We then present some test cases and comparisons to validate the solution procedure.

6.2. The control volume formulation for a transport variable ϕ

6.2.1 Discretization

Consider the conservation law for the variable ϕ, defined to be (a) 1 for the continuity equation (b) u and v for the x and y momentum equations and (c) specific enthalpy $C_p T$ for the energy equation. In the general case, we have

$$\frac{\partial(\rho\phi)}{\partial t} + \nabla \cdot (\rho\vec{u}\phi) = (\nabla \cdot \Gamma\nabla\phi) + S \qquad (6.1)$$

Consider the interface that passes through a Cartesian grid at a given instant. The control volumes in the vicinity of the interface are irregularly shaped, and in the most general case can assume a five-sided shape as shown in Fig. 6.2 below. In order to evaluate the momentum fluxes through the cell faces, we integrate Eq. (6.1) over the control volume and employ the divergence theorem to get

$$\int_V \frac{\partial\rho\phi}{\partial t} dV + \int_A (\rho\vec{u}\phi) \cdot \vec{n} dA = \int_A (\Gamma\nabla\phi) \cdot \vec{n} dA + \int_V S dV \qquad (6.2)$$

In two-dimensions we have

$$\int_A \frac{\partial\rho\phi}{\partial t} dA + \oint_l (\rho\vec{u}\phi) \cdot \vec{n} dl = \oint_l (\Gamma\nabla\phi) \cdot \vec{n} dl + \int_A S dA \qquad (6.3)$$

where the second term on the left hand side is now the line integral of the outward normal convective fluxes and the first term on the right side is the line integral of the outward normal diffusion fluxes through the faces of the control volume. We now proceed to discretize each of the terms in Eq. (6.3) for the control volume

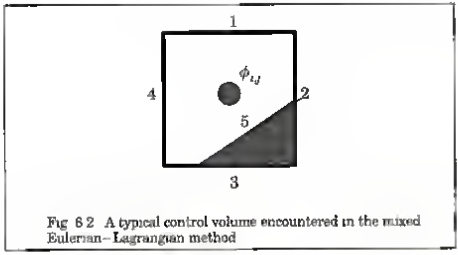

Fig. 6.2 A typical control volume encountered in the mixed Eulerian–Lagrangian method

shown. Thus

$$\int_A \frac{\partial(\rho\phi}{\partial t} dA = \frac{\rho^{n+1}_{i,j}\phi^{n+1}_{i,j} - \rho^{n}_{i,j}\phi^{n}_{i,j}}{\delta t} A_{cv} \tag{6.4}$$

where the superscript n, $n+1$ indicate the time levels and δt is the time step size. A_{cv} is the area of the irregular control volume. Next,

$$\oint_l (\rho\vec{u}\phi) \cdot \vec{n} dl = \sum_{k=1}^{5} (\rho_k u_k \phi_k)^{n+1} dl_k \tag{6.5}$$

is the summation of the convective normal effluxes through each cell face of the control volume. The superscript $n+1$ indicates the implicit nature of the scheme. The diffusion fluxes are computed as

$$\oint_l (\Gamma\nabla\phi) \cdot \vec{n} dl = \sum_{k=1}^{5} (\Gamma_k (\frac{\partial\phi}{\partial n})_k)^{n+1} dl_k \tag{6.6}$$

Let us denote the source term as follows,

$$\int_A S dA = \bar{S} \tag{6.7}$$

Substituting the above Eqs. (6.4–6.7) in Eq. (6.3) one obtains the discretized form as

$$\frac{\varrho^{n+1}{}_{i,j}\phi^{n+1}{}_{i,j} - \varrho^{n}{}_{i,j}\phi^{n}{}_{i,j}}{\delta t}A_{cv} + \sum_{k=1}^{5}(\varrho_k u_k \phi_k)^{n+1}dl_k = \sum_{k=1}^{5}(\Gamma_k(\frac{\partial\phi}{\partial n})_k)^{n+1}dl_k + \bar{S} \tag{6.8}$$

In particular the discrete form of the continuity equation can be written as

$$\frac{(\varrho^{n+1}_{i,j} - \varrho^{n}_{i,j})}{\delta t}A_{cv} + \sum_{k=1}^{5}(\varrho u_n)_k dl_k = 0 \tag{6.9}$$

Now multiplying Eq (6.9) by the value $\phi_{i,j}$ and subtracting from Eq (6.8) gives

$$\frac{\varrho^{n}{}_{i,j}(\phi^{n+1}{}_{i,j} - \phi^{n}{}_{i,j})}{\delta t}A_{cv} + \sum_{k=1}^{5}\varrho_k u_k(\phi_k - \phi^{n+1}_{ij})^{n+1}dl_k = \sum_{k=1}^{5}(\Gamma_k(\frac{\partial\phi}{\partial n})_k)^{n+1}dl_k + \bar{S} \tag{6.10}$$

6.2.2 The staggered grid

The solution of the discrete form, namely Eq (6.10) is carried out on a staggered grid arrangement shown in Fig 6.3. Staggered grids have been extensively adopted for computation of incompressible fluid flows due to their many advantages (Patankar,1979, Shyy, 1994) The variables and their respective control points are located as indicated in Fig 6.3 The interface is thus required to be tracked on such a grid arrangement. The definition of the control volumes, which is carried out according to the intersection procedure is now applicable to each type of control volume shown, namely the u, v and (p,T) control volumes For a given control volume then, the interface tracking procedure provides the information shown in Fig 6.4. Thus, at each iteration, explicit definition of the interface location/control volumes for each variable and its grid is available. This facilitates the application of boundary conditions on the faces of the cells containing the interface, as explained later.

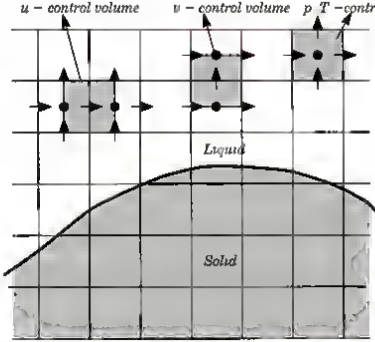

Fig 6 3 Control volumes for u,v,p and T variables showing the staggered arrangement

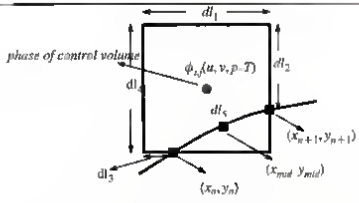

Fig 6 4 Illustration of information provided by the interface tracking module during assembly of coefficients for control volumes

6.2.3 Computation of the pressure field

For incompressible flows, since no explicit equation exists for the pressure field, some method needs to be devised to compute the pressure field. To extract the pressure, one makes use of the continuity equation and obtains a correction equation for the pressure and velocities that enforces mass conservation. The correction procedure is continued until convergence is achieved for each time step. Such a pressure correction method has been widely used and is described in detail elsewhere (Patankar,1979). The essential feature is that the following equation results for the pressure correction at each point

$$a_P p'_P - a_N p'_N - a_S p'_S - a_E p'_E - a_W p'_W = \frac{(\varrho^n_P - \varrho_P)A_{cv}}{\delta t} + \varrho_w u_w dl_w - \varrho_e u_e dl_e + \varrho_s v_s dl_s - \varrho_n v_n dl_n \qquad (6.11)$$

where the right hand side represents the mass deficit in the control cell, and is required to be nullified at convergence. The individual terms on the right hand side are mass fluxes through the faces of the control volume, including the interfacial segments.

6.2.4 Computation of convective and diffusive fluxes and source terms

We may return now to Eq. (6.10), for the situation shown in Fig. 6.5 below. It is standard in the notation of pressure-based implicit methods to identify the variables at time level n with superscript 'o' and leave the variables at the current time level $n+1$ without superscripts. Using this conventional notation and rewriting Eq. (6.10) for the variable ϕ, the convective fluxes are evaluated as follows

$$\sum_{k=1}^{5}(\varrho u_n)_k(\phi_k - \phi_P)dl_k = (\varrho_e u_e)(\phi_e - \phi_P)dl_e - (\varrho_w u_w)(\phi_w - \phi_P)dl_w + (\varrho_n u_n)(\phi_n - \phi_P)dl_n - (\varrho_s u_s)(\phi_s - \phi_P)dl_s \pm (\varrho_l u_{nl})(\phi_l - \phi_P)dl_l \qquad (6.12)$$

which may be written as,

$$\sum_{k=1}^{5}(\varrho u_n)_k(\phi_k-\phi_P)dl_k = F_e(\phi_e-\phi_P)-F_w(\phi_w-\phi_P) + F_n(\phi_n-\phi_P)-F_s(\phi_s-\phi_P)\pm\varrho\mu_{ni}(\phi_I-\phi_P)dl_I \tag{6 13}$$

Here the F's stand for the mass fluxes through the faces of the control volume. The lower case subscripts indicate the values at the cell faces Subscript I indicates the values at the interface. The manner in which these fluxes are evaluated , i.e , the specific shape function assumed for the variable ϕ for evaluation of thass fluxes determines the order of accuracy of the scheme employed In Eq (6 13) the sign of the last term is to be decided. What is required is the outward normal flux from the interfacial segment We shall return to this point momentarily.

Now, the diffusion fluxes can be written as

$$\sum_{k=1}^{5}\Gamma_k(\frac{\partial\phi}{\partial n})_k dl_k = \Gamma_e(\frac{\partial\phi}{\partial x})_e dl_e - \Gamma_w(\frac{\partial\phi}{\partial x})_w dl_w + \Gamma_n(\frac{\partial\phi}{\partial y})_n dl_n - \Gamma_s(\frac{\partial\phi}{\partial y})_s dl_s \pm \Gamma_I(\frac{\partial\phi}{\partial n})_I dl_I \tag{6 14}$$

Substituting the expressions provided by Eqs (6 13) and (6 14) in Eq (6 10) and simplifying, we now obtain

$$\frac{\varrho_P{}^{c}(\phi_P-\phi_P{}^{o})A_{cv}}{\delta t} + (J_e-F_e\phi_P)-(J_w-F_w\phi_P)+(J_n-F_n\phi_P)-(J_s-F_s\phi_P) = \pm\Gamma_I(\frac{\partial\phi}{\partial n})dl_I \mp \varrho\mu_{ni}dl_I(\phi_I-\phi_P)+\overline{S} \tag{6 15}$$

where

$$J_e = \varrho_e u_e dl_e\phi_e - \Gamma_e(\frac{\partial\phi}{\partial x})_e dl_e \tag{6 16}$$

and

$$J_n = \varrho_n v_n dl_n\phi_n - \Gamma_n(\frac{\partial\phi}{\partial y})_n dl_n \tag{6 17}$$

with similar expressions for J_w and J_s. The following notation is standard for the SIMPLE algorithm (Patankar,1979)

$$J_e - F_e\phi_P = a_E(\phi_P-\phi_E) \tag{6 18}$$

$$J_w - F_w\phi_P = a_W(\phi_W - \phi_P) \tag{6 19}$$

with similar expressions for a_N and a_S The forms assumed by $a_{E\,W\,N\,S}$ determine the order of accuracy of the differencing scheme employed For example

$$a_E = D_e A(|P_e|) + [-F_e, 0] \tag{6 20}$$

where P_e is the cell Peclet number $= F_e/D_e$ and the square bracket implies the maximum of the two quantities In this work the second-order central difference scheme is employed to discretize spatial derivatives, for which

$$A(|P|) = \mathbf{1} - 0\,5|P| \tag{6 21}$$

The Eq (24) can now be written as

$$\frac{\varrho_P{}^n(\phi_P - \phi_P{}^o)A_{cv}}{\delta t} + a_E(\phi_P - \phi_E) - a_W(\phi_W - \phi_P) + a_N(\phi_P - \phi_N) - a_S(\phi_S - \phi_P)$$
$$= \pm\, \Gamma_l(\frac{\partial\phi}{\partial n})_l dl_l \mp \varrho\mu_{nl} dl_l(\phi_l - \phi_P) + \overline{S} \tag{6 22}$$

Letting

$$\frac{\varrho_P{}^n A_{cv}}{\delta t} = a_P{}^o \tag{6 23}$$

and

$$a_P = a_P{}^o + a_E + a_W + a_N + a_S \tag{6 24}$$

we have the final discretized form

$$a_P\phi_P = a_N\phi_N + a_S\phi_S + a_E\phi_E + a_W\phi_W + b \tag{6 25}$$

where

$$b = \overline{S} \pm \Gamma_l(\frac{\partial\phi}{\partial n})_l dl_l \mp \varrho\mu_{nl} dl_l(\phi_l - \phi_P) \tag{6 26}$$

In the above discretization, the value of ϕ at any point P is dependent on its four immediate neighbors When cast in matrix form the equation reads—

$$[C]\ [\Phi] = [B] \tag{6 27}$$

where $[C]$ is a pentadiagonal coefficient matrix, Φ is the solution vector and B is a source vector The procedure usually adopted is to solve the system of equations in iterative fashion employing a line SOR method which calls for a tridiagonal matrix solution procedure

6.2.5 Computation of interfacial fluxes

We now proceed to detai the method for obtaining the interfacial flux terms. Considering the fluxes from the interface,

$$\pm \Gamma_I(\frac{\partial \phi}{\partial n})_I dl_I \mp \rho_l u_{nI} dl_I(\phi_I - \phi_P) \tag{6.28}$$

We need to estimate the following quantities at the interface ,

$$(\frac{\partial \phi}{\partial n})_I \quad , \quad \rho_l u_{nI} \quad , \quad \phi_I \tag{6.29}$$

and determine the missing signs to evaluate the flua terms As for the above values at the interface, ρ_I is easily obtained for incompressible flow as the value of the density at the liquid control point closest to the interface. u_{nI}, the fluid velocity

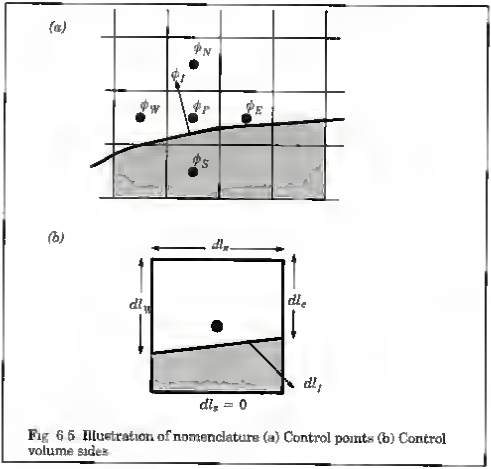

Fig 6.5 Illustration of nomenclature (a) Control points (b) Control volume sides

normal to the interface is evaluated from the boundary condition at the interface, Eq (1 15), once the interfacial velocity at that point is known The interfacial velocity is of course determined from the Stefan condition, Eq (1 17), during the course of the calculation and is coupled to the temperature gradients in the vicinity of the interface The normal gradient of any variable ϕ at the interface, i e , $(\partial\phi/\partial n)_I$ is evaluated in the same fashion as for the pure conduction problem A probe is inserted in each phase and a biquadratic shape function is described in the vicinity of the interface The derivative can then be estimated The value of

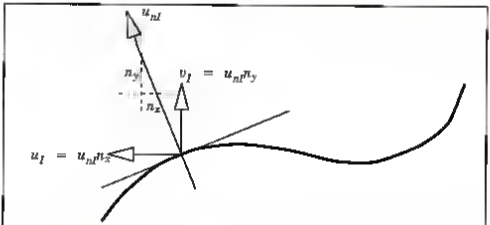

Fig 6 6 Illustration of velocity components of fluid at the interface

the variable on the interface ϕ_I, is again obtained from the boundary conditions In particular, for

1 The u-momentum equation, $\phi = u$, and $u_I = u_{nI}\, n_x$ as shown in Fig 6 6

2 The v-momentum equation $\phi = v$, and $v_I = v_{nI}\, n_y$ as shown in Fig 6 6.

3 For the energy equation $\phi = T$ and T_I is obtained from the Gibbs-Thomson condition at the interface.

Next, we need to decide upon the signs to be assigned to each of the interfacial fluxes The diffusion flux with the as yet undetermined sign is

$$\pm \Gamma_I (\frac{\partial \phi}{\partial n})_I dl_I \tag{6 30}$$

The positive sign is applicable when an outflux is evaluated By the procedure outlined above, the gradient evaluated is as follows

$$\frac{\partial \phi}{\partial n} = (\frac{\phi_{I+dn} - \phi_I}{dn}) \tag{6 31}$$

for the situation shown in Fig 6 7.

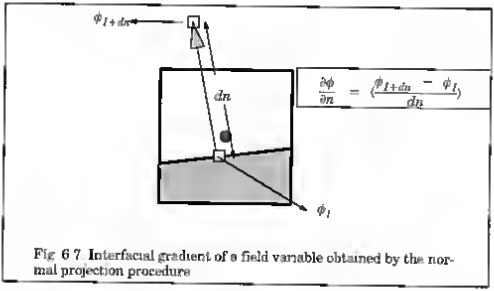

Fig 6 7 Interfacial gradient of a field variable obtained by the normal projection procedure

The gradient as evaluated above represents the influx into the control volume in each phase A negative sign is therefore required to provide the efflux from the control volume As for the sign of the convective interfacial flux, we have adopted the convention that the normal points into the liquid phase Hence, u_{nI} is the normal velocity of the fluid at the interface, and is directed into the liquid control volume. Therefore, the convective flux into the control volume is given by

$$\varrho \mu_{nI} dl_I (\phi_I - \phi_p) \tag{6 32}$$

To obtain an efflux from the control volume, a negative sign should appear in front of the flux term Thus, the final form of the source term b is given by,

$$b = -\Gamma_I dl_I (\frac{\partial \phi}{\partial n})_I + \varrho \mu_{nI} dl_I (\phi_I - \phi_p) + \bar{S} \tag{6 33}$$

6.2.6 Evaluation of the source term

For each of the equations, namely the continuity and momentum equations, the source term $\overline{S}$ assumes a different form. The pressure terms are included in this source term and its evaluation involves certain considerations which we now detail. For the u-momentum equation for example, we have

$$\overline{S}_u = \int_A - \left(\frac{\partial p}{\partial x}\right) dA \tag{6.34}$$

and for the v-momentum equation

$$\overline{S}_v = \int_A - \left(\frac{\partial p}{\partial y}\right) dA \tag{6.35}$$

Consider the term corresponding to the u-momentum equation as in Eq (6.34), in relation to the u-control volume shown in Fig 6.8(a) below. Applying the divergence theorem, Eq (6.34) can be written as

$$\overline{S}_u = - \sum_{k=1}^{5} p_f (dl_y)_k \tag{6.36}$$

where the length dl_y is the projected length of a side along the y-direction. Thus, for the control volume shown, the pressure contributions take the form,

$$\overline{S}_u = - p_e dl_e + p_w dl_w \pm p_f (dl)_y \tag{6.37}$$

Now, as shown in Fig. 6.8(b), $(dl)_y = dl_I \, n_x$, where n_x is the x-component of the unit normal vector to the interface in that cell, and is already available from the interface tracking information. From observing Fig. 6.7(b), it is evident that for $n_x < 0$ a negative sign is required in front of the pressure term for the interfacial segment and for $n_x > 0$, a positive sign is required. Thus, the appropriate form for the source term is now

$$\overline{S}_u = - p_e dl_e + p_w dl_w + p_f dl_I n_x \tag{6.38}$$

To estimate the value of pressure at the interface, p_I, a bilinear extrapolation is performed from the neighboring liquid phase pressure control points onto the interface location

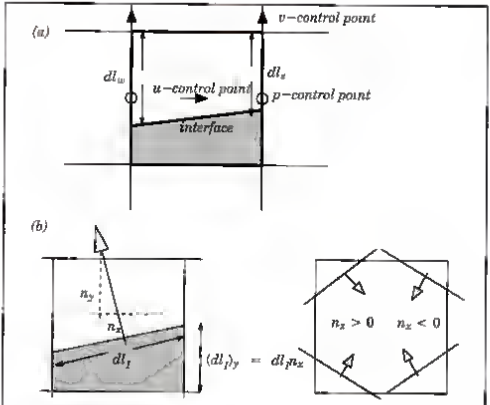

Fig 6 8 Schematic and geometric representation of cut cell (a) A typical control volume with an interfacial segment (b) Directions of normals and projected lengths for a typical control volume n_x and n_y are components of unit normal in the x and y directions

6.2.7 The continuity equation : pressure correction equation

The pressure correction equation is of the form shown in Eq (6 11) The right hand side contains mass fluxes through each side of the control volume. Such terms are easily evaluated, since the velocity values required in computing the mass fluxes are available at the cell faces, a feature of the staggered grid The coefficients for the pressure correction equation are assembled in the standard way (Patankar, 1979)

6.2.8. Dealing with cut cells

When the interface passes through the staggered grid arrangement as shown in Fig 6 3, the control volumes in the vicinity of the interface become fragmented Consider the control volume for the u velocity $u(i,j)$ as shown in Fig 6 9(a) The u control pount hes in the hquid phase here while a piece of the control volume shown shaded hes in the solid phase However, in Fig 6 9(b) the shaded regon belongs to cell $(i,j-1)$ but hes in the solid phase. Thus, one has to account for the existence of such pieces of control volumes and assign them to the proper phase. This is done by defining partner cells for each type of cell, a procedure discussed in more detail in Chapter 5 In Fig 6 9(a) for example the cell (i,j) is now redefined to be the unshaded irregular cell Smilarly, in Fig 6 9(b) the new u-cell (i,j) is defined by the shaded region. This procedure of redefining the cut cells and their partners is accomplished by running through the array of interfacial cells By assigning partner cell fluxes and redefining dimensions it is possible to maintain consistency at cell faces and conservation of fluxes

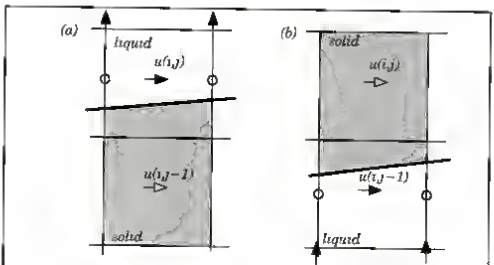

Fig 6 9 Definition of cut celle and their partners (a) Present cell ie in liquid phase (b) Present cell is in solid phase.

6.2.9 Conservation and consistency at cell faces

In solving the set of conservation laws, it is important to set up the control volume formulation and differencing schemes so that strict conservation of fluxes is maintained. Consider the situation shown in Fig. 6.10. Of concern to us are the flux evaluation through the faces of the cells (i,j) and (i ± 1, j) and their relation to the partner cell definitions. The newly redefined cells after partner cell assignment are as shown by the dotted lines. The fluxes through the west face of (i,j) are now magnified by the factor $(dl_{ij}(i,j) + (dy - dl_{ij}(i,j-1))) / dl_{ij}(i,j)$ to correct for the augmented length of the west face. A similar modification is made for cell (i−1, j) when its partner cell (i−1, j−1) is being dealt with. Similarly in cell (i,j−1) the pressure force on the west side is magnified by the factor above. fluxes from the interface computed in cell (i, j−1) are assigned to cell (i,j) and from cell (i−1,j−1) to cell (i−1,j). Thus, the partner assignment procedure and the cut cell coefficient assembly algorithms achieve explicit flux conservation in the cells affected by the interface.

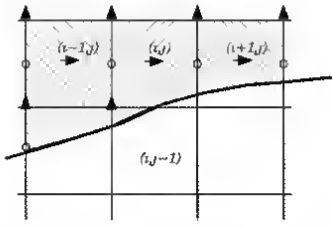

Fig. 6.10 Illustration of partner cell definitions.

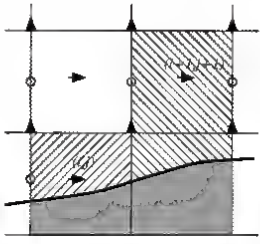

Fig 6 11 Illustration of an anomalous case in defining fluxes.

6.2.10 Anomalous cases

However, some anomalous situations may be encountered in the coefficient assembly process. For instance, in Fig. 6.11, the u-control point (i,j) is adjoined by a solid phase control point. Therefore the flux through the east face is not straightforward to compute. The way this is done to maintain consistency at that face is by noting that cell $(i+1,j+1)$ has been redefined by the partner cell assignment procedure to be of the shape shown. Thus, a part of the west face of cell $(i+1,j+1)$ is now adjecent to the east face of cell (i,j). Therefore the flux through the west face of cell $(i+1,j+1)$ has to be consistent with the fluxes through the east faces of (i,j) and $(i,j+1)$. The flux through the east face of cell (i,j) is now obtained by redistributing the west face flux of cell $(i+1,j+1)$, weighted according to the dimensions $dl_e(i,j)$ and $dl_e(i,j+1)$. In addition, if the east face pressure control point of cell (i,j) is also in the solid phase, the pressure contribution from cell $(i+1,j+1)$ is redistributed consistently between cells $(i,j+1)$ and (i,j). Such anomalous cases exist for all eight types of cells and for all control volumes. Treating such cases adds to the tedium of assembly of the coefficients but is critical in obtaining

solutions to flow problems If consistency at cell faces is violated, convergence cannot be achieved due to the existence of the spurious sources/sinks of mass, momentum and energy at such locations

6.2.11 Distinction between liquid and solid cells

In the cell assembly procedure, one has to be careful not to step across the interface into the opposite phase in performing the flux computations The advantage in combining the Eulerian (field solver) and Lagrangian (interface tracking) methods here is that the two phases can be treated separately Thus, unlike in the Eulerian methods, the interface separating the two phases can be explicitly defined and treated as a discontinuity And, in contrast with the Lagrangian methods, grid redistribution for conformity with the moving, distorting boundary is avoided Thus, in each phase, the operations involved in obtaining the flux estimates should involve points in the same phase and the interfacial values only The treatment of the liquid and solid phase control points follows the same procedure as far as the coefficient assembly is concerned However, the solid is passive as far as fluid flow goes, unlike in the purely Eulerian methods where it is assumed to have some porosity in the proximity of the interface to ease the sudden property jump across it In our case, once the coefficients are assembled, a flag denoting solid is employed to turn off the fluid flow computations in the solid phase, such that $a_P = 1$ and a_E, a_W, a_N, a_S , $b = 0$ in the solid, which results in $u = v = p' = 0$ in the solid phase Thus of course is not applicable for the energy equation where heat conduction in the solid is to be accounted for

6.2.12 Moving boundary problems – treatment of cells that change phase

When the interface moves, say due to change of phase, the shape of the interface at two time instants (or iterations) may develop as shown in Fig 6 12 Thus cells (i,j), $(i+1,j)$ etc have moved from solid phase into the liquid In the implicit solution procedure adopted here, information regarding the previous state

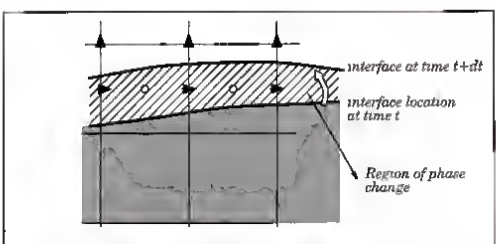

Fig 6 12 Change of phase of cells as the interface traverses the domain

of a control point is required to evaluate the time derivative, i e , the quantity $\phi^n_{i,j}$ corresponding to the new phase is non-existent for that control point To overcome this difficulty, flags are employed indicating the current and previous phases of the control point. When a control point changes phase, the value at that location corresponding to the phase in which it finds itself is estimated by performing a linear interpolation as shown in Fig. 6 13 The new value in a cell which undergoes phase change is thus obtained by interpolation from neighboring cells in the same phase as

$$\phi^n_{i,j} = (dy_j\phi^n_{i,j+1} + dy_N\phi^n_j)/(dy_j + dy_N) \qquad (6\ 39)$$

In particular the value $\phi^n_{i,j}$ is then obtained via the implicit solution procedure by iteration In our computations, flipping of a control point between two phases was practically non-existent This problem exists in purely Eulerian methods In our case, since the interface is a continuous entity each point on the interface is influenced by the motion of all its neighbors along the interfacial curve and this global influence helps in avoiding flipping of phase. The interface reconstruction procedures rely on local fluid fraction information in a cell to define the interface

and thus it is possible for a cell to flip between phases in the course of the iterations.

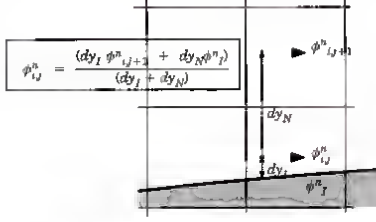

Fig 6.13 Illustration of interpolation procedure for the estimation of field quantities in cells that heve changed phase.

6.3. Results and discussion

We first compare solutions for a stationary interface with those from well-tested solution procedures using body-fitted coordinates (Shyy, 1987). This exercise is designed to validate the conservation and consistency characteristics of the cut cell method. The interface is sufficiently deformed that all the types of cut cells are encountered. In the absence of a consistent discretization in the vicinity of the interface, it is found that convergence cannot be achieved, and that care needs to be exercised in performing flux calculations in the grid cells affected by the interface. The computational domain is as shown in Fig. 6.14(a). The square cavity is a frequently adopted test bed for numerical experiments for incompressible flows and benchmarks exist. We deform the base of the cavity, the amplitude being 10 per cent of the base. A 121x121 Cartesian grid is employed. We first present the results for a driven cavity flow, where the top wall of the cavity is pulled at ve-

locity $U = 1$ corresponding to a Reynolds number of 1000 The results from the present method is compared with a previously benchmarked body fitted formulation with the same grid size. The results are shown in Fig 6 15 The streamline

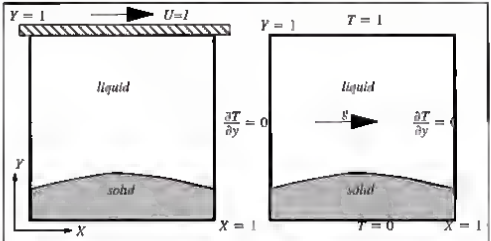

Fig 6 14 Illustration of computational domain and boundary conditions for the test cases presented. For both configurations, no−slip conditions are applies on all solid surfaces A Cartesian grid is used, with the interface passing through the grid The interface amplitude was equal to 0 1, which is 10% of the domain size (a) Domain and boundary conditions for driven cavity flow (b) For natural convection

patterns in Fig 6 15(a) and (b) show good agreement A quantitative comparison can be seen in Fig 6 15(c) and (d) where the centerline velocities are plotted

In Fig 6 16 we compare the results for a stationary interface with natural convection in the cavity shown in Fig 6 14 (b) The same grid size and interface shape as above is used The Rayleigh number computed is 10^5 and $Pr = 1$ Again the streamline patterns shown in Fig 6 16 (a) and (b) are in good agreement In Fig 6 16(e), (f), (g) we compare the centerline values of u, v components of velocity and temperature respectively along the centerline of the cavity The results agree closely with the body-fitted code Thus, it has been shown that the current scheme

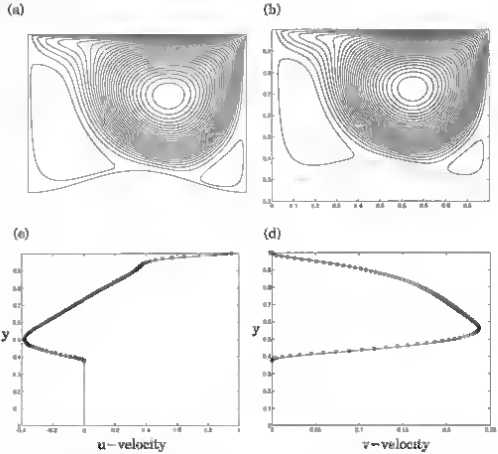

Fig 6 15 Streamlines for the case of a driven cavity with a deformed base Re=1000, 121X121 grid (a) Contours from a boundary−fitted grid computation (b) On a fixed Cartesian grid using the current method Comparison of solutions from the boundary−fitted and current Cartesian grid method (c) Centerline u−velocity. Dots represent solution from boundary−fitted grid Full lines from current calculation (d) centerline v−velocity

yields accurate results for the case of a stationary interface, in the presence of complex flowfields It is noted here that the formulation developed here would be useful in computing incompressible flows around complex shapes employing fixed Cartesian grids, circumventing the need for generation of boundary-fitted grids

We now proceed to test the numerical procedure developed here for a situation involving phase change Hitherto much effort has been devoted to numerical-

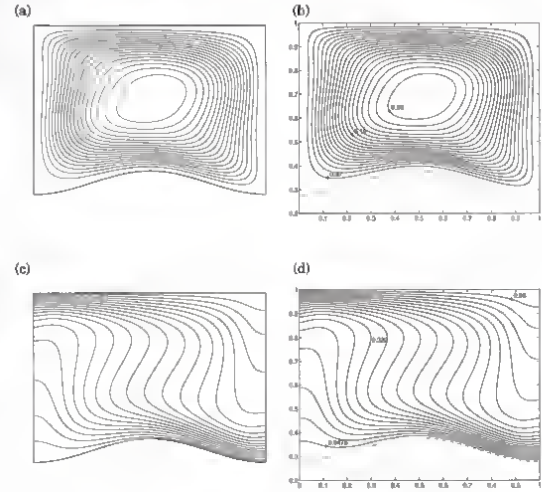

Fig 6 16 Streamlines for natural convection in a deformed cavity $Re=10^5$, $Pr=1$, 121X121 grid. (a) Result from boundary−fitted grid computations
(b) Results from Cartesian grid computations
(c) Temperature contours from the boundary−fitted formulation
(d) Temperature contours from the Cartesian grid computations

ly duplicating the results of Gau and Viskanta (1986) (hereafter referred to as G&V) for the melting of Gallium from a vertical wall in a rectangular enclosure. Gallium is adopted as the experimental material since it is a metal with low melting point and thus is easy to handle. Unfortunately numerical values of interface positions were not presented in G&V and the initial conditions are ambiguous The authors also present interface shapes viewed from the front and rear of their

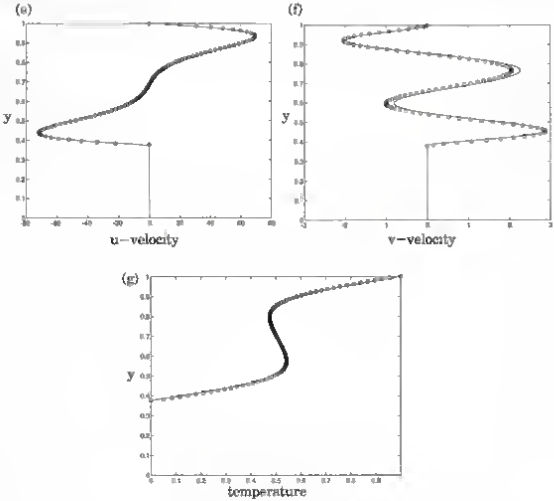

Fig 6 16 −− continued (e) Centerline u−velocity Dots are from the boundary−fitted grid computations Full lines are from the current method. (f) Centerline v−velocity comparison (g) Centerline temperatures

experimental set-up, and poor correspondence is observed Furthermore, recent experiments of Campbell et al (1994) appear to differ from G&V in regard to interface shapes and positions Underlying these facts is the difficulty in performing experiments in relation to flowfields and interface positions in opaque melts Despite these limitations, the experiments of G&V have been extensively employed for comparison Needless to say, the agreement between the numerics and experiment is at best modest (Lacroix, 1989, Lacroix and Voller, 1989) A more effective

comparison may be between numerical techniques of essentially disparate nature, for instance purely Lagrangian and Eulerian methods. Lacroix and Voller (1989) have performed such a comparison. The grid sizes used by these authors, however may not be sufficiently fine to resolve all the flow features. In our work, we found the presence of multiple convection cells in the initial stages of development of the interface in some cases. It is not conceivable that such cells can be resolved by coarse grids. The presence of such cells is important to capture, in particular because the interface shape reflects the presence of these flow features. Thus, two different numerical schemes can yield results in good agreement for the same grid spacing, but neither may actually be an accurate calculation. In fact, the level of numerical dissipation, i.e., the order of accuracy of the numerical technique was found to determine the types of flow features resolvable, especially at higher Rayleigh numbers. Thus, the entire situation, especially for the higher Rayleigh numbers, is found to be highly sensitive to the numerical conditions employed. Since the interface shape is strongly linked to the flow features and *vice versa*, great care must be employed in performing the computations.

Here we present calculations for the melting of Gallium from a vertical wall for the configuration shown in Figure 6.17. The current method is compared with an enthalpy-based Eulerian method (Shyy and Rao, 1993) employing an 81x81 grid. Unless otherwise mentioned the second-order central difference scheme is used for both the methods. In a method dealing with the temperature as a variable and using an interface tracking procedure, it is not possible to initiate melting in a domain that is entirely solid. Thus, the computations using the present method are started from an initial condition generated by the enthalpy method, so that an thin initial melt layer exists at the start. The flowfield and temperature field are obtained from the purely Eulerian method. Melting is initiated at the left wall. In Fig. 6.18 we show the results for a Rayleigh number of 10^4. The Prandtl num-

ber of Gallium is 0 021 The Stefan number for this case is 0 042 The interfacial shape and position are compared in this case with that of the enthalpy-based method in Fig 6 18(a) As can be seen close agreement is maintained between the predictions of the two methods The present interface tracking method is marginally slower than the purely Eulerian method for large times However, it is likely that with further refinement of the grid better agreement can be obtained. It may be noted that the location of the elbow in the phase front is correctly predicted, and thus the size of the recirculation zone is obtained accurately This can be seen from the plots of the streamlines at two different time instants, shown in Fig 6 18 (e–f) Furthermore the centerline velocities and temperature profiles, shown in Fig 6 18(b) are in good agreement Thus this experiment has proven that the methods employed in treating the interface, in particular the flux computations for the cut cells, the treatment of pressure terms, and the procedures involved with the newly formed cells are borne out by these calculations

We next present, in Fig 6 19 the results for a higher Stefan number In this case, as above $Ra = 10^4$, $Pr = 0.021$, but Stefan number $St = 0.42$, a ten-fold increase In Fig 6 19(a) the interface positions are compared, plotted at equal intervals of time $\delta t^* = 10$ As can be seen the results are very close except for the lagging of the current method for larger times But even for the rapidly moving interface, the front shapes are well predicted, which implies that the bulk flow, i e., recirculation zones are obtained accurately In the figures containing contours of stream function and isotherm contours, Fig 6 19 (c–h), the interface has been represented in each case by plotting the temperature contours $T = -0.005$, 0 0 and 0 005 In the case of the enthalpy method this is the best approximation to the interface shape that one can obtain In fact, in the comparisons of the interface shapes, the values corresponding to the enthalpy method are obtained as that corresponding to the $f_s = 0.5$ contour by interpolation Thus there is an uncertainty

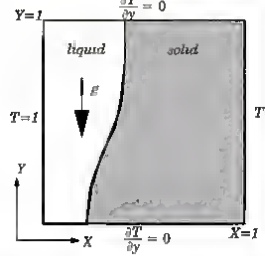

Fig 6.17 Illustration of computational domain and boundary conditions for the melting of Gallium The melting is initiated at the left wall No−slip velocity conditions are imposed on all solid surfaces Computations are performed on a Cartesian grid

of the order of the grid spacing in identifying the interface position in the enthalpy method In contrast the interface tracking procedure explicitly yields information regarding interface shape Also, it is noted that in the interface tracking method, no modelling of physics is necessary in the vicinity of the interface, while in the enthalpy method, there is an unavoidable smearing of information In addition the D'Arcy law treatment and the mushy zone model (Voller and Prakash, 1987) obscure the transport processes in this region.

6.4. Summary

A numerical solution technique has been developed to combine the strengths of the purely Eulerian and Lagrangian methods This has resulted in a method that has the following features:

1 Highly distorted interfaces can be handled by the Lagrangian component, namely the interface tracking scheme. In the previous chapter we have demon

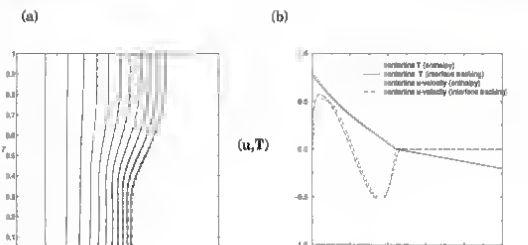

Fig. 6.16 Melting of Gallium, Ra=10^4, Pr=0.021, St=0.042, 81x81 grid. Melting is initiated at the left.
(a) Comparison of interface positions at equal intervals of time. Dotted lines represent the enthalpy–based method, full lines correspond to the present method.
(b) Comparison of centerline profiles. Legends are self–explanatory.

strated the ability of the scheme to capture the interactions, i.e. merger and break-up of different shapes and their subsequent evolution. The methods that were developed to handle diffusion-controlled instability phenomena have here been extended to incorporate convection effects.

2. The computations are performed on a fixed Cartesian grid. Thus, the problems associated with grid redistribution associated with body-fitted adaptive grids is avoided. Also the procedures employed in the discretization of the equations on such a grid lend themselves to the use of well-tested implicit pressure-based flow solvers. The solutions are achieved by discretizing the equations via a control volume formulation, with particular attention toward conservation and consistency in assembling the fluxes of conserved variables. The solution is achieved by using

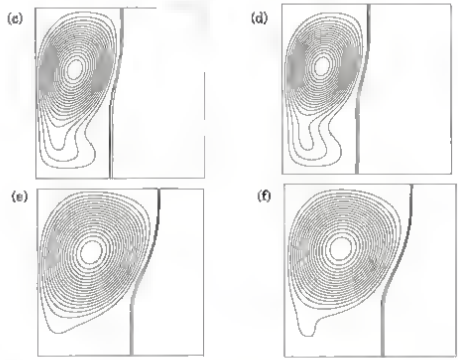

Fig. 8.18 -- continued. Streamline contours at t=50 and t=100. Comparison of the enthalpy and present methods. (c) Current interface tracking method, t=50. (d) Enthalpy method, t=50. (e) Current method, t=100. (f) Enthalpy method, t=100. The interface has been represented by plotting the temperature contours between T=−0.005 and 0.005. In the case of the current method, the interface position is actually available explicitly and exactly. In the enthalpy method, the only information regarding the interface is the contours shown.

the line SOR method, leading to the iterative solution of tri-diagonal matrices 3. The interface definition is strictly maintained and the boundary conditions applied on the control volumes. The release of latent heat during phase change has been incorporated via the Stefan condition. Several details involved in dealing with the presence of the interface have been presented. Some procedures have been devised in dealing with the flux of quantities at the interface.

The results presented here demonstrate the accuracy of the computational procedure by comparing with previously tested methods. Thus, at this stage we

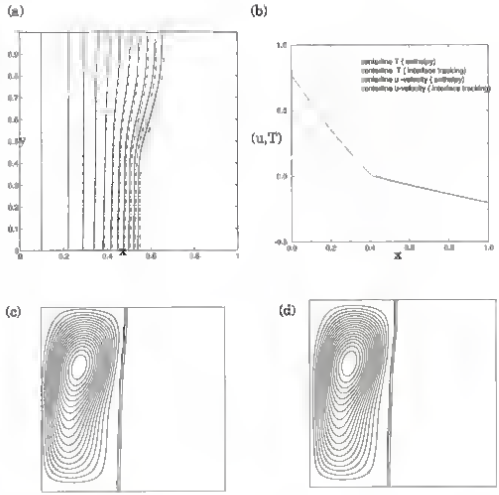

Fig 6 19 Melting of Gallium Comparison of solutions from an enthalpy method and the present interface tracking method Higher Stefan number case $Re=10^4$, Pr= 0 021, St=0 42, 81x81 grid. (a) Comparison of interface shapes at equal intervals of time Full lines belong to the present method Dashes represent enthalpy method (b) Comparison of centerline values The legend is self–explanatory (c) Streamline contours for the current method at t=50 (d) Streamline contours for enthalpy method at t=100 In (c) and (d), the interface is represented by plotting the temperature contours T= −0 005, 0 0 and 0 005

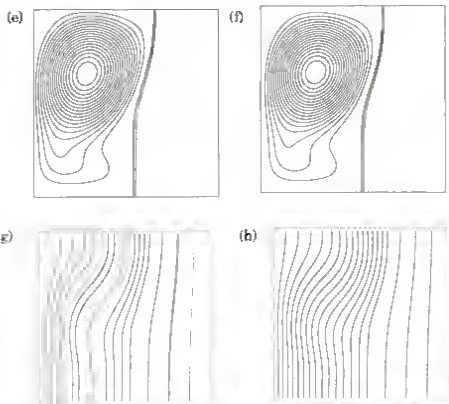

Fig. 6.19 – – continued (e) Streamline contour at t=100, for the interface tracking method (f) Streamline contour at t=100, enthalpy method (g) Temperature contour at t=100, interface tracking method (h) Temperature contour, t=100, enthalpy method

have a computational procedure that can handle the evolution of highly distorted fronts At the micro-scale level, at which diffusion processes dominate the method can handle complex geometries and physics At the macroscopic level the flow features obtained are in agreement with the solutions from body-fitted techniques for deformed boundaries Further extension of the work presented here is required to combine all the capabilities demonstrated here to incorporate the entire range of phenomena encountered in the solidification process The primary extensions are outlined in the next chapter

CHAPTER 7

SUMMARY AND SUGGESTIONS FOR FUTURE WORK

A method for the computation of transport processes in the presence of deformed, moving boundaries has been developed. The work presented here is the framework for a more robust and flexible solution technique that can handle complex situations involving many interacting interfaces. It has only been possible in the scope of this dissertation to address some of the fundamental issues involved in tracking the evolution of internal boundaries of arbitrary shape on fixed Cartesian grids. The physical phenomenon that has motivated this effort is the morphological instability of solidification fronts. This problem presents many challenges to a numerical simulation procedure designed to capture all the events involved in the solidification from melts. Highly distorted interfaces arise, which may subsequently undergo changes in topology. The interfacial phenomena are significantly influenced by interfacial features such as slopes and curvatures. In addition, transport phenomena in each phase are coupled to the motion of the interface.

The final solidified product in any processing arrangement is dependent on the macroscopic as well as microscopic physical mechanisms. Convective effects are important at the macroscopic scales of the phenomenon, while capillary forces are critical at the microscopic scale. The growth environment impacts on the microstructure. In turn, the microstructure determines the solid fractions and transport phenomena close to the phase front. Neither of these aspects has been clarified to a desirable extent. Less is established regarding the interaction of scales.

An attempt has been made herein to unify the behavior of the phenomena at the different scales In performing computations, the effects of one scale on another enters via the control parameters and non-dimensional quantities in the governing equations as well as the boundary conditions on the computational domain and the interface. The complexity of the phenomenon and the many issues involved in the matching procedure are brought to light. There are several directions in which the scaling analysis must be extended and these are detailed later.

In dealing with the simulation of the interfacial evolution the following steps were adopted

1 After it was clear from a preliminary effort at employing boundary-fitted coordinates that such a framework would encounter serious difficulties in the advanced stages of the instability, a new approach was deemed necessary With this in view, an interface tracking algorithm was developed with the aid of an imposed velocity field modelled to induce highly deformed boundaries and topological changes. Markers and cells were used to perform the tracking of the fronts An intersection procedure was devised to prevent particle depletion/accumulation and to retain the resolution consistent with that of the grid Several details involved in executing mergers and breakups of several interfaces were tackled. These two measures have surmounted problems usually associated with a purely Lagrangian procedure

2. As a next step, the interface tracking algorithm was incorporated in a field equation solver where pure conduction heat transport in each phase was computed This yields the value of interfacial velocity The key issue that arises when an interface of arbitrary shape passes through a Cartesian grid is the problem of dealing with the irregularly shaped control volumes. Such cut cells have been tackled and the fluxes through them evaluated based on a control volume for-

mulation Care has been taken to assign fluxes such that conservation and consistency are maintained In addition many procedures had to be developed to deal with the communication between field equation solver and interface tracking modules

3 Based on the flux evaluation techniques and other methods in the pure conduction case an extension to the full Navier-Stokes solver was made The solver now has the ability to compute flows at the macroscopic levels, i.e. convection dominated flows A pressure-based implicit solver is used. The interaction of the flow with the interface has been dealt with and fluid flow variables thereupon computed, keeping in mind the need for conservation to be honored.

The procedures developed here form the framework for computing incompressible flows with arbitrarily shaped, moving boundaries Several tests and feasibility studies have been performed. However, the scope of the numerical technique has not been fully exploited at this stage Extensions of the following types are envisaged.

1. Grid refinement. When the interface increases in perimeter and assumes convoluted shapes, the curvatures in regions of large deformations may increase. Furthermore the solid phase may begin to occupy a larger portion of the computational domain The current fixed grid technique then encounters two difficulties. Firstly, there may be insufficient resolution in the regions of high interfacial curvature. Secondly, the grid distribution may not be sufficient in regions where the transport processes may demand higher resolution, such as in the vicinity of the interface. Thus, restriction to a fixed Cartesian grid, while carrying with it an inherent simplicity, may be somewhat inflexible There are ways of overcoming this difficulty One can employ a local refinement technique in the required regions For example, a multi-block grid refinement can be performed This will permit retaining the line SOR technique along with the time-implicit formulation Since

the interface moves and deforms, with time the regions demanding resolution will change Thus, the multiblock grid layout will have to adapt to this changing need by a process of block addition or elimination or by reconfiguring the blocks in the interfacial regions Such treatments may impose considerable logical burdens on the tracking and field solver components In the context of discontinuities in compressible flows, such a methodology is extant (Berger and Colella, 1989) Multiblock methods for the framework developed for the flow solver in the present work can be developed following Wright and Shyy (1992) for incompressible flows

Local refinement by grid cell division can also be performed but this will entail adopting an explicit time-stepping formulation, which will call for revamping the current solution technique Another strategy would be to use a curvilinear adaptive grid instead of the fixed Cartesian grids used in this work, while retaining the independence of grid motion from that of the interface This measure is likely to add significantly to the complexity of the logic involved in tracking the interface and is unlikely to provide much benefit in terms of resolution when the interface becomes highly deformed

2 Inclusion of solute field The computations here have been performed for pure materials The addition of a solute field is necessary, since many technologically important solidification processes involve additives or solutes. The presence of the solute composition variable adds to the complexity of the problem by impacting on the instability mechanisms, and bringing in double-diffusive transport effects In the numerical method developed here it should be straightforward to include the composition field as well as the interfacial boundary conditions under impurity-controlled growth However, more than in the pure material case the scaling issue here is complicated An additional non-dimensional number (Schmidt number $=\nu_l / D_l$, i.e., the ratio of momentum and mass diffusivities)

is involved Also new microscopic as well as macroscopic behavior can arise and the communication between the scales have to be re-examined

3 Matching of macro and micro fields . For the pure material case, a method to relate macroscopic to microscopic conditions has been devised Thus, a scaled form of the microscopic equations has been obtained The inverse problem, i e quantifying the effects of microstructures on the macroscopic transport properties needs to be addressed This task will involve averaging and statistical procedures With the addition of solute the situation will become more involved The microstructure information defines the nature and extent of the mushy zone in the enthalpy based formulations, which are popular for the simulation of the macroscopic flow features. In other formulations, some means of conveying the interfacial structure to the global flowfield has to be devised Establishing such a communication between scales is important for the simulations to have any impact on practical solidification arrangements

4 Changes in topology . Only single interfaces, in conjunction with the field solver are dealt with in this work The extension to incorporate competition effects or interactions of multiple interfaces will need the aid of grid refinement. In principle, it is possible to track the mergers and breakups of interfaces. When such events occur the physics involved are not well understood and thus some ambiguity in treating such highly non-equilibrium events will be inevitable However, with a suitably refined Cartesian grid it would be possible for the interface tracking procedure to handle topological changes.

5 Other phenomena with interfaces . While the present method has been applied to the solidification problem it would be possible to apply the same techniques to other physical phenomena involving interfaces Apart from the fact that the flow

solver is currently restricted to incompressible flow, there are no inherent specializations to the solidification problem

It is the goal of the author to incorporate these extensions and test the computational scheme presented in this work for problems of greater complexity. It is hoped that further development along the lines of the framework laid out here will lead to a robust, powerful and economical solver for fluid flow configurations involving moving, deformed boundaries including phase transformations

REFERENCES

Ananth, R. and Gill, W N 1989 Dendritic growth of an elliptic paraboloid with forced convection in the melt, *J Fluid Mech.*, Vol 208, pp 575–593

Ananth, R. and Gill, W N. 1991 Self-consistent theory of dendritic growth with convection, *J Crystal Growth*, Vol 108, pp 173–189

Ashgriz, N and Poo, J Y. 1991 FLAIR–Flux Line-Segment Model for Advection and Interface Reconstruction, *J Comp Phys.*, Vol 93, pp 449–468

Aref, H and Tryggvasson, G 1984 Vortex dynamics for passive and active interfaces, *Physica 12D*, pp 59–70

Bayyuk, S A., Powell, K.G and van Leer, B 1993 A simulation technique for 2-dimensional unsteady inviscid flows around arbitrarily moving and deforming bodies of arbitrary geometry, *AIAA Paper No 93–3391*

Beckermann, C , Feller, R. J , Irwin, T.R., Muller-Spath, H and Wang, C Y. 1994 Visualization of sedimentation and thermosolutal convection during equiaxed alloy solidification, *AIAA Paper No 94–0570*

Beckermann, C and Viskanta, R 1993 Mathematical modeling of transport phenomens during alloy solidification, *Appl Mech Rev* , Vol 46, pp 1–27

Bejan, A. 1984 *Convection Heat Transfer*, Wiley, New York.

Ben-Jacob, E., Godbey, R , Goldenfeld, N D , Koplik, J , Levine, H , Mueller, T. and Sander L M 1985 Experimental demonstration of the role of anisotropy in interfacial pattern formation, *Phys Rev. Lett* , Vol 55, pp 1315–1318

Bensimon D 1986 Stability of viscous fingering *Phys Rev A*, Vol 33, pp 1302–1308

Bensimon, D and Pelce, P 1986 Tip–splitting solutions to the Stefan problem, *Phys. Rev* , Vol A 33, pp 4477–4478

Berger, M J and Colella, P 1989 Local adaptive mesh refinement for shock hydrodynamics, *J Comp Phys* , Vol 82, pp 64–84

Borisov, A. G , Fedorov, O P and Maslov, V V 1991 Growth of Succinonitrile dendrites in different crystallographic directions, *J Crystal Growth*, Vol 112, pp 463–466

Boussou, Ph , Perrin, B and Tabeling, P 1990 Influence of an external periodic flow on dendritic crystal growth In *Nonlinear Evolution of Spatio-temporal Structures in Dissipative Dynamical Systems*, Eds F H Busse and L Kramer, Plenum Press, New York

Brackbill, J U , Kothe D B and Zemach, C 1992 A continuum method for modeling surface tension, *J Comp Phys*, Vol 100, pp 335–354

Brattkus, K 1989 Capillary instabilities in deep cells during directional solidification, *J Phys France*, Vol 50, pp 2999–3006

Brenner, E A 1991 Pattern selection in two-dimensional dendritic growth, *Advances in Phys* , Vol 40, No 1, pp 53–97

Brower, R , Kessler, D , Koplik, J and Levine, H 1983 Geometric approach to moving interface dynamics, *Phys Rev Lett* , Vol 51, pp 1111–1114

Brown, R A 1988 Theory of transport processes in single crystal growth from the melt, *A I Ch E J*, Vol 34, pp 881–911

Brush, L N and Sekerka,R F 1989 A numerical study of a two-dimensional crystal growth forms in the presence of anisotropic growth kinetics, *J Crystal Growth*, Vol 96, pp 419–441

Cahn, J W and Hilliard, J E 1958 Free energy of a nonuniform system, I Interfacial free energy, *J Chem Phys* , Vol 28, No 2, pp 258–267

Camel, D , and Favier, J J 1986 Scaling analysis of convective solute transport and separation in Bridgeman crystal growth from the doped melt, *J de Physique*, Vol 47, pp 1001–1014

Campbell, T A , Pool, R E and Koster, J N 1994 Melting and solidification of a liquid metal at a vertical wall, *AIAA Paper No 94–0792*

Canright, D and Davis, S H 1991 Buoyancy effects of a growing, isolated dendrite, *J Crystal Growth*, Vol 114, pp 173–189

Carey, V P 1992 *Liquid Vapor Phase Change Phenomena*, Series in Chemical and Mechanical Engineering, Hemisphere Publishing, Washington DC

Chern, I -L , Glimm, J , McBryan, O , Plohr, B and Yaniv, S 1986 Front tracking for gas dynamics, *J Comp Phys* , Vol 62, pp 83–110

Chorin A J 1985 Curvature and solidification, *J Comp Phys* , Vol. 58, pp 472–490

Cladis, P E., Finn, P L. and Gleeson, J T 1990 Routes to cell formation and hidden ramps in directional solidification, in *Nonlinear Evolution of Spatio-Temporal Structures in Dissipative Continuous Systems*, Ed Busse, F H and Kramer, L , Plenum Press, New York

Couder, Y., Gerard, N and Rabaud, M 1986 Narrow fingers in the Saffman-Taylor instability, *Phys Rev A* Vol 34, No 6, pp 5175–5178.

Crank, J 1984 *Free and Moving Boundary Problems*, Oxford University Press, Oxford, UK.

Cross, M C and Hohenberg, P C 1993 Pattern formation outside of equilibrium, *Rev Mod Phys.*, Vol 65, No 3.

Daly, B J 1967 Numerical study of two-fluid Rayleigh Taylor instability, *Phys Fluids*, Vol 10 pp 297–307.

Daly, B J 1969 A technique for including surface tension in hydrodynamic calculations, *J Comp Phys*, Vol 4

Dantzig, J A 1989 Modelling liquid-solid phase change with melt convection, *Int J Numer Meth Engng*, Vol 28, pp 1769–1785.

Davis, S H. 1990 Hydrodynamic interactions in directional solidification, *J Fluid Mech.*, Vol 212, pp. 241–262.

Davis, S. H., Muller, U. and Dietsche, C 1984 Pattern selection in single-component systems coupling Benard convection and solidification, *J Fluid Mech.*, Vol. 144, pp. 133–151.

de Cheveigne, S , Fauvre, G , Guthmann, C and Kurowski, P 1990 Directional solidification of transparent eutectic alloys in *Nonlinear Evolution of Spatiotemporal Structures in Dissipative Continuous Systems*, Ed Busse, F H and Kramer, L , Plenum Press, New York

DeGregoria, A J and Schwartz, L W 1985 Finger breakup in Hele-Shaw cells, *Phys Fluids*, Vol 28, No 9, pp 2313–2314

DeGregoria, A J and Schwartz, L W 1986 A boundary integral method for two-phase displacement in Hele-Shaw cells, *J Fluid Mech* , Vol 164, pp 383–400.

Dienstfrey 1985 Noise sustained structure, intermittency and the Ginzburg-Landau equation, *J Stat Phys.*, Vol 40, pp 371–395.

Dougherty, A , Kaplan, P D and Gollub, J P 1987 Development of sidebranching in dendritic crystal growth, *Phys Rev Lett.*, Vol 58, pp. 1652–1655.

Drazin, P G and Reed, H W 1981 *Hydrodynamic Stability*, Cambridge University Press, Cambridge, UK.

Emerton, N E 1984 *The Scientific Reinterpretation of Form*, Cornell University Press, Ithaca.

Fabietti, L M , Seetharaman, V and Trivedi, R. 1990 The development of solidification microstructures in the presence of lateral constraints, *Metall Trans A*, Vol 21A, pp. 1299–1310

Fang, R. T , Glicksman, M E , Coriell, S R., McFadden, G B and Bouvert, R. F 1985 Convective influence on the stability of a cylindrical solid-liquid interface, *J Fluid Mech* , Vol 202, pp 339–366, 1985

Fauci, L. J. and Peskin, C. S. 1988. A computational model of aquatic animal locomotion, *J. Comp. Phys.*, Vol. 77, pp. 85–108.

Favier, J. J., 1990. Recent advances in Bridgeman growth modeling and fluid flow, *J. Crystal Growth*, Vol. 99, pp. 18–29.

Favier, J. J. and Rouzaud, A. 1983. Morphological stability of the solidification interface under convective conditions, *J. Crystal Growth*, Vol. 64, pp. 387–379.

Flemings, M. C. 1974. *Solidification Processing*, McGraw–Hill, New York.

Flesselles, J.–M., Simon, A. J. and Libchaber, A. J. 1991. Dynamics of one-dimensional interfaces: an experimentalist's view, *Adv. Phys.*, Vol. 40, No. 1, pp. 1–51.

Floryan, J. M. and Rasmussen, H. 1989. Numerical methods for viscous flows with moving boundaries, *Appl. Mech. Rev.*, Vol. 42, No. 12, pp. 323–341.

Forth, S. A. and Wheeler, A. A. 1989. Hydrodynamic and morphological stability of the unidirectional solidification of a freezing binary alloy: A simple model, *J. Fluid Mech.*, Vol. 202, pp. 339–366.

Forth, S. A. and Wheeler, A. A. 1992. Coupled convective and morphological instability in a simple model of a freezing binary alloy including a shear flow, *J. Fluid Mech.*, Vol. 236, pp. 61–94, 1992.

Fromm, J. 1981. Finite difference computation of the capillary jet, free surface problem, in *Lecture Notes in Physics*, Vol. 238, Springer Verlag, New York, pp. 188–193, 1981.

Garandet, J. P., Duffar, T. and Favier, J. J. 1990. On the scaling analysis of the solute boundary layer in an idealized growth configuration, *J. Crystal Growth*, Vol. 106, pp. 437–444.

Gau, G. and Viskanta, R. 1986. Melting and solidification of a pure metal on a vertical wall, *Trans. ASME*, Vol. 108, pp. 174–181.

Glicksman, M. E., Cornell, S. R. and McFadden, G. B. 1986. Interaction of flows with the crystal-melt interface, *Ann. Rev. Fluid Mech.*, Vol. 18, pp. 307–336.

Glicksman, M. E., Schaefer, R. J. and Ayers, J. D. 1976. Dendritic growth– a test of theory, *Metall. Trans. A*, Vol. 7A, pp. 1747–1759.

Glimm, J., Grove, J., Lindquist, B., McBryan, O. A., Tryggvason, G. 1988. The bifurcation of tracked scalar waves, *SIAM J. Sci. Stat. Comput.*, Vol. 9, No. 1, pp. 61–79.

Glimm, J., McBryan, O., Melnikoff, R. and Sharp, D. H. 1986. Front tracking applied to Rayleigh Taylor instability, *SIAM J. Sci. Stat. Comput.*, Vol. 7, No. 1, pp. 230–251.

Herring, C. 1951 Surface tension as a motivation for sintering, in *Physics of Powder Metallurgy*, Edited by W. E. Kingston, pp 143–179, McGraw Hill, New York

Hirt, C. W. and Nichols, B. D. 1981 Volume of Fluid (VOF) method for the dynamics of free boundaries, *J. Comp. Phys*, Vol. 39, pp. 201–225

Homsy, G. M. 1987 Viscous fingering in porous media, *Ann. Rev. Fluid Mech.*, Vol. 19, pp. 271–312

Howison, S. D., Ockendon, J. R., and Lacey, A.A. 1985 Singularity development in moving-boundary problems, *Q. Jl. Mech. Appl. Math.* Vol. 38, pp. 343–360

Huang, S.-C. and Glicksmann, M. E. 1981 Fundamentals of dendritic solidification – I. Steady state tip growth, *Acta Metall.*, Vol. 29, pp. 701–715. Fundamentals of dendritic solidification –II. Development of sidebranch structure, *Acta Metall.* Vol. 29, pp. 717–734

Huerre, P. 1987 Spatio-temporal instabilities in closed and open shear flows. in *Instabilities and Nonequilibrium Structures*, Eds. E. Tirapegui and D. Villaroel, pp. 141–177, Dodrecht, Reidel, Germany

Ivantsov, G. P. 1947 Temperature field around spheroidal, cylindrical and circular crystal growing in a supercooled melt, *Dokl. Akad. Nauk.*, Vol. 58, pp. 567–569

Kessler, D. A., Koplik, J. and Levine, H. 1988 Pattern selection in fingered growth phenomena, *Advances in Physics*, Vol. 37, No. 3, pp. 255–339

Kobayashi, R. 1993 Modelling and numerical simulations of dendritic crystal growth, *Physica D*, Vol. 63, pp. 410–423

Kothe, D. B. and Mjolsness, R. C. 1992 RIPPLE: A new method for incompressible flows with free surfaces, *AIAA J.*, Vol. 30, No. 11, pp. 2694–2700

Kurowski, P., de Chevegne, S., Fauvre, G. and Guthman, C. 1989 Cusp instability in cellular growth, *J. Phys. France*, Vol. 50, pp. 3007–3019

Kurz, W. and Trivedi, R. 1992 Microstructure and phase selection in laser treatment of meterials, *Trans. ASME*. Vol. 114, pp. 450–458

Lacroix, M. 1989 Computation of heat transfer during melting of a pure substance from an isothermal wall, *Numer. Heat Transfer*, Part B, Vol. 15, pp. 191–210

Lacroix, M. and Voller, V. R. 1990 Finite difference solutions of solidification phase change problems: transformed versus fixed grids, *Numer. Heat Transf., Part B*, Vol. 17, pp. 25–41

Langer, J. S. 1981 Instabilities and pattern formation in crystal growth, *Rev. Mod. Phys.*, Vol. 52, No. 1, pp. 1–56

Langer, J S., and Muller-Krumbhaar 1578 Theory of dendritic growth, Parts I, II, and III, *Acta Metall.*, Vol. 28, pp 1661–1708

Lefebvre, A. H 1989 *Atomization and Sprays*, Hemisphere, New York

Liang, P Y 1991 Numerical method for calculation of surface tension flows on arbitrary grids, *AIAA J* , Vol 29 No 2, pp 161–167

Liang, S 1986 Random-Walk simulation of flows in Hele-Shaw cells, *Physical Review A*, Vol 33, No 4, pp 2663–2674

McCay, M H McCay, T D and Hopkins, J A. 1993 Optical analyses of fluid flow effects on directional solidification rates in NH_4Cl-H_2O solution, *HTD*, Vol 234, ASME 1993, pp 1–11

McFadden, G B and Coriell, S R. 1987 Non-planar interface morphologies during unidirectional solidification, *J. Crystal Growth*, Vol 84, pp 371–388

McFadden, G B , Coriell S R , Boisvert, R. F. Glicksman, M E. and Fang, Q. T. 1984 Morphological stability in the presence of fluid flow in the melt, *Metall. Trans A*, Vol 15A, pp 2117–2124

McLean, J W and Saffman, P G 1981 The effect of surface tension on the shape of fingers in a Hele-Shaw cell, *J Fluid Mech* , Vol 102, pp 455–469

Miyata, H. 1986 Finite difference simulation of breaking waves, *J Comp Phys* , Vol 65, pp 179–214

Morinishi, K. 1992 A finite difference solution of the Euler equations on body-fitted Cartesian grids, *Comput Fluids*, Vol 21, No 3, pp 331–344

Mullins, W W and Sekerka, R.F 1964 Stability of a planar interface during solidification of a dilute binary alloy, *J Appl. Phys.*, Vol. 3, pp 444–451

Muschol M , Liu, D and Cummins, H. Z. 1992 Surface tension anisotropy measurements of Succinonitrile and Pivalic Acid comparison with microscopic solvability theory, *Phys Rev A*, Vol 46, No 5, pp 1038–1050

Nakaya, U 1954 *Snow Crystals*, Harvard University Press, Cambridge, MA.

Ni, J and Beckermann, C 1993 Modeling of globulitic alloy solidification with convection, *J Mater Proc and Man Sci* , Vol 2, pp 217–231

Oran, E. S., and Boris, J P 1987 *Numerical Simulation of Reactive Flow*, Elsevier, New York

Osher, S. and Sethian, J A. 1988 Fronts propagating with curvature dependent speed : Algorithms based on Hamilton-Jacobi formulations *J Comp Phys* , Vol 79, pp 12–49

Ostrach, S 1983 Fluid mechanics in crystal growth, *J Fluids Engg* , Vol 105, pp 5–20

Patankar, S V 1980 *Numerical Heat Transfer and Fluid Flow*, Hemisphere Publishing Corp , Washington D C

Pelce, P 1988 *Dynamics of Curved Fronts*, in Perspectives in Physics Series, Academic Press Inc , New York

Penrose, O and Fife, P C 1990 Thermodynamically consistent models of phase-field type for the kinetics of phase transitions, *Physica D*, Vol 43, pp 44–62

Pieters, R. and Langer, J S 1986 Noise-driven Sidebranching in Dendritic Crystal Growth, *Phys Rev Lett.*, Vol 56, pp 1948–1952

Poo, J Y and Ashgriz, N 1991 FLAIR, Flux Line-segment Model for Advection and Interface Reconstruction, *J Comput Phys* , Vol 93, pp 449–468

Quirk, J J 1992 An alternative to unstructured grids for computing gas dynamic flows around arbitrarily complex two-dimensional bodies, *ICASE Report No 92–7*, NASA Langley Research Center, Hampton, VA.

Rappaz, M 1989 Modelling of microstructure formation in solidification processes, *Inter Mat Rev* , Vol 34, No 3, pp 93–123

Rappaz, M and Thevoz, Ph 1987 Solute diffusion model for equiaxed dendritic growth Analytical solution, *Acta Metall* , Vol 35, No 12, pp 2929–2933

Rayleigh, Lord 1899 *Scientific Papers*, Vol 1, Cambridge, England

Rubinstein, E R. and Glicksman, M E. 1990 Dendritic growth kinetics and structure, I Pivalic Acid, II Camphene, *J Crystal Growth* Vol 112, pp 84–110

Saffman, P G and Taylor G I 1958 The penetration of a fluid into a porous medium or Hele-Shew cell containing a more viscous fluid, *Proc. Royal Soc Lond.*, A 245, pp 312– 329

Sato, T., Kurz, W and Ikawa, K. 1987 Experiments on dendrite branch detachment in the Succinonitrile-Camphor alloy, *Trans. Japan Inst Met.*, Vol 28, No 12, pp 1012–1021

Saito, Y, Goldbeck Wood, G and Muller Krumbhaar, H. 1988 Numerical simulation of dendritic growth, *Phys Rev A*, Vol 38, No 4, pp 2148–2157

Sekerka, R F 1993 Role of instabilities in determination of the shapes of growing crystals, *J Crystal Growth*, Vol 128, pp 1–12

Sethian, J A. 1990 Numerical algorithms for propagating interfaces Hamilton–Jacobi equations and conservation laws, *J Diff Geom* , Vol. 31, pp 131–161

Sethian, J A. and Strain, J 1992 Crystal growth and dendritic solidification, *J Comp Phys* , Vol 98, No 2, pp 231–253

Sharp, D.H 1984 An overview of Rayleigh Taylor instability, *Physica 12D*, pp 3–18.

Shyy, W 1987 An adaptive grid method for Navier Stokes flow computation, *Appl. Math. Comput.*, Vol. 21, pp 201–219.

Shyy, W 1994 *Computational Modelling for Fluid Flow and Interfacial Transport*, Elsevier, Amsterdam, The Netherlands.

Shyy, W., Pang, Y., Hunter, G. B., Wei, D. Y. and Chen, M.-H. 1992 Modelling of turbulent transport during continuous ingot casting, *Int. J. Heat Mass Transfer*, Vol. 35, pp. 1229–1245.

Shyy, W. and Rao, M.M. 1993 Enthalpy based formulations for phase change problems with application to gritter, *AIAA Paper No. 93–2831, also Microgravity Sci. and Tech.* Vol. 7 (1994), pp. 41–491.

Smith, J.B. 1981 Shape instabilities in pattern formation in solidification: A new method for numerical solution of the moving boundary problem, *J. Comp. Phys.*, Vol. 39, pp. 112–127.

Straus, J. 1989 A boundary integral approach to unstable solidification, *J. Comp. Phys.*, Vol. 85, pp. 342–389.

Tabeling, P., Zocchi, G. and Libchaber, A. 1987 An experimental study of the Saffman-Taylor instability, *J. Fluid Mech.*, Vol. 177, pp. 67–82.

Thevoz, Ph., Desbolles, J. L. and Rappaz, M. 1989 Modelling of equiaxed micro structure in casting, *Metall. Trans. A*, Vol. 20A, pp. 311–322.

Thompson, J.F., Warsi, Z. U. A., and Mastin, C.W. 1985 *Numerical Grid Generation*, Elsevier, New York.

Thomson, M.E. and Szekely, J. 1989 Density stratification due to counterbuoyant flow along a vertical crystallisation front, *Int. J. Heat and Mass Transfer*, Vol. 32, pp. 1021–1036.

Tirmizi, S.H. and Gill, W.N. 1987 Effect of natural convection on growth velocity and morphology of dendritic ice crystals, *J. Crystal Growth*, Vol. 85, pp. 488–502.

Trivedi, R. and Somboonsuk, K. 1984 Constrained dendritic growth and spacing, *Mater. Sci. Engg.*, Vol. 65, pp. 65–74.

Trygvasson, G. and Unverdi, S.O. 1992 A front tracking method for viscous, incompressible, multi-dimensional flows, *J. Comp. Phys.*, Vol. 100, pp. 25–37.

Tseng, A. A., Zou, J., Wang, H. P. and Hoole, S. R. H. 1989 Numerical modeling of macro and micro behaviors of materials in processing: A review, *J. Comput. Phys.*, Vol. 102, pp. 1–17.

Turner, J.S. 1973 *Buoyancy Effects in Fluids*, Cambridge University Press, London.

Ungar, L H and Brown, R A 1984 Cellular interface morphologies in directional solidification The one-sided model, *Phys Rev B*, Vol 29, No 3, pp 1367–1380

Unverdi, S O and Tryggvason, G 1992 A front-tracking method for viscous, incompressible multi-fluid flows, *J Comp Phys*, Vol 100, pp 25–37

Vanden–Broeck, J -M 1983 Fingers in a Hele-Shaw cell with surface tension, *Phys Fluids*, Vol 26, pp 2033–2034

Viecelli, J A 1971 A computing method for incompressible flows bounded by moving walls, *J Comp Phys*, Vol 8, pp 119–143

Voller, V R and Cross, M 1981 Accurate Solutions of moving boundary problems using the enthalpy method, *Int J Heat Mass Transf*, Vol 24, pp 545–556

Voller, V R and Prakash, C 1987 A fixed grid numerical modelling methodology for convection-diffusion mushy region phase change problem, *Int J Heat and Mass Transfer*, Vol 30, pp 1709–1719

Wang, C Y and Beckermann, C 1993 Single vs dual-scale volume averaging for heterogeneous multiphase systems, *Int J Multiphase Flow*, Vol 19, No 2, pp 397–407

Wang, J C T and Widhopf, G F 1989 A high-resolution TVD finite volume scheme for the Euler equations in conservation form, *J Comp Phys*, Vol 84, pp 145–173

Weeks, J D and Gilmer, G H 1979 Dynamics of crystal growth, *Adv Chem. Phys*, Vol 40, pp 157–224

Wheeler, A A., Murray, B T and Schaefer, R J 1993 Computations of dendrites using a phase field model, *Physica D*, Vol 66, pp 243–262

Woodruff, D P 1973 *The Solid Liquid Interface*, Cambridge Press, Cambridge

Wright, J A. and Shyy, W 1992 A pressure-based composite grid method for the incompressible N-S equations, *J Comp Phys.*, Vol 107, pp 225–238

Xiao, R.-F, Alexander, J I., and Rosenberger, F 1988 Morphological evolution of growing crystals A Monte–Carlo simulation, *Phys Rev A*, Vol 38, No 5

Xiao, R.-F, Alexander, J I , and Rosenberger, F 1990 Growth morphology with anisotropic surface kinetics, *J Crystal Growth*, Vol 100, pp 313–329

Xu, J -J 1988 Asymptotic behavior of steady dendritic growth at far-field, *Phys Rev A*, Vol 37, No 8, pp 3087, 3095

Yao, L S , and Prusa, J 1989 Melting and freezing *Adv in Heat Transf*, Eds J P Hartnett and T F Irvine, Vol 19, pp 1–95

Youngs, D L. 1984 Time dependent multimaterial flow with large fluid distortion, in *Numerical Methods for Fluid Dynamics*, Eds K W Morton and M J Baines, Academic, New York, pp 273–285

Zeeuw, D D and Powell, K.G 1993 An adaptively refined Cartesian mesh solver for the Euler equations, *AIAA Paper No 90–0001*

BIOGRAPHICAL SKETCH

H S. Udaykumar was born April 8, 1967, in the city of Madras, India. He did most of his schooling in the placid, picturesque town of Mysore, India. He obtained a bachelors degree in aerospace engineering from the Indian Institute of Technology, Madras in 1988. He began his master's degree studies at the University of Florida in the same year and obtained the degree in 1990. Since then he has been in pursuit of a seemingly elusive doctorate in aerospace engineering at the same institution.

I certify that I have read this study and that in my opinion it conforms to acceptable standards of scholarly presentation and is fully adequate, in scope and quality, as a dissertation for the degree of Doctor of Philosophy

Wei Shyy, Chairperson
Professor of Aerospace Engineering
Mechanics and Engineering Science

I certify that I have read this study and that in my opinion it conforms to acceptable standards of scholarly presentation and is fully adequate, in scope and quality, as a dissertation for the degree of Doctor of Philosophy

Ulrich H. Kurzweg
Professor of Aerospace Engineering,
Mechanics and Engineering Science

I certify that I have read this study and that in my opinion it conforms to acceptable standards of scholarly presentation and is fully adequate, in scope and quality, as a dissertation for the degree of Doctor of Philosophy

Lawrence E. Malvern
Professor of Aerospace Engineering,
Mechanics and Engineering Science

I certify that I have read this study and that in my opinion it conforms to acceptable standards of scholarly presentation and is fully adequate, in scope and quality, as a dissertation for the degree of Doctor of Philosophy

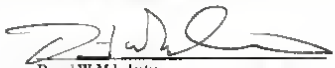

David W Mikolaitis
Associate Professor of Aerospace Engineering, Mechanics and Engineering Science

I certify that I have read this study and that in my opinion it conforms to acceptable standards of scholarly presentation and is fully adequate, in scope and quality, as a dissertation for the degree of Doctor of Philosophy

R Narayanan
Professor of Chemical Engineering

This dissertation was submitted to the Graduate Faculty of the College of Engineering and to the Graduate School and was accepted as partial fulfillment of the requirements for the degree of Doctor of Philosophy

December 1994

Winfred M Phillips
Dean, College of Engineering

Karen A Holbrook
Dean, Graduate School